Fundamental Understanding and Design Principles of Oxide/Metal Surfaces for Lithium Storage

by

Yi-Chun Lu

Bachelor of Science, Materials Science and Engineering

National Tsing Hua University, Taiwan, 2007

Submitted to the Department of Materials Science and Engineering in partial fulfillment of the requirements for the degree of

DOCTOR OF PHILOSOPHY IN MATERIALS SCIENCE AND ENGINEERING

AT THE MASSACHUSETTS INSTITUTE OF TECHNOLOGY

JUNE 2012

Signature of Author:_____

Department of Materials Science and Engineering
May 18, 2012

Certified by:_____

Yang Shao-Horn
Gail E. Kendall Chair of Mechanical Engineering
Associate Professor of Materials Science and Engineering
Thesis Supervisor

Accepted by:_____

Gerbrand Ceder
Professor of Materials Science and Engineering
Chair, Departmental Committee on Graduate Student

Fundamental Understanding and Design Principles of Oxide/Metal Surfaces for Lithium Storage

by

Yi-Chun Lu

Submitted to the Department of Materials Science and Engineering
on May 18, 2012
in Partial Fulfillment of the Requirements for the Degree of
Doctor of Philosophy in Materials Science and Engineering

Abstract

Lithium-battery technologies have promising potentials to enable efficient energy distribution, sustainable transportation systems, and the widespread of renewable energy. One of the most critical challenges that limits their further advances is the limited ability to design efficient interfacial and surface chemistries due to the lack of fundamental understanding of reaction mechanisms. This thesis aimed to develop the fundamental understanding and design principles of oxide and metal surfaces for conventional Li-ion batteries and next generation, high-energy Li-air (or Li-O_2) batteries. Fundamental approaches involving electrochemical characterizations, advanced spectroscopic and microscopic techniques were used to probe the interfacial and surface reactions of these batteries.

The criteria for efficient electrode-electrolyte interfaces for Li-ion batteries were identified by examining the working mechanism of "$AlPO_4$" nanoparticle coatings on enhancing the cycle life and energy efficiency of $LiCoO_2$ batteries. SEM, XRD and XPS revealed that the "$AlPO_4$" nanoparticles promote the formation of Co-Al-O-F species on the $LiCoO_2$ particle surfaces as protection layers against electrolyte decomposition and oxygen loss from the lattice. This highlights the importance of metal oxyfluoride species toward material stability and cell efficiency.

The reaction kinetics, catalyst effects and reaction mechanism of Li-O_2 batteries were investigated by developing electrochemical model systems i.e., rotating disk electrode and Li_2O_2-filled composite electrodes, to quantify the intrinsic catalytic activity of nonaqueous oxygen reduction (ORR) and oxygen evolution reactions (OER). We found that the Li^+-ORR activity is in order of Pd > Pt > Ru ≈ Au > C, exhibiting a volcano-type dependence as a function of the oxygen adsorption energy of the catalyst surface. This volcano dependence suggests that the oxygen adsorption energy of the catalyst can serve as the ORR activity descriptor for designing highly active ORR catalyst for Li-O_2 batteries. In addition, the application of Au nanoparticles was found to significantly increase the rate

capability of the Li-O_2 cells by enhancing the intrinsic ORR activity and influencing the structures of the discharge products. The catalyst effects on the charge reaction (OER), or Li_2O_2-decomposition reaction, were studied by potentiostatically oxidizing the Li_2O_2-filled composite electrodes with various catalysts. It is found that the electro-oxidation of Li_2O_2 can be significantly catalysed by the presence of Pt/C. With insights obtained from the model system studies, we designed bimetallic PtAu nanoparticles as bifunctional catalysts for Li-O_2 batteries. Interestingly, the PtAu/C catalyst exhibits similar discharge profile to the Au/C and mirrors the charge activity of the Pt/C catalyst, achieving a remarkable round-trip efficiency (~75%) for rechargeable Li-O_2 batteries.

Thesis Supervisor: Yang Shao-Horn
Gail E. Kendall Chair of Mechanical Engineering,
Associate Professor of Materials Science and Engineering

Dedicated to My Beloved Parents
&
My Mentor in Life: Daisaku Ikeda, SGI President

Acknowledgements

I want to express my deepest appreciation to those who have made this work possible and my journey at MIT memorable.

First and foremost, I would like to thank my advisor, Professor Yang Shao-Horn, for her tireless efforts in nurturing me into an independent researcher and ceaseless support for my professional and personal developments. It was through her limitless passion and rigorous training that this thesis and my Ph.D. career at MIT have been made possible.

I would like to thank Professor Hubert Gasteiger, who has guided me to enable the Li-air research in this thesis and taught me the true essence of having fun in lab! It was truly a lifelong benefit for this encounter. I am also grateful for the insightful advice and fruitful discussions from my thesis committee members, Professor Daniel Nocera and Professor Jeffery Grossman. I also acknowledge Prof. Yew at National Tsing Hua University for her continuous support and valuable guidance.

Many of my colleagues and collaborators have helped me greatly to complete this work. I especially thank Dr. Azzam Mansour for his mentorship in X-ray photoelectron spectroscopy, and Dr. Naoaki Yabuuchi for sharing his knowledge in battery chemistry. I thank ALL my EEL members for their heartfelt support, especially Ethan, Shuo, Jonathon, Pierre, David, Eva, Wenchao, Hye Ryung, Lei, Jin, Betar, Chris C., Chris K., Seung Woo, GJ, Yuki, Ted, and Jungik.

Another important part of my Ph.D. life has been enlightened by my friends and fellow members in SGI. To begin, I want to thank my mentor in life, SGI President, Daisaku Ikeda, who has made me awaken to my dream and mission. Next, I would like to thank genuine support from my friends. Special thanks to Amy, Shih-Long, Vivian, Hsu-Yi, Chao Ling, Chung-Yi, Elise, Teri, Mint, Jessie, Tanya, Beth, Shu-Hua, Victor, Woei Ling, Liang-Yi, Chun-Hsiang, Carl, and Tsao-Hsien.

Finally, I want to give my deepest thanks to my family, especially my parents, uncle, aunt and my two sisters for their wholehearted support and love. Thank you for loving who I am and always be there for me.

Table of Contents

List of Figures

List of Tables

Chapter 1. Introduction

1.1 Motivation

The development of reliable and efficient energy storage systems is vital to effectively utilize intermittent renewable energy sources and create a sustainable transportation system.[1,2] Bridging the gap between the renewable energy and user demands, energy storage can increase the deployment of renewable energy sources, enhance the reliability/efficiency of the grid, and enable electric vehicles to decrease dependence of limited fossil fuels (Figure 1-1).[1-6]

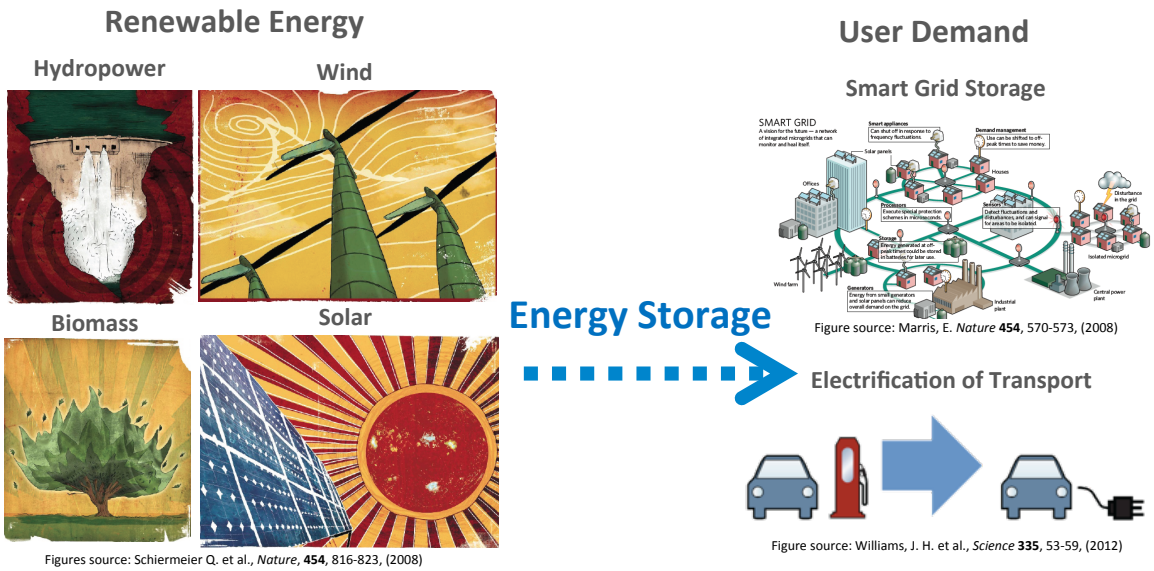

Figure 1-1. The role of energy storage is to bridge the gap between the intermittent renewable energy sources and user demands, including electric grid storage and electrification of transport. Figure sources: Schiermeier, Q. et al., *Nature* **454**, 816-823, (2008), Marris, E. *Nature* **454**, 570-573, (2008), and Williams, J. H. et al., *Science* **335**, 53-59, (2012).

The power rating and discharge duration time of the energy storage system determine the potential applications of such system. Figure 1-2 shows the comparison of discharge time and power rating for various energy storage technologies. It is clear that battery technology is the most commonly used system across wide range of applications due to its high energy density, satisfactory power capability and high mobility.[7,8]

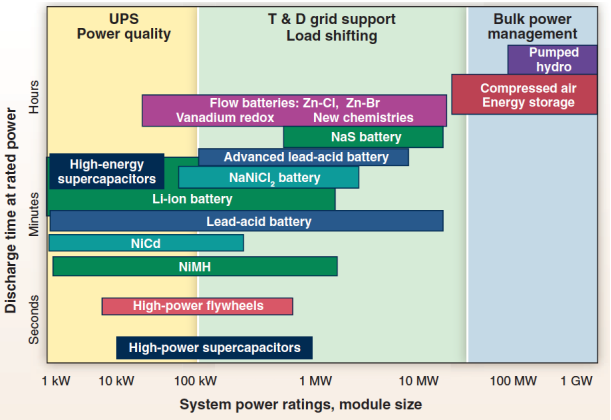

Figure 1-2. Comparison of discharge time and power rating for various energy storage technologies. Adapted from Dunn, B. et al., *Science* **334**, 928-935, (2011). [Courtesy of Electric Power Research Institute]

Among various battery technologies, lithium-ion (Li-ion) batteries have received the most attentions, owing to their high energy density, high efficiency and design flexibility.[9] Figure 1-3 shows that the Li-ion batteries offer the highest specific power and specific energy compared to all the common rechargeable batteries.

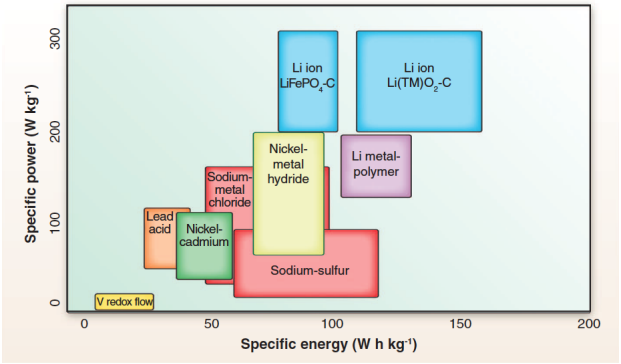

Figure 1-3. Gravimetric power and energy densities for various rechargeable batteries. Adapted from Dunn, B. et al., *Science* **334**, 928-935, (2011).

Li-ion batteries can serve as stationary power stations for grid storage as well as mobile energy sources for electrification of transport (Figure 1-1). For grid storage, Li-ion batteries can store excess energy from renewable sources and release it at times of greater demand.[2] For instance, the electric power profile shown in Figure 1-4 illustrates

that the use of Li-ion batteries (or other energy storage systems) helps accommodating peak loads to improve the performance of the electric grid.[2] At off-peak times, the excess energy is stored when the generation from baseload and renewable is greater than the load. At peak times, the extra load needed is supplied from the energy storage when the total load is greater than the total generation from baseload and renewable energy sources.[2] Enabling load shifting with renewable energy sources improves the reliability, stability and cost of the grid.[2]

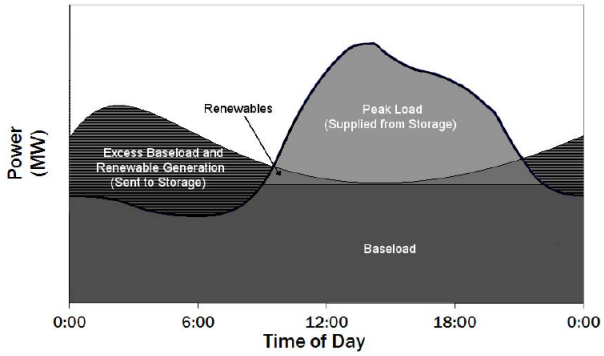

Figure 1-4. The effect of energy storage on the grid load profile. Adapted from Dunn et al., *Science* **334**, 928-935, (2011).

For electrification of transport, the Li-ion battery is an essential component to replace internal combustion engine cars with plug-in hybrid electric vehicles (PHEVs), or hybrid electric vehicles (HEVs), and ultimately all-electric vehicles (EVs). For example, General Motors introduced the Chevrolet Volt® EV with 40 miles driving range and Nissan introduced the Leaf® EV with 100 miles driving range in 2010. These commercialized EVs are powered by Li-ion battery packs. Electric cars are expected to have zero or controlled emission and provide a distributed storage mechanism for the grid, which can use energy from renewable resources, as illustrated in Figure 1-5.[5]

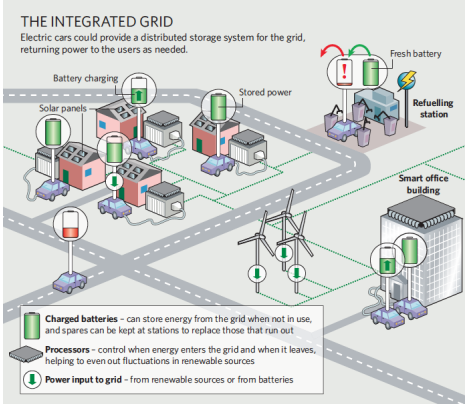

Figure 1-5. Example of using energy storage devices in the EVs as means to distribute energy for the grid and return power to the users as needed. Adapted from Tollefson, J. *Nature* **456**, 436-440, (2008).

The critical roles of energy storage technologies, especially Li-ion batteries, on maximizing our ability to exploit renewable energy sources, enabling efficient energy distribution, and creating zero-emission sustainable transportation system provide a large motivation for our studies.

1.2 Lithium-Ion Batteries

1.2.1 Working Principle of Li-Ion Batteries

Li-ion batteries are consisted of two host electrodes (positive electrode and negative electrode) and an electrolyte that transports Li ions between two electrodes, as shown in Figure 1-6.[10] The positive electrode material is typically a metal oxide with a layered structure, such as lithium cobalt oxide ($LiCoO_2$) and the negative electrode material is typically a graphitic carbon in a commercial cell.[10] During charge, electrical energy is used to remove lithium ions from the positive electrode to the negative electrode. During discharge, lithium ions release energy by migrating from the negative electrode to the positive electrode. The electrochemical reactions of the positive electrode and negative electrode during cell operation are illustrated in Eq. 1-1 to Eq. 1-2 (e.g. a Carbon-$LiCoO_2$

cell). The overall reaction is obtained by combining Eq. 1-1 and Eq. 1-2, as shown in Eq. 1-3.

$$\text{Positive electrode: } LiCoO_2 \Leftrightarrow Li_{1-x}CoO_2 + xLi^+ + xe^- \quad (1\text{-}1)$$

$$\text{Negative electrode: } C + xLi^+ + xe^- \Leftrightarrow Li_xC \quad (1\text{-}2)$$

$$\text{Overall: } LiCoO_2 + C \Leftrightarrow Li_{1-x}CoO_2 + Li_xC \quad (1\text{-}3)$$

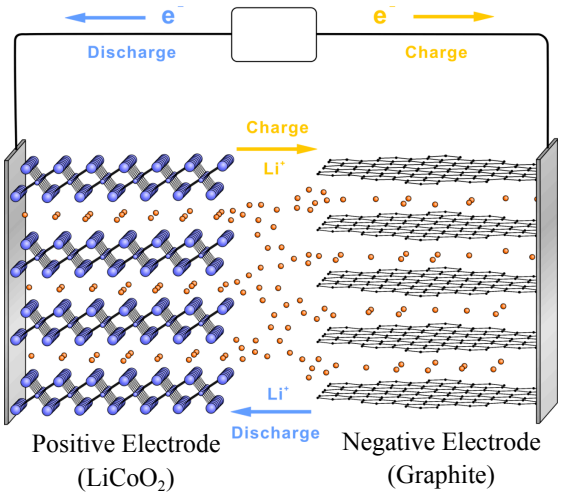

Figure 1-6. Schematic illustration of electrochemical process of Li-on batteries. Adapted from Prof. Yang Shao-Horn's course (2.625) materials.

1.2.2 Challenges of Li-Ion Batteries

Ideally, the Li ions are reversibly inserted or extracted from the electrodes without significant changes to the host materials. However, significant capacity fading and decrease of energy efficiency were observed during cycling to high voltages.[11,12] Structural instability and surface reactivity toward the electrolyte have been proposed as mechanisms for the degradation.[13] Surface modification via coatings with the host materials is one of the most successful methods of improving the battery performance.[14-16] For instance, "$AlPO_4$"-coated $LiCoO_2$ reported by Cho et al.[17,18] has shown superior cycling performance relative to $LiCoO_2$ coated with other oxides. However, the origin of the enhancement associated with the surface modification is not well understood, which limits the rational optimization process for lithium

transition metal oxide electrodes.

Another critical barrier of the Li-ion batteries for EVs applications is the insufficient specific energy, owing to the inherent charge storage limitation of the positive electrodes (i.e., typically one electron transfer per transition metal). The voltage and capacity comparison of existing intercalation compounds is shown in Figure 1-7, which indicates that the overall capacities of current Li-ion batteries are limited by the positive electrodes. To date, the specific energy of state-of-the-art rechargeable Li-ion battery packs can only provide 100 to 120 Wh/kg for all-electric vehicle applications,[19,20] and further engineering optimization using currently known materials may yield up to ≈50% higher values (≈180 Wh/kg). Unfortunately, this is still insufficient to support the long-term vision of sustainable transportation on the basis of full-range (300 miles) EVs, since the required ≈75 kWh battery would weigh at least ≈400 kg and thus compromise vehicle efficiency. Together, the Li-ion technology is facing two critical challenges. First, the lack of fundamental understanding of the role of surface modification and interfacial chemistry hinders the rational design of the Li-ion electrode materials. Second, the inherently limited specific energy prevents the use of Li-ion technology for sustainable EVs applications.

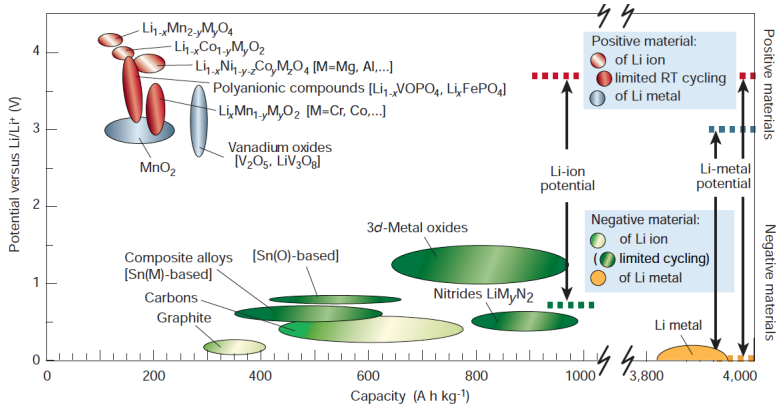

Figure 1-7. Voltage versus capacity for positive- and negative- electrode materials used in current Li-ion batteries. Adapted from Tarascon, J.-M. & Armand, M. *Nature* **414**, 359-367, (2001)

1.3 Rechargeable Lithium-Air Batteries

New battery chemistries that provide much higher specific energy are required to fulfill satisfactory driving range with reasonable battery pack weight. One promising approach leading to 3-4 times higher the specific energy of the positive electrode involves replacing the intercalation compound with a catalytically active oxygen electrode, forming a so-called lithium-air (Li-air) battery.[21] Figure 1-8 shows the practical specific energy of the rechargeable Li-air batteries together with other comment battery systems.[22] It is clear that the Li-air system has the best potential providing lightweight and long driving-range batteries for EVs applications.

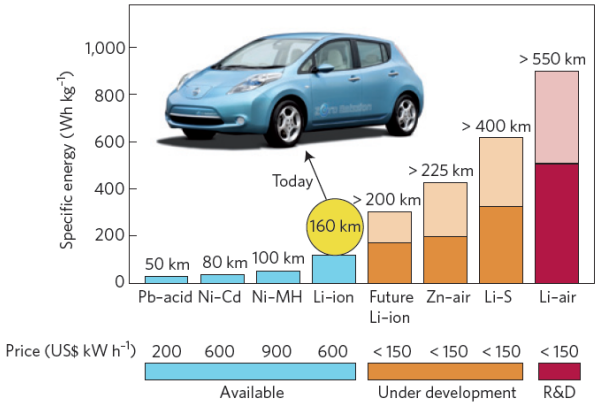

Figure 1-8. Practical specific energies of various rechargeable batteries, along with estimated driving distances and pack prices. Adapted from Bruce, P. et al., *Nat. Mater.* **11**, 19-29, (2012).

1.3.1 Working Principle of Rechargeable Li-Air Batteries

The working principle of rechargeable Li-air (or Li-O_2) batteries is shown in Figure 1-9. During discharge, oxygen from the air gets reduced and reacts with lithium ions to form lithium (per)oxide (oxygen reduction reaction, ORR). During charge, these oxides are oxidized and decomposed to regenerate lithium ions and O_2 (oxygen evolution reaction, OER). The electrochemical reactions of the positive electrode (O_2) and negative electrode (Li) during cell operation are illustrated in Eq. 1-4 to Eq. 1-5. The overall reaction is obtained by combining Eq. 1-4 and Eq. 1-5, as shown in Eq. 1-6.[21]

$$\text{Positive electrode: } O_2 + xLi^+ + xe^- \Leftrightarrow Li_xO_2 \text{ (x=2 or 4)} \quad (1\text{-}4)$$

$$\text{Negative electrode: } xLi \Leftrightarrow xLi^+ + xe^- \quad (1\text{-}5)$$

$$\text{Overall: } O_2 + xLi \Leftrightarrow Li_xO_2 \text{ (x=2 or 4)} \quad (1\text{-}6)$$

While the thermodynamic standard potential for Li_2O_2 formation is commonly quoted as ≈3.1 V vs. Li (V_{Li}),[21,23,24] no references to the thermodynamic database underlying its derivation were provided, and it should be noted that the value based on the NIST-JANAF thermochemical tables is actually 2.96 V_{Li},[25,26] which may be compared to a very similar value of 2.91 V_{Li} for Li_2O formation.[25] The latter values result in the expected positive entropy change for the thermal decomposition of lithium peroxide into gaseous oxygen and lithium oxide ($Li_2O_2 \rightarrow Li_2O + 0.5\,O_2$), while the previously reported value of ≈3.1 V_{Li} for Li_2O_2 would predict an obviously incorrect negative entropy change.

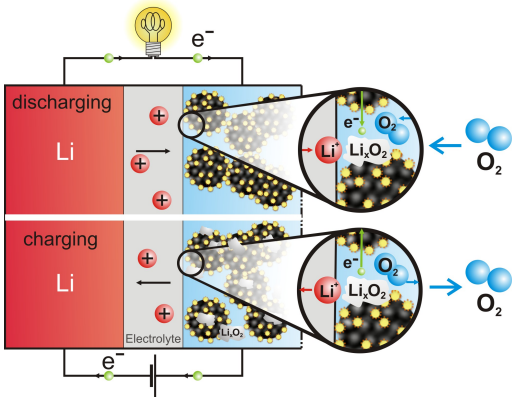

Figure 1-9. Working principle of a rechargeable Li-O_2 battery. Adapted from Lu, Y.C. et al., *Energy Environ. Sci.* **4**, 2999-3007, (2011).

Unlike the Li-ion batteries, where the specific capacities are limited by the lithium sites available in the host structure, the specific capacity of the Li-O_2 batteries are dominated by electrode porosity required to provide Li_xO_2 storage[23] and by oxygen diffusion through the electrolyte-flooded pores (this depends on the solubility of oxygen in the electrolyte).[27] Thus using high oxygen pressures and electrolytes with high oxygen solubility will increase specific capacities,[28] which is consistent with current distribution modeling.[29] Conventionally, specific capacities for carbon-based Li-O_2 electrodes are normalized to carbon weight, with values reported as high as 2500-5000 mAh/g_{carbon}.[30-32] For O_2-electrodes

based on high-surface-area carbon blacks with carbon volume fraction of ≈15%,[33] the maximum specific capacities can be estimated by assuming a required electrolyte volume fraction of 25% (note that capacities calculated this way were experimentally verified for the ice-filling of fuel cell cathodes[34] discharged at -20°C and 10 mA/cm^2). While these estimated maximum capacities shown in Table 1-1 agree well with capacities reported at low discharge rates (e.g., 5000 mAh/g_{carbon} at 0.01 mA/$cm^2_{electrode}$[30]), lower capacities are obtained at higher discharge rates[28,29,35] having a lower degree of electrode pore filling with Li_xO_2.[29] To compare O_2-electrodes capacities for Li-O_2 with those of Li-ion batteries, capacities must be normalized to the lithiated (discharged) electrode mass, including carbon in O_2-electrodes due to its high mass fraction. Table 1-1 shows that >5-fold higher specific capacities and >4-fold higher specific energies are projected for O_2-electrodes compared to state-of-the-art $LiCoO_2$, whereby a considerably higher capacity could be obtained by catalysts selective for Li_2O formation during discharge and active for electro-oxidizing Li_2O upon charging.

Table 1-1. Maximum specific capacity and energy for Li-air cathodes compared to $LiCoO_2$ intercalation cathodes in current Li-ion batteries. Underlying assumptions for carbon black (e.g., Vulcan-XC72) based Li-O_2 electrodes: *i)* carbon packing density of 0.36 g/cm^3 with ≈15% carbon volume fraction[33]; *ii)* 25% electrolyte volume fraction; *iii)* complete filling of the 60% void volume fraction with Li_xO_2 product. Modified from Lu, Y.C. et al., *Electrochem. Solid State Lett.* **13**, A69-A72, (2010).

	Li_2O_2	Li_2O	$LiCoO_2$
specific capacity wrt. carbon [mAh/g_{carbon}]	4600	6000	n.a.
specific capacity wrt. C+Li_xO_2 or $LiCoO_2$ [mAh/$g_{electrode}$]	900	1350	160
average discharge voltage [V_{Li}]	2.75	2.75	3.9
specific energy wrt. C+Li_xO_2 or $LiCoO_2$ [Wh/$kg_{electrode}$]	2450	3700	620

1.3.2 Challenges of Rechargeable Li-Air Batteries

Major challenges in developing Li-air (Li-O_2) batteries for practical applications include poor cycle life (10 – 100 cycles),[31,32,36] low rate capability (typically 0.1 to 1 mA/cm^2),[27,35,37,38] , and low round-trip efficiency (53 – 64 %,[39] 70 %,[31]). In Particular, the

latter are expected to strongly depend on the catalytic activity of the electrodes, but little is known about the electrocatalytic reduction and evolution of oxygen in the presence of lithium ions in nonaqueous electrolytes, thus hindering the progress of rechargeable Li-O_2 battery technology.

1.4 Thesis Overview

To overcome the critical challenges facing the rechargeable Li-ion and Li-O_2 batteries discussed above, the major objective of this thesis is to develop fundamental understanding and design principles of efficient metal/oxide surfaces for Li-ion and Li-O_2 batteries. First, we will investigate the role of surface chemistry of oxide-electrolyte interfaces on the efficiency and cycle life of the Li-ion batteries. The working principles of surface modification and criteria for the effective oxide-electrolyte interfaces will be discussed. (**Chapter 2**)

Second, the reaction kinetics, catalyst effects and reaction mechanism of Li-O_2 batteries will be investigated. In **Chapter 3**, a systematic methodology, namely rotating disk electrode (RDE), for quantifying the intrinsic catalytic activities and reaction kinetics of ORR during discharge in Li^+-containing nonaqueous media will be developed in the absence of undefined oxygen transport loss. Systems studied include well-defined glassy carbon (GC) electrodes as well as high-surface-area Vulcan carbon (VC) dispersed as a thin-film layer (~1 to ~5 μm) on the GC electrode in a RDE configuration.

In **Chapter 4**, the catalyst effects and reaction mechanism of the discharge reaction of Li-O_2 batteries will be discussed. The catalytic activity trends of Li^+-ORR of four different polycrystalline metal catalysts including palladium (Pd), platinum (Pt), ruthenium (Ru), gold (Au) as well as GC will be examined via the RDE technique developed in **Chapter 3**. We will examine materials' properties that control the activity of the Li^+-ORR and develop predictive tools for the design and screening of highly active catalysts. In addition, the activity trend obtained on these polycrystalline surfaces will be compared to that of high-surface-area thin film catalysts supported on GC electrode via the

RDE, and the discharge voltages of the Li-O_2 cells. Furthermore, the catalyst effects on the discharge rate capability of the Li-O_2 cells will be investigated coupled with spectroscopic techniques to reveal the reaction mechanism. Lastly, the nonaqueous Li^+-ORR mechanisms and rate-determining steps will be discussed and compared to that in aqueous media.

In **Chapter 5**, model electrodes that control the quantity and the morphology of the reactant of the charge reaction, e.g., Li_2O_2, will be developed to enable quantitative determination of Li_2O_2-decomposition reaction (oxygen evolution reaction, OER) kinetics and direct comparison of OER activity across different catalyst materials. In addition, the results obtained from the electro-oxidation of Li_2O_2 will be compared to the charging behavior in the Li-O_2 cells. Furthermore, insights obtained from the ORR and OER model systems will be applied to design a bifunctional catalyst to increase the round-trip efficiency of rechargeable Li-O_2 batteries. Finally, conclusion and perspective of fundamental approaches and strategies toward better understanding of oxide/metal surfaces for Li-storage and efficiency material systems will be discussed in **Chapter 6**.

Chapter 2. Probing the Origin of Enhanced Stability of "$AlPO_4$" Nanoparticle Coated $LiCoO_2$ During Cycling to High Voltages

Reproduced in part with permission from Yi-Chun Lu, Azzam N. Mansour, Naoaki Yabuuchi, and Yang Shao-Horn, Probing the Origin of Enhanced Stability of "$AlPO_4$" Nanoparticle Coated $LiCoO_2$ during Cycling to High Voltages: Combined XRD and XPS Studies. **Chem. Mater. 2009**, 21, 4408-4424, Copyright 2009 American Chemical Society.

2.1 Introduction

Application of an oxide, phosphate and fluoride such as ZrO_2,[14] Al_2O_3,[14,15] TiO_2,[14,40] $AlPO_4$[17,18,41-46]and AlF_3[16] to the surfaces of lithium transition metal oxide particles such as $LiCoO_2$ has shown to improve capacity retention upon cycling to high voltages. However, the origin in the performance improvement of surface-modified positive electrodes during electrochemical cycling is not well understood. Cho et al.[47,48] and Fey et al.[49,50] have first proposed that the oxide coating (e.g. Al_2O_3 and ZrO_2) can suppress phase transitions by constraining active particles against lattice parameter changes associated with lithium removal and insertion, which would reduce stresses and structural damage within individual particles, and improve capacity retention during cycling. However, it is shown subsequently[41-46,51] that suppression of lattice expansion is not necessary to obtain improved cycling performance of "$AlPO_4$"- and oxide-coated $LiCoO_2$. Another school of thought is that coating materials[52] and/or processes involved in application of coating[51] modify the surfaces of active materials and surface reactions between active materials and the electrolyte, and stabilize active materials upon cycling to high voltages. On one hand, several studies[53,54] have shown that the coating particles not only serve as a physical barrier to reduce the corrosion of the active material by HF in the electrolyte (a common contaminant in $LiPF_6$-containging electrolyte[55]) and to decrease electrode impedance but also scavenge HF in the electrolyte by the formation of metal fluorides. This mechanism (referred to as the HF-scavenge-model here) could explain many common observed effects of metal oxide coatings such as: 1) suppression of the dissolution of transition metals in the lithium transition metal oxides[14]; 2) reducing the side

reactions, which can result in less decomposition of active materials and electrolytes; 3) reduction of HF generation in the electrolyte solution.[53,56] On the other hand, Wang and coworkers[52,57,58] have shown that Al_2O_3 or YPO_4 particles increase the acidity of the electrolyte rather than scavenge the HF in the electrolyte, which can corrode the insulating surface species on $LiCoO_2$ and thus reduce electrode impedance. This discrepancy in the working mechanism limits the optimization of processes to stabilize lithium transition metal oxide electrodes. For example, the first mechanism points to the fact that the thickness and the uniformity of the coating layer are critical to enhance cycling performance[53] while the second mechanism[52,57-59] suggests that it is not essential for coating layer to be compact or to be on the surface of the active materials in order to reduce capacity loss during cycling. Understanding the origin in the enhancement mechanism associated with coating materials on the cycling performance is essential to develop strategies to increase the lifetime of lithium batteries.

There is a lack of fundamental understanding on the influence of coating on the surface composition and structure changes of lithium transition metal oxide particles during electrochemical cycling and aging. A number of inorganic and organic species have been detected or suggested on the surfaces of active particles during cycling or exposure to salt-containing electrolyte in the work of Aurbach et al.[55,60-65] Organic species such as $ROCO_2Li$ can be formed on the oxide surfaces due to nucleophilic reactions between oxide particles (negatively charged oxygen on the surface) and electrophilic alkyl carbonates in the solvents such as ethylene carbonate (EC) of the electrolyte.[60-63,65] In addition, LiF can form on cycled and aged Li_xCoO_2 in the $LiPF_6$-containing electrolyte as a result of chemical reactions between HF and $LiCoO_2$,[55] which can lead to considerable electrode impedance growth as LiF is very resistive to Li ion migration. It is of great interest to examine the effect of coating on the surface chemistry of Li_xCoO_2 electrodes, which could provide insights to the mechanism of enhanced cycling performance found for "$AlPO_4$"-coated $LiCoO_2$ electrodes. The effects of Al_2O_3 and $AlPO_4$ coating on the surface chemistry of Li_xCoO_2 electrodes cycled up to 4.4 V vs. Li have been studied by XPS[66] in some detail. Although coating is shown to reduce Co deposits on the negative electrode, no significant change in the surface composition and chemical environment of cycled Li_xCoO_2 is noted with coating addition. Such lack of

difference between the cycled coated and bare Li_xCoO_2 electrodes may be related to the relatively low upper cycling voltage limits of 4.2 V and 4.4 V used in this study, and to the fact that the electrodes were washed with dimethyl carbonate (DMC) prior to XPS analysis.[66] Our previous study[12] has shown that "$AlPO_4$"-coated $LiCoO_2$ particles, where Li_3PO_4 and $LiCo_{1-y}Al_yO_2$ with relatively high Al substitution levels are detected on active particles, exhibit significant enhancement in the capacitance retention upon cycling to 4.7 V in comparison to bare "$LiCoO_2$". In this study, we utilize synchrotron X-ray powder diffraction to probe the bulk changes of bare and "$AlPO_4$"-coated $LiCoO_2$ upon cycling to 4.7 V, and use X-ray photoelectron spectroscopy (XPS) to probe the changes in the surface chemistry induced upon cycling. We here discuss structural and surface compositional differences found in discharged bare and coated electrodes after cycling to 4.7 V vs. Li, from which a mechanism responsible for the enhancement in cycle life of "$AlPO_4$"-coated $LiCoO_2$ electrodes is proposed and tested.

2.2 Experimental Session

Bare "$LiCoO_2$" and "$AlPO_4$"-coated $LiCoO_2$ powder samples were prepared as described previously.[12] Bare "$LiCoO_2$" was prepared from stoichiometric amounts of Co_3O_4 and Li_2CO_3 heated at 1000°C for 4 hours in an oxygen stream. An $AlPO_4$-nanoparticle solution was prepared by slowly dissolving $Al(NO_3)_3 \cdot 9H_2O$ and $(NH_4)_2HPO_4$ in distilled water until a white $AlPO_4$-nanoparticle suspension was observed. The $AlPO_4$ nanoparticles with particle sizes in the range of 5-10 nm were amorphous, as determined by X-ray diffraction.[43] Bare "$LiCoO_2$" was added to this suspension and mixed thoroughly for 5 minutes. The slurry was dried in an oven at 120 °C for 6 hours and heat-treated at 700 °C for 5 hours, from which the "$AlPO_4$"-coated $LiCoO_2$ was obtained. The weight fraction of "$AlPO_4$" on $LiCoO_2$ is 1% after firing at 700 °C, as determined by inductively coupled plasma-mass spectroscopy (ICP-MS) (ICPS-1000IV, Shimadzu).

The reversible capacities and cycling stability of bare "$LiCoO_2$" and "$AlPO_4$"-coated $LiCoO_2$ composite electrodes were measured by using a two-electrode lithium cell (Tomcell Type TJ-AC). Preparation of composite electrodes had been described in detail elsewhere.[12] Lithium cells were constructed inside the glovebox using a lithium metal foil as

the negative electrode and the composite positive electrode separated by two polypropylene microporous separators (Celgard 2500). The electrolyte used was 1M $LiPF_6$ in a 1:1 volume ratio EC: DMC solvent (Kishida Chemical Corp). Assembled lithium cells were allowed to soak for 6~8 hours prior to electrochemical testing on a Solartron 1470 battery testing unit. Cycling characteristics of bare "$LiCoO_2$" and "$AlPO_4$"-coated $LiCoO_2$ electrodes were compared for two testing conditions. The first test was performed at a C/5 rate (bare: 0.12 mA/cm^2, coated: 0.16 mA/cm^2) between voltage limits of 3.0 V and 4.7 V vs. Li for 30 cycles after the first charge/discharge measured at a C/10 rate. The C-rate was defined based on the theoretical capacity of $LiCoO_2$ (274 mAh/g) in this study. The second test condition included galvanostatic cycling at a C/5 rate (bare: 0.29 mA/cm^2, coated: 0.36 mA/cm^2) between voltage limits of 2.5 V and 4.7 V vs. Li for 20 cycles, during which holding at 4.7 V was imposed for 4 hours each cycle. The cells were disassembled in an argon-filled glove box (< 5 ppm of H_2O and O_2), after which Li_xCoO_2 electrodes were extracted and stored in hermetically sealed containers in the glove box. The samples were then transported in these argon-filled containers for XPS and X-ray diffraction analyses. The discharged bare and coated electrodes cycled under the second test condition were examined by 1) JEOL 6320FV field-emission scanning electron microscopy (SEM) to investigate the changes in the surface morphology, 2) synchrotron X-ray diffraction to show the changes in the bulk crystal structure of $LiCoO_2$, and 3) XPS to reveal the changes in the surface compositions and chemical environments induced upon cycling. It should be noted that there are 10 wt.% of PVDF binder and 10 wt.% of Super P carbon in all of the pristine and discharged bare and coated electrodes. Therefore, the intensity of the signals from the binder and conductive additive are relatively higher in this study.

Synchrotron radiation of BL02B2 at SPring-8 (Sayo-gun, Hyogo, Japan), equipped with a large Debye-Scherrer camera[67] was used to collect X-ray diffraction data of the cycled electrode samples. The incident beam was adjusted to a wavelength of 0.5 Å by a Si(111) monochromator to minimize the absorption by the samples. The wavelength was calibrated to 0.5027 Å using a CeO_2 standard (S.G. $Fm\bar{3}m$, a = 5.4111(1) Å). The diffraction patterns were collected in the 2θ-range of 0 to 75°. A few milligrams of each sample were placed in a Linderman capillary (0.5 mm in diameter and approximately 2 cm in height)

during the measurement. X-ray diffraction data were recorded on an imaging plate for 20 min. Rietveld refinement analysis was performed using FullProf[68] in the 2θ-range of 10-45° (d-spacing of 2.87-0.65 Å).

The XPS spectra of bare "$LiCoO_2$" and "$AlPO_4$"-coated $LiCoO_2$ electrodes before and after cycling were measured using a Physical Electronics model 5400 X-ray photoelectron spectrometer. The samples were removed from the argon-filled containers, mounted onto a gold-coated sample holder, and transferred into the introduction chamber of the XPS spectrometer under ambient conditions in about two minutes. The introduction chamber was then immediately evacuated using a combination of roughing and turbomolecular pumps for about 10 to 15 minutes before transferring the sample to the XPS analysis chamber. The data were collected at room temperature using non-monochromatic Al K_a (1486.6 eV) X-ray source operating at 400 W (15 kV and 27 mA). The X-ray source is located at 54.7 degrees relative to the analyzer axis. All samples were analyzed at an electron takeoff angle of 45 degrees relative to the sample plane. It should be noted that the X-ray source and collection angle of 45° used in this experiment yield a sampling depth of ~ 5 nm for the O 1s photoemission line.[69] The samples were mounted onto a gold-coated sample holder with the aid of electrically conducting tabs, and were placed into the introduction chamber which was evacuated using roughing and turbomolecular pumps for about 10 to 15 minutes before being transferred into the analysis chamber of the XPS instrument. Data collection proceeded when the analysis chamber pressure reached ~$2x10^{-8}$ Torr. The size of the analysis area was set to a 1.1-mm-diameter spot. Survey spectra were collected at low resolution using analyzer pass energy of 89.45 eV, an increment of 0.5 eV/step, and an integration interval of 50 milliseconds/step. The final spectrum consisted of the average of 20 cycles. Multiplex spectra of various photoemission lines were collected at medium resolution using analyzer pass energy of 35.75 eV, an increment of 0.2 eV/step, and an integration interval of 50 milliseconds/step. Data collection intervals were approximately 37 minutes for survey spectra and ~100-200 minutes for each set of multiplex spectra depending on sample composition. Depth profile analysis was made using 4 KeV Ar ions with a raster size of 4x4 mm^2. The sputtering was made in one-minute intervals for a total sputtering time of 10 minutes for the bare electrode after 20 cycles and 20 minutes for the coated electrode after 20

cycles. The Li 1s, C 1s, O 1s, F 1s, Al 2s, Al 2p, P 2p, and Co 2p photoemission lines were collected after each interval of sputtering at constant analyzer pass energy of 71.0 eV, and an energy increment of 0.5 eV. The sputtering rate was calibrated using a 1000 Å SiO_2 film on a Si substrate and was found to be in the range of 35-40 Å of SiO_2 per minute.

The linearity of the spectrometer energy scale was calibrated using the Au $4f_{7/2}$ and Cu $2p_{3/2}$ photoemission lines of sputter-cleaned foils. The measured binding energies for these two lines were 83.93 and 932.59 eV, respectively, which compared well with the established values of 84.00 and 932.66 eV. The measured binding energies were shifted only by -0.07 eV with respect to the established values. To compensate for this small shift and sample charging effects, all spectra of powder samples were calibrated with the C 1s photoemission peak for adventitious hydrocarbons at 285.0 eV.[70] Spectra for the electrodes were calibrated with respect to the approximate average of the binding energies for carbon black and hydrocarbons at 284.6 eV since their C 1s spectra include contributions from carbon black and hydrocarbons. It should be mentioned that small differences in binding energy scale from sample to sample could arise due to inherent differences in binding energies of hydrocarbons present on different surfaces. The procedures for curve fitting analysis of photoemission lines are discussed in detail elsewhere.[12] The relative sensitivity factors for Li 1s, C 1s, O 1s, F 1s, Co $2p_{3/2}$, Al 2s, and P 2p photoemission lines were given as 0.028, 0.314, 0.733, 1.00, 2.113, 0.312, and 0.525, respectively. In order to identify the nature of the bonding environments for pristine and cycled bare and coated $LiCoO_2$ electrodes, a number of reference compounds, namely, aluminum phosphate ($AlPO_4$), layered O3 $LiAl_{0.1}Co_{0.9}O_2$, lithium carbonate (Li_2CO_3), gamma lithium phosphate (γ-Li_3PO_4), layered O3 lithium aluminum oxide ($LiAlO_2$), cobalt(II) fluoride (CoF_2), cobalt(III) fluoride (CoF_3), aluminum fluoride (AlF_3), lithium hexafluorophosphate ($LiPF_6$), Super P carbon powder, PVDF powder and 50 wt.% PVDF and 50 wt.% super P carbon composite electrode were used as standards for comparison. The X-ray powder diffraction patterns of some of the reference samples are shown in Figure 2-1.

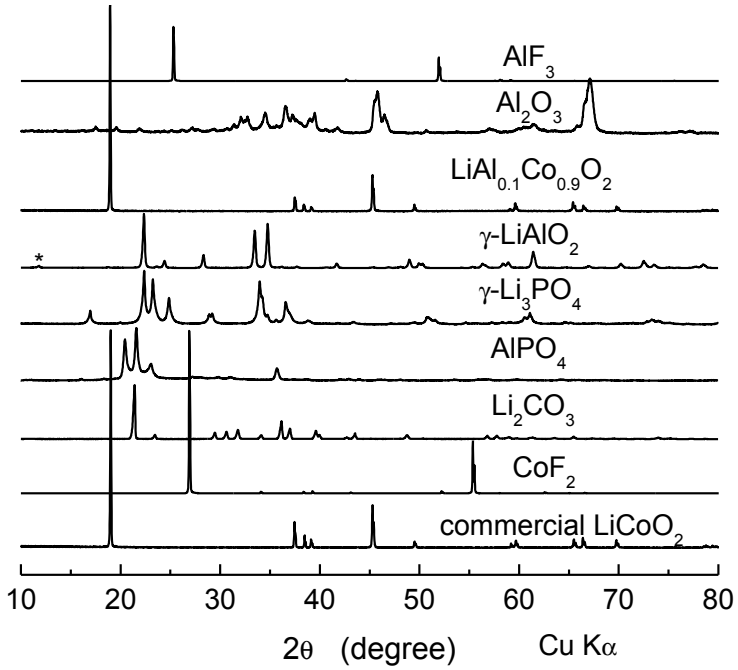

Figure 2-1. X-ray diffraction patterns for reference compounds used in the XPS analysis, including AlF_3 (Alfa Aesar, anhydrous, 99.5%), γ-Al_2O_3 (<50nm, Sigma-Aldrich), Li_3PO_4 (Alfa Aesar, Puratronic, 99.99%), $AlPO_4$ (Alfa Aesar, Puratronic, 99.99%), $LiAlO_2$ (Alfa Aesar), Li_2CO_3 (Alfa Aesar, Puratronic, 99.999%), CoF_2 (Alfa Aesar, 99.9%), and $LiAl_{0.1}Co_{0.9}O_2$, which was prepared by the solid-state method from $CoCO_3$, Li_2CO_3, and $Al(NO_3)_3$, heated at 500 °C for 1 hour and annealed at 900 °C for 12 hours. Commercial $LiCoO_2$ for additional test experiment is included. XRD measurements were performed on a Rigaku RU300 diffractometer with Cu K_α radiation at room temperature. Patterns were measured between 10-100° of 2θ, at a scan rate of 2.0 degrees/min. Symbol (*) indicates peak of a minor impurity phase.

2.3 Results and Discussion

2.3.1 Electrochemical Characterization

The galvanostatic voltage profiles of lithium cells having bare "$LiCoO_2$" and "$AlPO_4$"-coated $LiCoO_2$ electrodes reveal that the coated electrodes exhibit higher capacity in comparison to the bare electrode upon cycling to 4.7 V vs. Li, as shown in

Figure 2-2. This finding is in good agreement with previous studies.[12,18,41-46] It should be noted that the cell polarization grew considerably upon cycling, having that of cycled "$AlPO_4$"-coated $LiCoO_2$ much smaller than that of cycled bare. With a 4-hour holding at 4.7 V, the polarization of bare and coated $LiCoO_2$ electrodes became larger than those tested without holding. After cycling with 4.7 V holding, coated electrodes maintained greater capacity retention (~70% retention) in comparison to bare electrodes (~50% retention). It is hypothesized that smaller polarization and larger reversible capacity of coated electrodes relative to bare electrodes upon cycling to 4.7 V can be attributed to enhanced structural and surface stability of coated $LiCoO_2$ relative to bare, which will be examined in detail by SEM, synchrotron X-ray diffraction and XPS in the following sections.

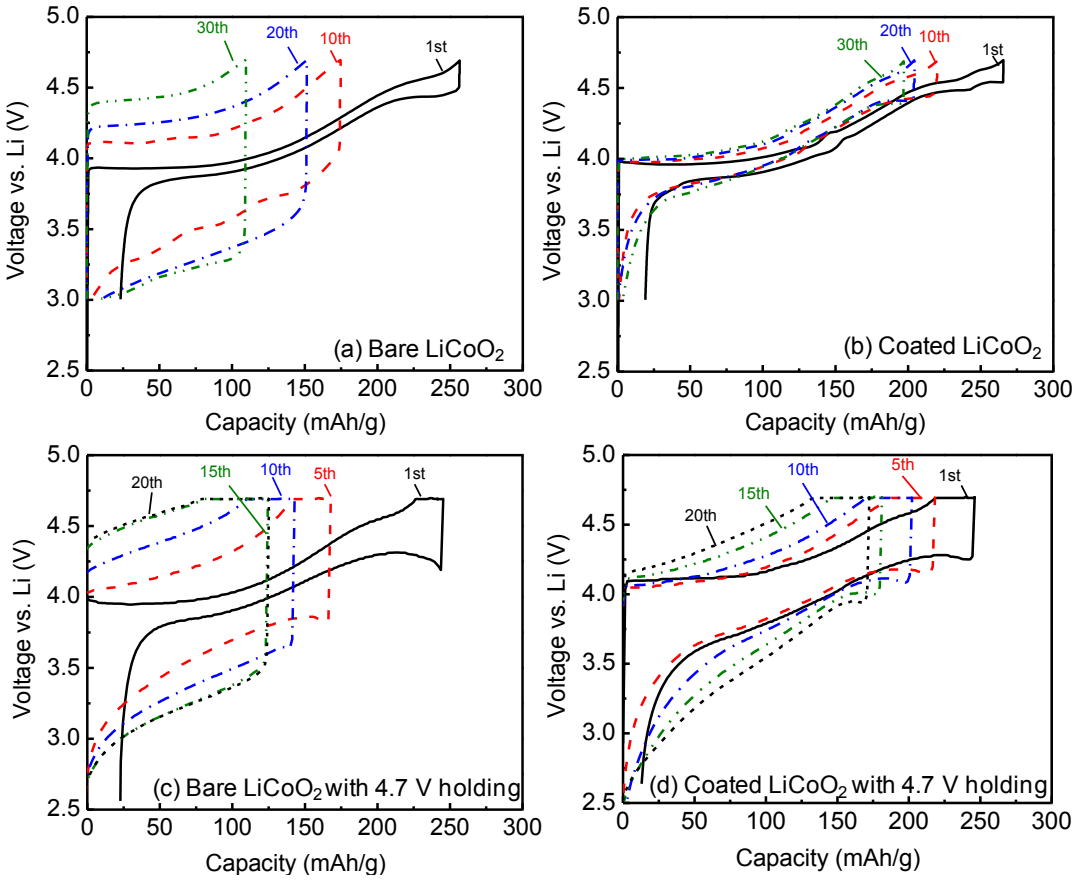

Figure 2-2. Voltage profiles of (a) bare "$LiCoO_2$" and (b) "$AlPO_4$"-coated $LiCoO_2$ during cycling between 3.0 and 4.7 V at a C/10 rate in the 1st cycle and a C/5 rate in the subsequent

cycles. (c) bare "$LiCoO_2$" and (d) "$AlPO_4$"-coated $LiCoO_2$ during cycling between 2.5 and 4.7 V at a C/5 rate with holding at 4.7 V for 4 hrs. The cycled electrodes in the discharge state were used for XPS characterization.

2.3.2 Microstructure Characterization-SEM Imaging

SEM secondary electron images of bare and "$AlPO_4$"-coated $LiCoO_2$ particles, before and after 20 cycles to 4.7 V with holding, are compared in Figure 2-3. Before cycling, the surfaces of the bare "$LiCoO_2$" particles appear to be fairly smooth, as shown in Figure 2-3a, whereas the surfaces of the "$AlPO_4$"-coated $LiCoO_2$ particles are rough, as shown in Figure 2-3b. Our previous observations[12] have shown that the coating thickness varies on the micrometer scale with variations in the range of 10 nm to 100 nm. Interestingly, the surfaces of the cycled bare "$LiCoO_2$" particles in the discharged state were found to remain smooth after 20 cycles (Figure 2-3c). In contrast, a large number of additional deposits were found on the surfaces of cycled coated $LiCoO_2$ particles (Figure 2-3d) to the original surface morphologies (Figure 2-3b). The chemical nature of these new deposits in the cycled coated electrodes will be discussed in the context of the XPS results.

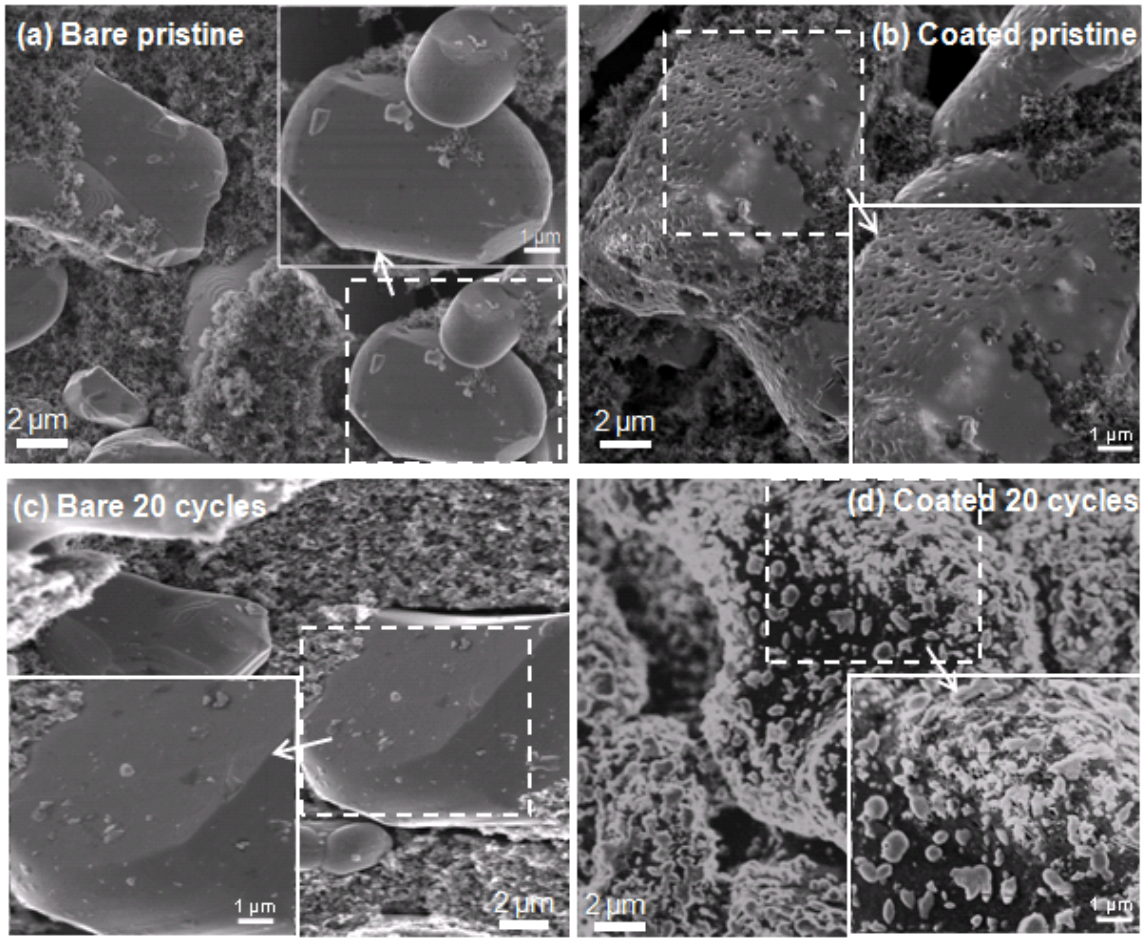

Figure 2-3. Scanning electron micrographs of (a) bare "$LiCoO_2$" pristine electrode and (b) "$AlPO_4$"-coated $LiCoO_2$ pristine electrode. The coated particles show pitted textures on the surface. (c) bare "$LiCoO_2$" after 20 cycles to 4.7 V with holding and (d) "$AlPO_4$"-coated $LiCoO_2$ after 20 cycles to 4.7 V with holding. No apparent changes for the bare samples after cycling, whereas many newly formed patches were found on the surfaces of the coated particles after cycling.

2.3.3 Synchrotron Powder X-ray Diffraction Analysis

The changes in the bulk crystal structure of bare and coated Li_xCoO_2 electrodes before and after cycling to 4.7 V with holding were examined by synchrotron X-ray diffraction. Figures 2-4 shows highlighted synchrotron X-ray diffraction patterns of pristine and cycled bare and coated electrodes in the discharged state, where Bragg reflections

are indexed to a hexagonal unit cell with rhombohedral symmetry having space group $R\bar{3}m$. The crystallographic parameters of pristine and cycled, bare and coated $LiCoO_2$ in the rhombohedral symmetry were obtained from the Rietveld refinement of the diffraction data, as shown in Table 2-1. The lithium content in Li_xCoO_2 of cycled electrodes was estimated from the refined X-ray diffraction results and the open-circuit voltages (OCV) of the cells. We have previously shown that the coated $LiCoO_2$ exhibits a voltage plateau and a two-phase reaction upon initial lithium de-intercalation,[12] which is characteristic of stoichiometric $LiCoO_2$,[71-74] whereas bare "$LiCoO_2$" exhibits a slopping voltage profile and a single-phase reaction upon lithium de-intercalation, which suggests that bare "$LiCoO_2$" is lithium over-stoichiometric. The OCV result of the coated Li_xCoO_2 (Figure 2-5) shows that the two-phase region starts from x = ~0 and ends at x = ~0.75 while that of the bare Li_xCoO_2 reveals a single-phase region in the same lithium compositional window. Neither changes in the crystallographic parameters of the hexagonal unit cell of cycled coated electrodes relative to the pristine electrode nor the appearance of a secondary phase of $Li_{0.75}CoO_2$ was detected. Therefore, the lithium content of the discharged coated $LiCoO_2$ after 20 cycles is estimated to be close to 1. In contrast, the unit cell dimension along the $\boldsymbol{c}_{hex.}$ axis was increased slightly from the pristine (14.040 Å) to the cycled bare electrode in the discharged state (14.073 Å). Comparison with the lattice parameter changes of Li_xCoO_2 as a function of lithium content x reported by Levasseur et al.[75] suggest that the discharged bare electrode after 20 cycles has a lithium content of ~0.9 per unit formula.

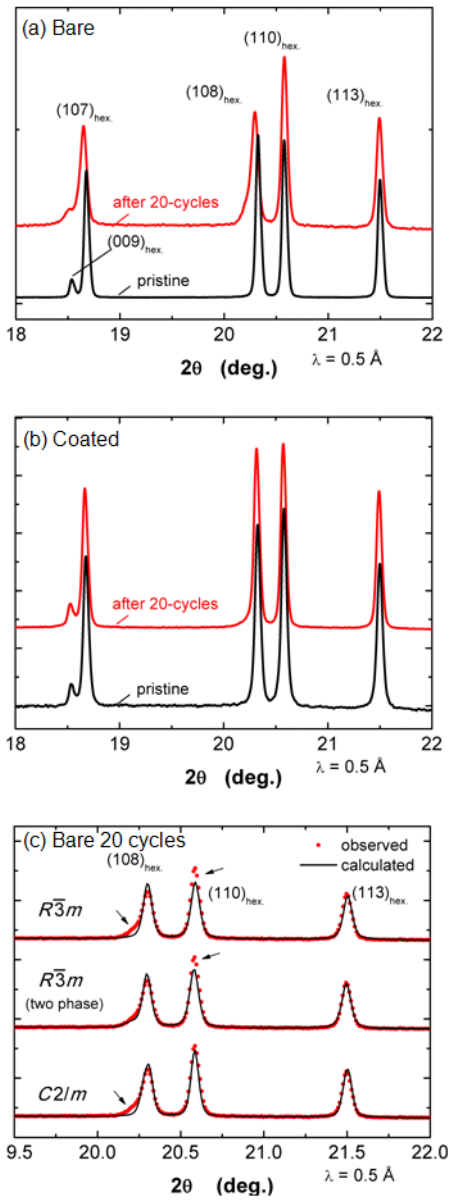

Figure 2-4. Synchrotron X-ray diffraction patterns, before and after cycling to 4.7 V with holding of (a) bare and (b) "$AlPO_4$"-coated $LiCoO_2$ electrodes. No apparent change was found for the coated electrode after 20 cycles, whereas peak broadening was noted for the bare sample after 20 cycles, indicating structural damage to Li_xCoO_2 upon cycling (c) Comparison of experimental X-ray diffraction pattern of the bare "$LiCoO_2$" after 20 cycles with calculated patterns of single-phase with space group R $\bar{3}$m, mixture of two R $\bar{3}$m phases and single-phase with space group C2/m.

Table 2-1. Crystallographic parameters for the pristine bare and coated electrodes, and the cycled bare and coated electrodes after 20 cycles obtained from the Rietveld analysis.

Material			bare electrode	bare 20 cycles		coated electrode	coated 20 cycles
space group			$R\bar{3}m$	$R\bar{3}m$	$C2/m$	$R\bar{3}m$	$R\bar{3}m$
lattice constants	$a_{hex.}$ (Å)		2.81288(1)	2.81308(1)	$a_{mono.}$ = 4.8742(2) $b_{mono.}$ = 2.8130(1)	2.81288(1)	2.81291(1)
	$c_{hex.}$ (Å)		14.0403(4)	14.0734(6)	$c_{mono.}$ = 4.9612(1) β = 108.988(4)°	14.0413(4)	14.0461(4)
Wyckoff position	3a site	Co (g)[a]	1.0	1.00	1.0 (2a site)	1.0	1.0
		B (Å^2)[a]	0.20	0.20	0.20	0.20	0.20
	3b site	Li (g)[a]	1.0	1.0	1.0 (2d site)	1.0	1.0
		B (Å^2)[a]	1.00	1.00	1.00	1.00	1.00
	6c site	O (g)[a]	1.0	1.0	1.0 (4i site)	1.0	1.0
		B (Å^2)	0.36(6)	0.55(9)	0.61 (8)	0.30(7)	0.41(6)
positional parameter for 6c site[b]			0.2603(4)	0.2608(4)	x = 0.238(1) z = 0.218(1)	0.2603(4)	0.2601(4)
Interatomic distance Co-O (Å)			1.921	1.918	1.921	1.921	1.922
R_{wp} (%)			17.9	19.0	18.0	17.0	16.6
R_B (%)			6.18	9.29	9.00	6.99	5.81

[a] not refined

[b] oxygen positions are (0, 0, z) for $R\bar{3}m$ and (x, 0.5, z) for $C2/m$

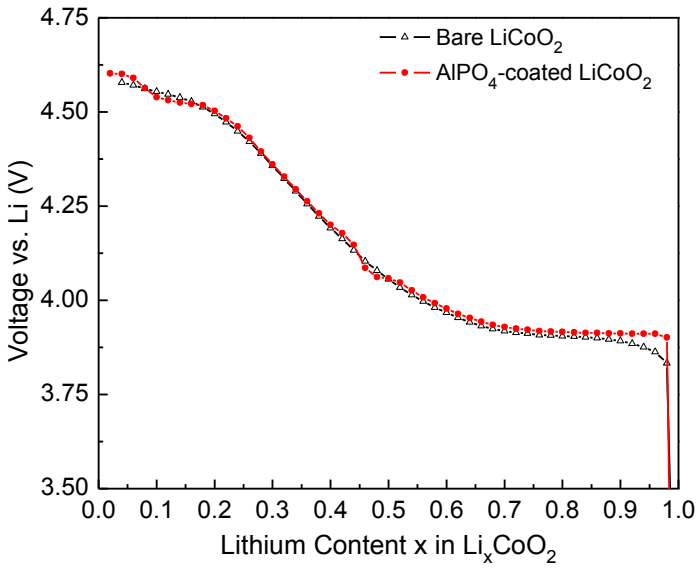

Figure 2-5. Open-circuit voltages (OCV) of the bare and coated $LiCoO_2$ as a function of Li content per unit formula. The data were collected in a two-electrode cell with lithium as the counter electrode.

It should be noted that the $(10l)_{hex.}$ peaks of the cycled bare Li_xCoO_2 was broadened selectively toward lower diffraction angles after 20 cycles, as shown in Figures 2-4a and 2-4c. For example, a peak shoulder toward the lower diffraction angles was very apparent for the $(108)_{hex.}$ reflection. Such broadening would not have been detectable using conventional laboratory diffractometers. In contrast, the peak profiles of all Bragg reflections for discharged coated $LiCoO_2$ remained unchanged after the cycling in Figure 2-4b. In order to examine and gain some insights into the origin of the observed peak broadening, the following structural analysis has been performed on the cycled bare "$LiCoO_2$". We applied two models, 1) a mixture of two $R\bar{3}m$ phases, and 2) a monoclinic phase with space group C2/m. The observed and calculated intensities for these models are compared in Figure 2-4c. Although the observed peak shoulder can be simulated well using the two-phase model having the volume fraction of the secondary phase less than 10 %, the observed intensity of the $(110)_{hex.}$ peak cannot be fitted satisfactorily, as shown in Figure 2-4c. On the other hand, the application of the monoclinic model with space group C2/m was found to slightly improve the Rietveld refinement results in comparison to the single $R\bar{3}m$ phase, as shown in Table 2-1. However, these selectively broadened Bragg peaks could not be explained fully with the monoclinic phase, as shown in Figure 2-4c. We further discuss if proton insertion and/or oxygen loss is likely to give rise to the selective peak broadening. Several studies have shown that proton exchange for Li^+ in $LiCoO_2$ particles in acid,[76,77] where protons occupying prismatic sites instead of octahedral sites can lead to shearing of oxygen lattice from ABCABC (O3 oxygen stacking) to ABBCCA (P3 oxygen stacking).[78] However, slabs with protons on the prismatic sites have smaller interslab distance relative to $LiCoO_2$, which would lead to selective peak broadening toward higher diffraction angles (not lower diffraction angles as observed in Figure 2-4). Therefore, the observed peak broadening is unlikely from proton exchange for Li in $LiCoO_2$. Although the origin of the peak broadening observed in cycled bare electrode is not fully understood, it is hypothesized that oxygen loss can give rise to the selective peak broadening observed for the cycled bare electrode. This hypothesis is supported by the fact that the isotropic displacement parameter of oxygen on the 6c site became larger in the cycled bare electrode than pristine bare when the occupancy of the oxygen was fixed, which indicates lowered local symmetry for MeO_6 octahedron and/or

decreased oxygen occupancy at this site if the occupancy was allowed to vary. Further electron diffraction and high-resolution TEM imaging studies are needed to test this hypothesis.

2.3.4 X-ray Photoelectron Spectroscopy Analysis

Pristine bare and coated electrodes, and cycled bare and coated in the discharged state. The XPS spectra of pristine and discharged bare and coated $LiCoO_2$ electrodes after 1 and 20 cycles as well as reference materials are shown in Figures 2-6 to 2-18. The XPS results reported here for pristine and cycled bare and coated electrodes were reproducible at least on three different electrodes in each case. It is noted that phase identification for complex electrode surfaces, based solely on XPS investigations, is not conclusive without further support from other techniques such as energy dispersive spectroscopy in scanning transmission electron microscope at liquid nitrogen temperature and vibration spectroscopy. The reported phases, hereafter, were selected to represent, as closely as possible, the appropriate oxidation states and concentrations of various elements present in the surface region.

C 1s Region. The C 1s photoemission spectra of pristine and discharged electrodes after 1 and 20 cycles for bare and coated $LiCoO_2$ are shown in Figure 2-6. These spectra, except the one for the coated electrode after 20 cycles, are dominated by a contribution from Super P carbon black followed by a contribution from PVDF. The reference spectra of Super P carbon black, PVDF and a composite electrode of 50 wt.% PVDF and 50 wt.% Super P carbon (Figure 2-7) were used as reference sample to deconvolute the spectra of composite electrodes. First, an asymmetric peak at 284.6 eV due to C-C bonding and a very broad peak with relatively lower intensity (5~10% of main peak)[79] at ~ 290.5 eV due to the shake-up satellite structure can be attributed to carbon black. C-H bonds or adventitious hydrocarbons with binding energy around 285.0 eV, is considered to have a relatively small contribution in the C 1s region shown in Figure 3-6a to Figure 3-6e due to the fact that the first component shows similar characteristics to those of carbon black (highly asymmetric and narrow peak with a FWHM less than 1.5 eV). Second, a peak at ~286.2

eV can be attributed to carbon atoms singly bound to oxygen (C-O)[80] and the CH_2 in PVDF.[66] Third, a peak near 287.6 eV can be related to carbon atoms bound to two oxygen atoms with two single bonds (O-C-O)[80] or bound to one oxygen with a double bond (C=O).[80,81] Fourth, a peak near 289.0 eV can be related to carbon bound to two oxygen atoms as in the carboxylic group (O-C=O).[80] Lastly, a peak located at 290.8 eV can be related to the CO_3 group in Li_2CO_3 (~290.3 eV[82]) for pristine bare and coated $LiCoO_2$ particles and/or surface organic films consisting of species such as $ROCO_2Li$ (~290.1 eV[83]) for cycled electrodes, and carbon atoms bound to two fluorine atoms (CF_2 in PVDF). The amounts of oxidized carbon species slightly increased relative to aliphatic carbon (the 284.6 eV component) upon cycling of bare electrodes. In contrast, the contribution from carbon black at 284.6 eV decreased significantly in the coated electrode after 20 cycles relative to pristine coated electrode. Instead a relatively broader peak (FWHM of ~2.38 eV) near 285.0 eV was clearly recognized, which can be attributed to adventitious hydrocarbon. The significant decrease in the carbon black signal and the dominance of the hydrocarbon signal indicates that the surface film developed on the coated electrode after 20 cycles is much thicker than for the bare electrodes.

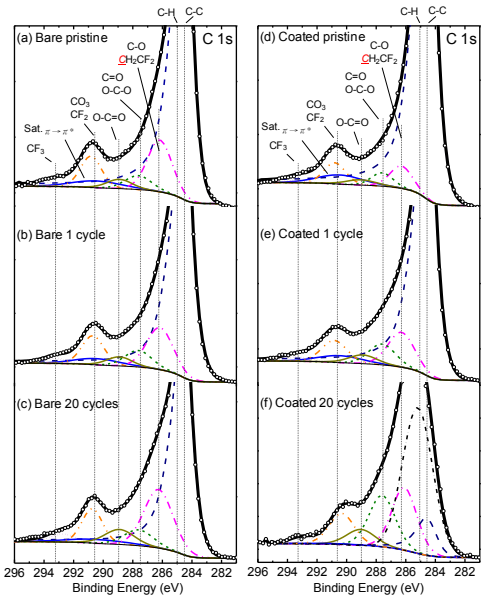

Figure 2-6. XPS spectra of the C 1s photoemission line for bare "$LiCoO_2$" in the condition of (a) pristine electrode, (b) after 1 cycle, (c) after 20 cycles, and "$AlPO_4$"-coated $LiCoO_2$ in the condition of (d) pristine electrode, (e) after 1 cycle, (f) after 20 cycles.

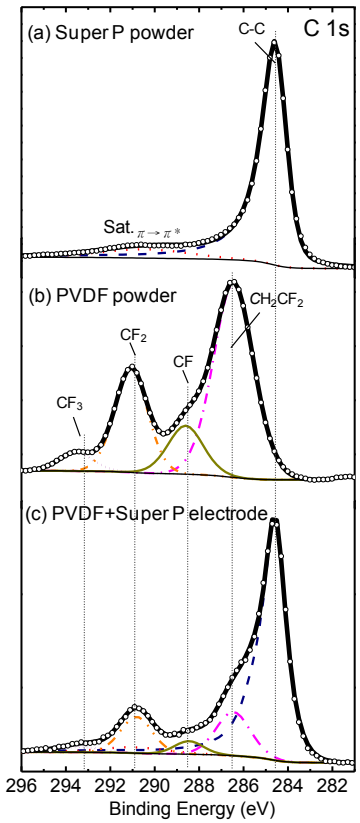

Figure 2-7. Reference XPS spectra of C 1s photoemission line for (a) Super P carbon powder, (b) Poly(vinylidene fluoride) powder, and (c) 50 wt.% carbon + 50 wt.% PVDF composite electrode. Carbon black shows one asymmetric peak at 284.6 eV with long tail extended to high energy region. Another component at ~290.5 eV was recognized as the shake-up satellite structure ($\pi \rightarrow \pi^*$ transition) of carbon black. PVDF powder shows two main components at ~286.4 eV and ~291.0 eV which are attributed to CH_2 and CF_2 in PVDF. Two noticeable peaks located at ~288.5 eV and 293.3 eV are related to the –CF (Mariana D. et al., *J. Appl. Polym. Sci.* **67**, 2125-2129, (1998)) and $-CF_3$ (Sultana, T. et al., *Appl. Surf. Sci.* **255**, 2569-2573, (2008)) groups which might be associated with X-ray damage.

Co 2p Region. The Co 2p photoemission spectra of pristine and discharged electrodes after 1 and 20 cycles for bare and coated $LiCoO_2$ are shown in Figure 2-8. The spectra of pristine bare and coated electrodes reveal a $2p_{3/2}$ peak and a $2p_{1/2}$ peak at ~780 eV and ~795 eV, respectively. Shake-up satellite peaks for each line are located at ~9.7 eV higher

relative to the main component. The locations and line shapes of the main peaks and their satellites of pristine electrodes indicate that cobalt ions are in the trivalent state.[84] The Co 2p spectra of cycled bare electrodes after 1 and 20 cycles were found similar to those of pristine bare "$LiCoO_2$" indicating that there was no apparent change in the Co oxidation state after cycling.

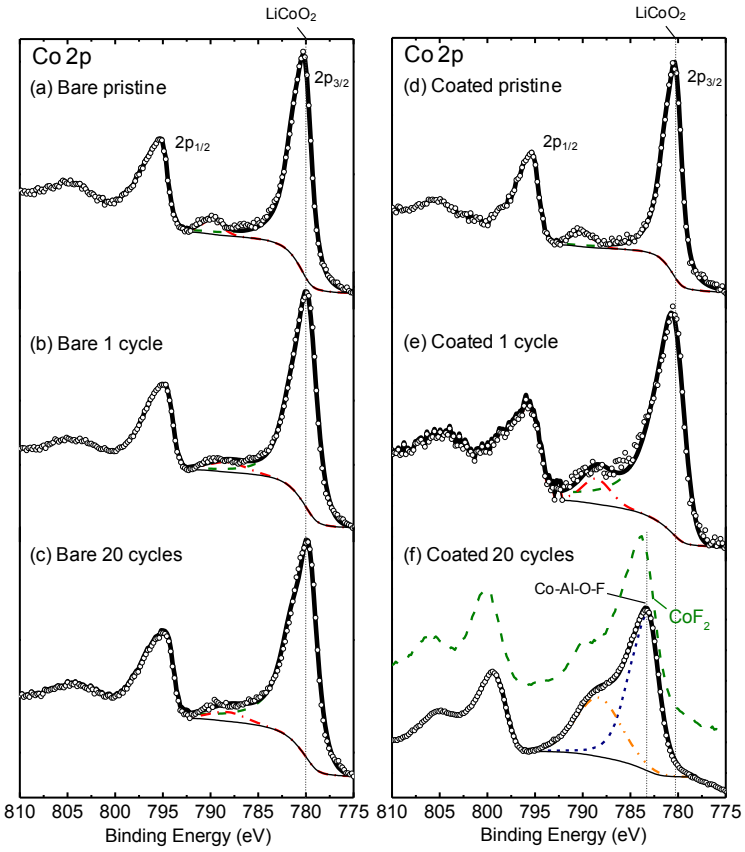

Figure 2-8. XPS spectra of the Co 2p photoemission line for (a) pristine bare "$LiCoO_2$" electrode, (b) after 1 cycle, (c) after 20 cycles, (d) pristine "$AlPO_4$"-coated $LiCoO_2$ electrode, (e) after 1 cycle, and (f) after 20 cycles.

In contrast, the Co 2p spectrum for the discharged coated electrode after 20 cycles is considerably different from that of the pristine coated electrode. First, the binding energy of the Co $2p_{3/2}$ line shifts from 780.4 eV for the pristine coated electrode to ~783.1 eV for the coated electrode after 20 cycles. Second, the spectrum of the coated electrode after 20 cycles displays an intense satellite structure at ~5.2 eV higher relative to the ~783.1 eV

peak. The higher binding energy for the discharged coated electrode after 20 cycles relative to that of pristine coated electrode and the intense satellite structure with a 5.2 eV shift higher relative to the main peak can be attributed to Co bound to fluorine atoms, which indicates the formation of Co-containing fluoride and/or oxyfluoride species. This assignment was confirmed by the similarity in the Co 2p spectra between the discharged coated electrodes and a CoF_2 powder reference, which is shown in Figure 2-8f.

Figure 2-8 shows the Co 2p photoemission spectra of discharged bare and coated electrodes after 20 cycles as a function of sputtering time. For the discharged bare electrode, only small changes were found in the shake-up structure upon sputtering, where the increased shake-up intensities could be attributed to the formation of CoO by the reduction of Ar beam during sputtering.[85] This observation suggests that there is no detectable difference in the cobalt valence state between the surface and bulk of cycled bare electrodes in the discharge state. On the other hand, the intensity of the higher binding energy component observed for the discharged coated electrode, which was attributed to Co bound to fluorine atoms, decreased with increasing sputtering time. The presence of Co-containing fluoride and/or oxyfluoride species can be related to the additional patches revealed by SEM on the surfaces of coated $LiCoO_2$ after cycling (Figure 2-3). The intensity of a lower binding energy peak near 779.5 eV, which corresponds to the Co^{3+} in $LiCoO_2$, became visible after only 1 minute of sputtering and its intensity increased with sputtering time. This result further supports the hypothesis that Co-containing fluoride and/or oxyfluoride species covers the surface of discharged coated Li_xCoO_2 after cycling to 4.7 V. Although how these fluoride and/or oxyfluoride species are formed on coated Li_xCoO_2 during cycling is not understood, it is interesting to mention that Markovsky et al.[86] have shown that adding Co^{2+} ions in the electrolyte leads to the formation of cobalt fluorides on the surface of Li_xCoO_2 cycled and aged in the $LiPF_6$-containing electrolyte.

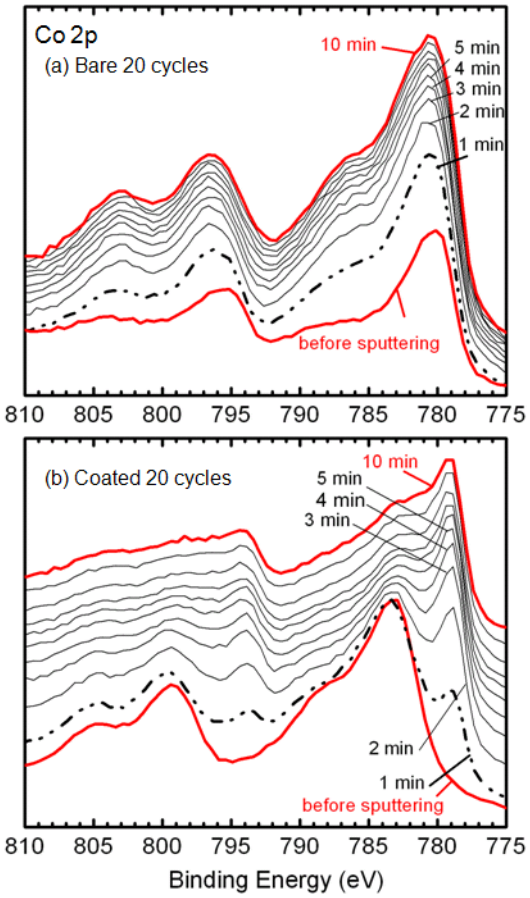

Figure 2-9. XPS depth profiles of the Co 2p photoemission line for (a) bare "$LiCoO_2$" after 20 cycles, (b) "$AlPO_4$"-coated $LiCoO_2$ after 20 cycles.

An estimate for lithium content and subsequently the valence state of Co in the discharged state of Li_xCoO_2 can be made from the area of the satellite peak relative to that of the of Co 3p main line following the procedure reported by Daheron et al.[87] On this basis[87], the discharged bare electrode after 20 cycles has a lithium content of ~0.9 per unit formula as shown in Figure 2-10, which is in agreement with the estimation from the synchrotron X-ray diffraction and OCV results discussed earlier in this paper. As the surface of discharged coated electrode after 20 cycles was covered largely by Co-containing fluoride and/or oxyfluoride species, this method is not appropriate to estimate the cobalt valence state in this case. It should be noted that we find no evidence for the presence of Co_3O_4 on the surface of cycled $LiCoO_2$ as suggested by previous studies[57,65] as broadening of the Co $2p_{3/2}$ line and shake-up structure expected for Co_3O_4 with Co^{2+} and

Co^{3+}[88] relative to $LiCoO_2$ were not observed in this work. This result is in agreement with previous XPS findings of electrochemically deintercalated Li_xCoO_2 (x varies from 1 to 0)[87] and Li_xCoO_2 cycled to 4.4 V.[66] In addition, we find no evidence for the presence of surface CoO or $Co(OH)_2$ for pristine and cycled bare and coated electrodes. The Co 2p binding energies for both CoO and $Co(OH)_2$ (XPS reference samples used in this study) are significantly lower than those of CoF_2 while their characteristic shake-up structures is much more intense than that of $LiCoO_2$ and are also shifted only by 7.0 and 6.1 eV, respectively, relative to the main line, which are significantly less than the 10 eV shift in the case of $LiCoO_2$.

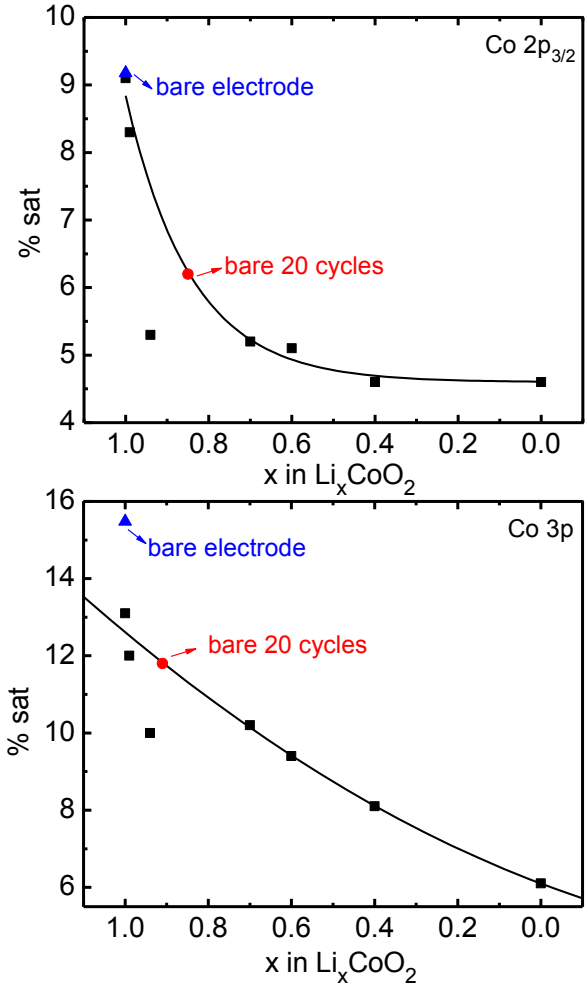

Figure 2-10. Comparison of the satellite relative area (%) from Co $2p_{3/2}$ and Co 3p core peaks of bare "$LiCoO_2$" pristine electrode and after 20 cycles. The Li content of bare Li_xCoO_2

electrode after 20 cycles can be estimated as ~0.9 per unit formula. The square datapoints were extracted from a previous study (Daheron, L. et al., *Chem. Mat.* **20**, 583-590, (2008)).

F 1s Region. The F 1s photoemission spectra of pristine and discharged electrodes after 1 and 20 cycles for bare and coated $LiCoO_2$ are shown in Figure 2-11. The F 1s spectra of pristine bare (Figure 2-11a) and coated (Figure 2-11d) electrodes were deconvoluted into two components. An intense component at 688.0 eV is assigned to fluorine atoms in PVDF. This assignment is in good agreement with the F 1s binding energy of a reference sample having a mixture of PVDF and Carbon as shown in Figure 2-12. A weak component was found around 685.0 eV, which could be attributed to LiF (685.0 eV[66]). It is hypothesized that HF can be generated via a dehydrofluoination reaction in the PVDF binder, and then react with $LiCoO_2$ or Li_2CO_3 to form LiF.[89] For the bare electrodes after 1 and 20 cycles and the coated electrode after 1 cycle, the F 1s spectra were deconvoluted into three components at ~688.0 eV, ~686.6 eV and ~685.5 eV.

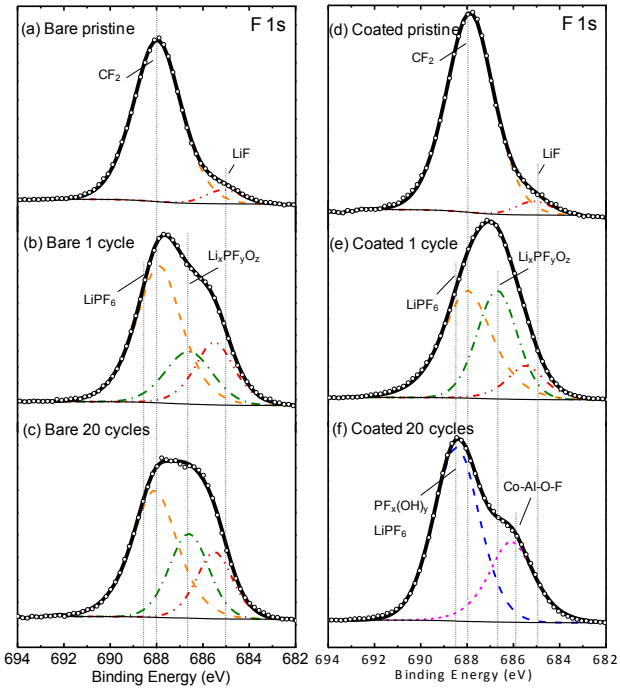

Figure 2-11. XPS spectra of the F 1s photoemission line for bare "$LiCoO_2$" in the condition of (a) pristine electrode, (b) after 1 cycle, (c) after 20 cycles and "$AlPO_4$"-coated $LiCoO_2$ in the condition of (d) pristine electrode, (e) after 1 cycle, (f) after 20 cycles.

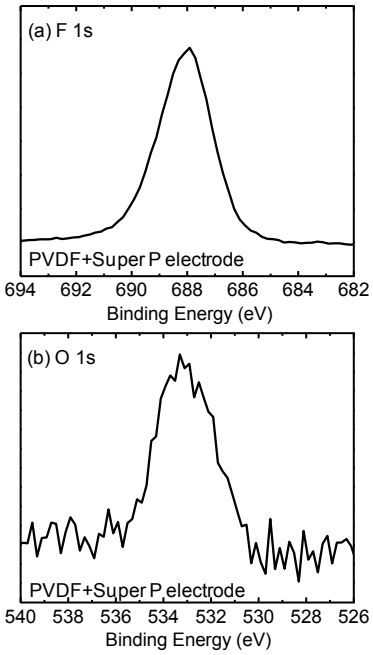

Figure 2-12. XPS spectra of the (a) F 1s and (b) O 1s photoemission line for 50 wt.% carbon + 50 wt.% PVDF composite electrode.

The high-energy component at 688.0 eV can be attributed to PVDF (~688.0 eV) and $LiPF_6$ (~688.5 eV confirmed by a reference sample in this study). The intermediate-energy component at ~686.6 eV can be attributed to $LiPF_6$ degradation intermediates such as $Li_xPF_yO_z$.[66] It should be noted that this peak may include a contribution from $LiPF_6$ degradation products due to X-ray exposure during the XPS measurements. The low-energy component at ~685.5 eV can be attributed to LiF and other metal fluorides[86] and/or oxyfluoride species. For the coated electrode after 20 cycles, the F 1s spectrum was deconvoluted into two components. The component at 686.0 eV is assigned to the fluorine atoms in the form of Co-containing fluoride and/or oxyfluoride species. This assignment is consistent with the observed F 1s binding energy of 686.0 eV for a CoF_2 reference sample in this study. The high binding energy component of the F 1s line (688.5 eV), which contributes ~26.8 at.% to the composition, cannot be attributed fully to $LiPF_6$ and PVDF. Based on the composition and binding energy considerations, it is believed that this component likely includes contributions from PF_xO_y (e.g., OPF_3 and O_2PF) and/or $PF_x(OH)_y$ (e.g., $(OH)PF_4$, $(OH)_2PF_3$, $(OH)_3PF_2$, or $(OH)_4PF$). However, the F 1s binding energy reported for PF_xO_y ($LiPF_6$ decomposition products such as POF_3) is ~687 eV, its binding energy can be higher if

the oxygen also binds to a hydrogen atom. Therefore, $PF_x(OH)_y$ appears to be a better candidate. In addition, a small amount of HF left on the surface cannot be excluded. However, since XPS cannot detect H, definitive confirmation of HF cannot be made. Detailed comparisons of surface chemical compositions of different species would be discussed in details in a later section.

O 1s Region. The O 1s photoemission spectra of the pristine and discharged electrodes after 1 and 20 cycles for bare and coated $LiCoO_2$ are shown in Figure 2-13. The spectra of pristine bare and coated electrode consist of three components. First, the low-energy peak at ~529.7 eV can be attributed to lattice O^{2-} ions in the O3 layered $LiCoO_2$ structure. The second peak at ~532.0 eV can be attributed to surface defects associated with oxygen oxidation states less negative than O^{2-} ions[84,90] and more covalent Co-O bonds[91] on the "$LiCoO_2$" particle surface. In addition, the oxygen atoms in Li_2CO_3 (532.1 eV[12]) and oxygen atoms doubly bound to carbon atoms (532.0 eV) should also be considered in this component. A contribution from Li_3PO_4 (~531.6 eV[12]), which is present on the surface of pristine "$AlPO_4$"-coated $LiCoO_2$,[12] was also considered. The third component at 533.5 eV can be related to oxygen bound to carbon with a single bond as in ester groups.[81,92]

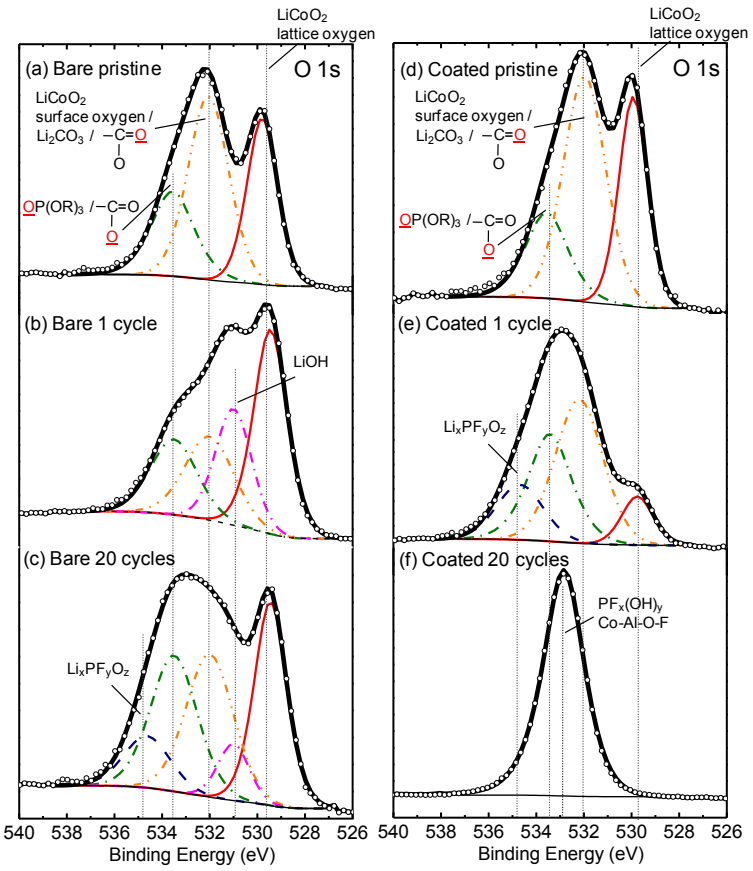

Figure 2-13. XPS spectra of the O 1s photoemission line for bare "$LiCoO_2$" in the condition of (a) pristine electrode, (b) after 1 cycle, (c) after 20 cycles and "$AlPO_4$"-coated $LiCoO_2$ in the condition of (d) pristine electrode, (e) after 1 cycle, (f) after 20 cycles.

For the discharged bare electrodes, a peak near 531.0 eV appeared after 1 cycle and its intensity decreased after 20 cycles. This component can be related to metal hydroxide groups such as $Co(OH)_2$ (530.8 eV[93]) or LiOH (531.1 eV[93]). However, Co environment in $Co(OH)_2$ was excluded since the Co 2p region for the discharged bare electrodes clearly show that the cobalt ions remained in the trivalent state.[84] Therefore, the oxygen component at 531.0 eV is likely due to LiOH, which could be formed by the reaction of OH^- (due to trace amount of water in the electrolyte) with Li^+ on the particle surface.[94] Upon cycling of bare electrode to 20 cycles, the carbonates species, which could develop from reactions between Li_xCO_2 and the electrolyte, were found to increase, as evidenced by the increased peak intensities at 532.0 eV (Li_2CO_3 and oxygen atoms forming a double bond with the carbon in

Li alkyl carbonates ROCO_2Li[83]) and at ~533.5 eV (oxygen atoms forming a single bond with the carbon in Li alkyl carbonates ROCO_2Li,[83] $OP(OR)_3$[66] and polycarbonate-type compounds[66]). A peak at very high binding energy of ~534.6 eV, which appeared after 20 cycles, was attributed to the oxygen atoms in fluorophosphate intermediates, namely $Li_xPF_yO_z$.[95]

For the cycled coated electrodes, a peak at ~532.8 eV grew upon cycling and became dominant after 20 cycles, as shown in Figure 2-13e to Figure 2-13f. This peak cannot be assigned to Li_2CO_3 as the binding energy of this component is not in good agreement with that of Li_2CO_3 and the two contributions of lithium alkyl carbonates,[83] and there are not enough oxidized carbon atoms to account for all of the oxygen atoms in the form of carbonates. As the O 1s binding energies of metal oxyfluoride species such as Al-O-F (~532.7 eV)[96] and Si_xOF_y[97] (~532.9 eV) and $PF_x(OH)_y$ like species such as $(OH)PF_4$, $(OH)_2PF_3$, $(OH)_3PF_2$, or $(OH)_4PF$. However, based on the surface composition analysis, $(OH)_2PF_3$ appears to be the most likely candidate. The O 1s line of the coated electrode after 20 cycles is ~532.8 eV. It is reasonable to speculate that $PF_x(OH)_y$ has O 1s binding energy higher than pure hydroxides (typically in the range of 531.0-531.5 eV) as the presence of fluorine can increase its binding energy. For example, the binding energy of the O 1s line increased from 531.5 eV for $Al(OH)_3$ to 533.0 eV for $Al(OH)_{0.7}F_{2.3}$.[98] It should be noted that the peak corresponding to lattice oxygen in $LiCoO_2$ at ~529.6 eV is no longer detectable in the spectrum for the discharged coated electrode after 20 cycles (Figure 2-13f) while it is visible in the spectrum for the discharged bare electrodes after 20 cycles (Figure 2-13c). The absence of lattice oxygen and the significant reduction in the intensity of the carbon black signal for the coated electrode after 20 cycles are consistent with the formation of a surface film covering the pre-cycled surface.

Figure 2-14 shows the O 1s photoemission spectra for the discharged bare and coated electrodes after 20 cycles as a function of sputtering time. For the discharged bare electrode, the intensity of components in the energy range from ~531 eV to ~534 eV decreased relative to that of lattice O^{2-} component upon sputtering, and was diminished after 3 minutes of sputtering. Similarly, the intensity of the surface oxygen peak of the discharged coated electrode decreased relative to that of lattice O^{2-} peak with sputtering time but

remained visible after 10 minutes of sputtering. This observation further confirms that the surface film developed on the discharged coated electrode after 20 cycles is considerably thicker than that on the discharged bare electrode.

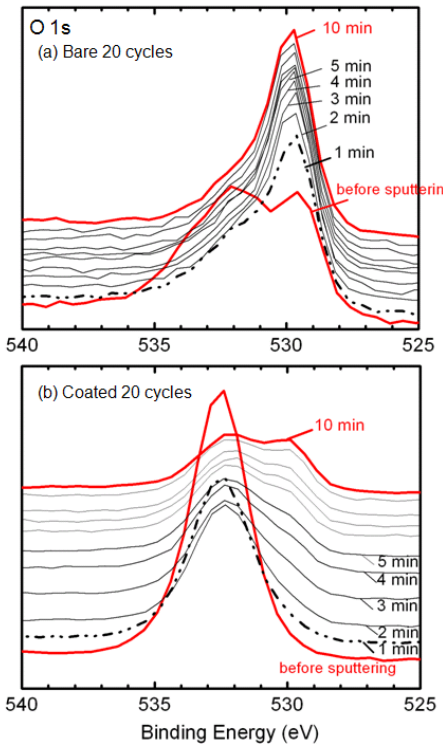

Figure 2-14. XPS depth profiles of the O 1s photoemission line for (a) bare "$LiCoO_2$" after 20 cycles, (b) "$AlPO_4$"-coated $LiCoO_2$ after 20 cycles.

P 2p Region. The P 2p photoemission spectra of pristine and discharged electrodes after 1 and 20 cycles for bare and coated $LiCoO_2$ are shown in Figure 2-15. The spectra for the discharged bare electrodes after 1 cycle and 20 cycles show three contributions with the following binding energies: 1) ~133.5-134 eV, which can be assigned to phosphate species such as $OP(OR)_3$[66] resulting from degradation of $LiPF_6$; 2) ~136 eV, which can be attributed to $Li_xPF_yO_z$[66]; 3) ~137.8 eV, which can be attributed to the $LiPF_6$ salt (~138 eV in the reference sample used in this study) in the electrolyte. The amounts of degradation products were found to grow with cycling. For the pristine coated electrode, the spectrum shows a single peak at 134.3 eV (Figure 2-15c), which can be attributed to Li_3PO_4 as reported previously.[12] In addition to Li_3PO_4, the spectrum of the discharged coated electrode after 1

cycle (Figure 2-15d) was fitted with three components similar to those found in the cycled bare electrodes. After 20 cycles, the XPS P 2p signal of the discharged coated electrode can be attributed to a minor component from $LiPF_6$ and a major component from species such as $PF_x(OH)_y$, which is supported by the fact that the binding energy of the P 2p line for the coated electrode after 20 cycles is close to that reported for $OPCl_3$ (135.9 eV[99]). The Li_3PO_4 component was no longer visible, which could be revealed after 10 minutes of sputtering (not shown). This observation suggests that some Li_3PO_4 remains on the surface of $LiCoO_2$ beneath the newly formed species.

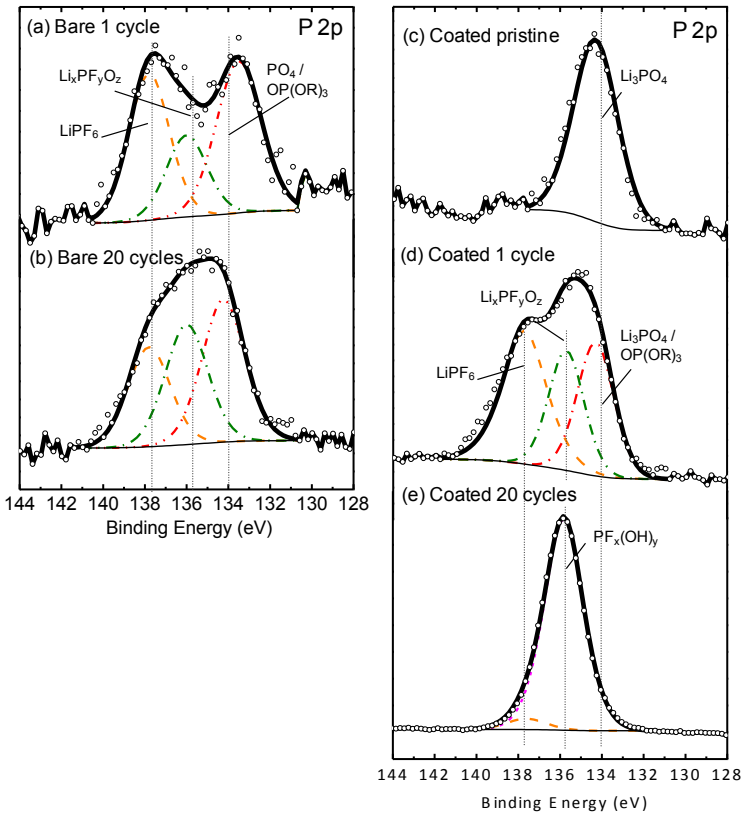

Figure 2-15. XPS spectra of the P 2p photoemission line for bare "$LiCoO_2$" in the condition of (a) after 1 cycle, (b) after 20 cycles and "$AlPO_4$"-coated $LiCoO_2$ in the condition of (c) pristine electrode, (d) after 1 cycle, (e) after 20 cycles.

Al 2s Region. As expected, Al was not detected on the pristine and cycled bare electrodes. The Al 2s photoemission spectra of the pristine and cycled coated electrodes after subtracting the P 2p satellite contribution are shown in Figure 2-16. The Al 2s region of "$AlPO_4$"-coated

$LiCoO_2$ powder (Figure 2-16a) displays a single component at 118.7 eV, which is consistent with that of $LiAlO_2$ or heavily Al-doped $LiCo_{1-y}Al_yO_2$ as reported previously.[12] The Al 2s region of the pristine coated electrode (Figure 2-16b) displays a highly asymmetric line, which was deconvoluted into two components. One component is at 118.6 eV, which is attributed to $LiAlO_2$ or heavily Al-doped $LiCoO_2$ (~118.7 eV).[12] The other component is at ~120.8 eV with the corresponding Al 2p line is at ~75.7 eV (Figure 2-17). The intensity of the high-energy component for the discharged coated electrodes after 1 and 20 cycles increased at the expense of the $LiAlO_2$ component, as shown in Figure 2-16c to Figure 2-16d. After 20 cycles, the $LiAlO_2$ component is no longer visible and only the high-energy component at 120.8 eV is prominent in Figure 2-16d. (The corresponding Al 2p line is at ~75.9 eV as shown in Figure 2-18d.) The high-energy component which appears in the coated pristine electrode, coated electrode after 1 cycle and the entire peak in the coated electrode after 20 cycles indicates that a fraction of the Al (pristine electrode and electrode after 1 cycle) and the entire Al (electrode after 20 cycles) is present in a highly ionic bonding environment.

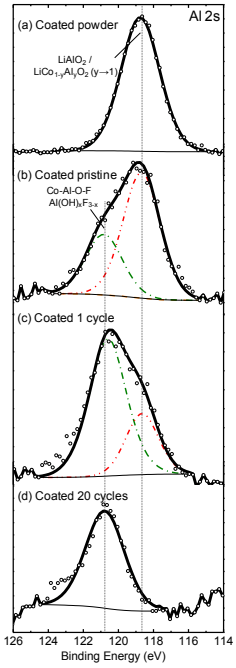

Figure 2-16. XPS spectra of the Al 2s photoemission line for "$AlPO_4$"-coated $LiCoO_2$ in the condition of (a) powder sample, (b) pristine electrode, (c) after 1 cycle, (d) after 20 cycles.

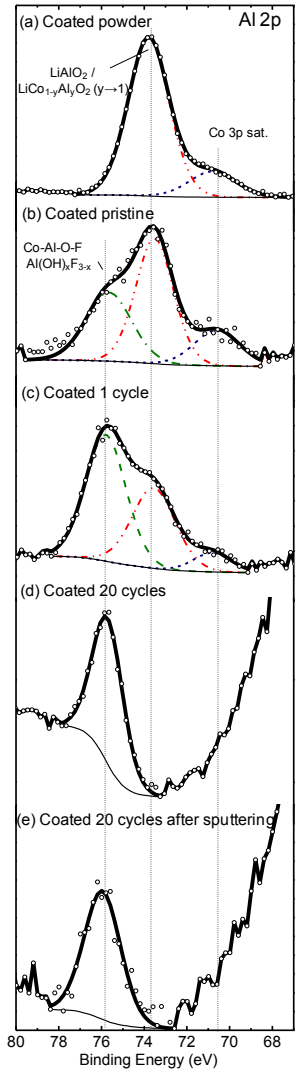

Figure 2-17. XPS spectra of the Al 2p photoemission line for "$AlPO_4$"-coated $LiCoO_2$ in the condition of (a) powder sample, (b) pristine electrode, (c) after 1 cycle, (d) after 20 cycles and (e) 20 cycles after 20 minutes of sputtering.

Furthermore, such high binding energies for that Al 2s and 2p lines cannot be attributed to a pure form of aluminum oxides or hydroxides with Al 2s binding energy in the range of 117.0-119.0 eV.[12] However, such high binding energies for Al 2s and Al 2p were observed for various Al-containing fluorides, oxyfluorides and hydroxyfluorides. For example, Al 2s line of AlF_3 is at ~121.6 eV (reference material in this study); Al 2s and Al 2p lines for K_3AlF_6[100]

are at 120.6 and 75.8 eV; Al 2p line of Al-containing oxyfluoride (Al-O-F) [96] is ~75.8 eV and the Al 2p line of $Al(OH)_xF_{3-x}$ [98] is ~76.0 eV. Accordingly, the Al high binding energy component can be due to surface species in the form of mixed-metal fluorides and/or oxyfluorides and/or hydroxyfluorides. It should be noted that the formation of Al-containing fluorides and/or oxyfluorides and/or hydroxyfluorides in the pristine coated electrode is consistent with results published by Edström et al.[89], in which the authors observed a small impurity of LiF on fresh laminates (with no previous contact with the electrolyte). The authors suggested that the observed LiF was formed as a consequence of a dehydrofluorination reaction in PVDF binder, generating HF, which then reacts with the active material or Li_2CO_3 to form LiF. It is interesting to note that the entire Al in the discharged coated electrode after 20 cycles was found in the form of mixed-metal fluorides and/or oxyfluorides. It is worth noting that the low-energy component of $Li(Al,Co)O_2$ was not revealed after 20 minutes of sputtering (Figure 2-17e, Figure 2-18) indicating that the $LiCo_{1-y}Al_yO_2$ was totally consumed during cycling.

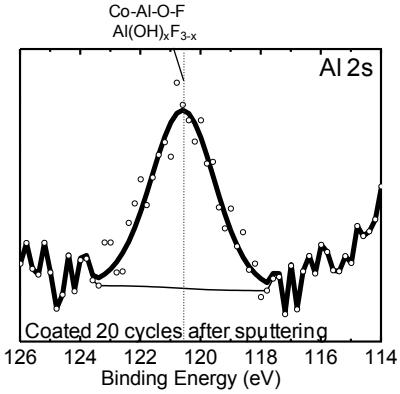

Figure 2-18. XPS spectra of the Al 2s photoemission line for "$AlPO_4$"-coated $LiCoO_2$ in the condition of 20 cycles after 20 minutes sputtering.

Surface Chemical Compositions. The surface chemical compositions of pristine and discharged electrodes after 1 and 20 cycles for bare and coated $LiCoO_2$ are listed in Table 3-2. First, the most noticeable changes in the surface chemistry of the cycled bare electrodes are the surface atomic concentrations of Li and F in the LiF and $Li_xPF_yO_z$ components, which were found to considerably increase during cycling.

Table 2-2. Binding energies (eV) and atomic percentages (%) of the elements Li, C, O, F, P, and Co from the XPS spectra of bare and "$AlPO_4$"-coated $LiCoO_2$ electrodes before and after cycling for 1 cycle and 20 cycles.

		Bare electrode		Bare 1 cycle		Bare 20 cycles	
Peak	Assignments	BE(eV)	Atom%	BE(eV)	Atom%	BE(eV)	Atom%
Li 1s	$LiCoO_2$ (~54.3 eV)	54.4	2.1	54	2.8	54.0	2.3
	LiOH (55 eV) / Li_2CO_3 (55.5 eV) / LiF (56 eV) / $Li_xPF_yO_z$ / $LiPF_6$ (56.8~57 eV)	56.3	3.1	56.5	7.8	56.6	12.7
C 1s	Carbon Black (284.6 eV) / Hydrocarbon (285.0 eV) Shake-up satellite (~290.5 eV)	284.6 / 290.5	49.2	284.6 / 290.5	37.7	284.6 / 290.5	26.4
	C-O (~286.1 eV) CH_2-CF_2(PVDF) (~286.4eV)	286.2	9.0	286.2	7.2	286.3	9.2
	O-C-O / C=O (~287.6 eV)	287.6	2.6	287.6	2.8	287.6	2.5
	O-C=O (~289 eV)	288.9	1.7	288.9	1.5	288.9	2.4
	Li_2CO_3 (~290.3 eV) CF_2 (PVDF) (~290.9 eV)	290.8	4.7	290.7	4.1	290.7	4.0
	CF_3 (~293.5 eV)	293.3	0.7	293.3	0.7	292.7	1.0
O 1s	Lattice oxygen in $LiCoO_2$ (~529.8 eV)	529.8	3.0	529.5	3.6	529.5	3.3
	hydroxide group (ie:LiOH) (~531.0 eV)			531.0	2.2	531.0	0.8
	Surface oxygen in $LiCoO_2$ (~531.7 eV) / O-C=O (ie: $ROCO_2Li$) (~532.0 eV) / Carbonates (ie: Li_2CO_3) (~532.1 eV)	532.1	4.4	532.0	2.1	532.0	3.3
	$OP(OR)_3$ / O-C=O (ie: $ROCO_2Li$) (~533.5 eV)	533.6	2.2	533.5	1.8	533.5	3.1
	$Li_xPF_yO_z$ (~534.6 eV)					534.6	1.2
F 1s	LiF (~685.1 eV)	685.1	0.9	685.5	5.0	685.5	5.3
	$Li_xPF_yO_z$ (~686.6 eV)			686.6	4.8	686.6	7.0
	PVDF(CH_2-CF_2) (~688 eV) / $LiPF_6$ (~688.5 eV)	688.0	15.0	687.9	12.8	688.0	12.7
P 2p	Phosphate (ie: $OP(OR)_3$ ~134 eV)			133.5	0.2	134.2	0.4
	$Li_xPF_yO_z$ (135.5 eV~136 eV)			136.0	0.1	136.0	0.4
	$LiPF_6$ (~137.8 eV)			137.8	0.2	137.8	0.3
Co $2p_{3/2}$	$LiCoO_2$ (~780 eV)	780.1	1.4	779.9	2.5	779.8	2.2
	satellite (+~10 eV)	789.8		788.2		788.2	

		Coated pristine		Coated 1 cycle		Coated 20 cycles	
Peak	Assignments	BE(eV)	Atom%	BE(eV)	Atom%	BE(eV)	Atom%
Li 1s	$LiCoO_2$ (~54.3 eV)	54.5	1.3	54.4	1.4		
	Li_2CO_3 (55.5 eV) / LiF (56 eV) / $Li_xPF_yO_z$ / $LiPF_6$ (56.8~57 eV)	56.2	1.7	57.2	14.3	56.5	7.9
C 1s	Carbon Black (284.6 eV) / Hydrocarbon (285.0 eV) Shake-up satellite (~290.5 eV)	284.6 / 290.5	64.3	284.6 / 290.5	31.6	284.6 / 290.5	0.3
	Hydrocarbon (285.0 eV)					285.2	4.7
	C-O (~286.1 eV) CH_2-CF_2(PVDF) (~286.4eV)	286.3	3.8	286.3	4.5	286.1	1.7
	O-C-O / C=O (~287.6 eV)	287.6	2.1	287.6	2.7	287.6	1.5
	O-C=O (~289 eV)	289.0	1.2	288.9	1.2	289.0	0.5
	Li_2CO_3 (~290.3 eV) CF_2 (PVDF) (~290.9 eV)	290.8	3.4	290.8	2.7	290.3	0.3
	CF_3 (~293.5 eV)	293.3	0.4	293.3	0.5	293.0	0.1
O 1s	Lattice oxygen in $LiCoO_2$ (~529.8 eV)	529.9	2.3	529.8	1.0		
	Li_3PO_4 (~531.6 eV) / Surface oxygen in $LiCoO_2$ (~531.7 eV) / O-C=O (ie: $ROCO_2Li$) (~532.0 eV) / Carbonates ($Li_2CO_{3..}$) (~532.1 eV)	532.0	3.2	532.2	4.5		
	Co-Al-O-F(~532.7 eV) / $PF_x(OH)_y$					532.8	24.3
	$OP(OR)_3$ / O-C=O (ie: $ROCO_2Li$) (~533.5 eV)	533.6	1.4	533.4	3.2		
	$Li_xPF_yO_z$ (~534.6 eV)			534.7	1.7		
F 1s	LiF (~685.1 eV)	685.1	0.6	685.5	3.3		
	Co-Al-O-F (CoF_2 ~686.0 eV)					686.1	12.0
	$Li_xPF_yO_z$ (~686.6 eV)			686.7	10.7		
	PVDF(CH_2-CF_2) (~688 eV) / $LiPF_6$ (~688.5 eV) / $PF_x(OH)_y$	687.9	11.5	688.0	14.0	688.5	27.9
P 2p	Phosphate (ie: $OP(OR)_3$ ~134 eV)	134.3	0.5	134.3	0.4		
	$Li_xPF_yO_z$ (135.5 eV~136 eV) $PF_x(OH)_y$			135.7	0.4	135.8	10.0
	$LiPF_6$ (~137.8 eV)			137.7	0.5	137.6	0.5
Al 2s	$LiAl_yCo_{1-y}O_2$ (y~1)(~118.7 ev)	118.7	0.7	118.7	0.3		
	Co-Al-O-F (K_3AlF_6~120.6 ev) / $Al(OH)_xF_{3-x}$	120.8	0.3	120.6	0.8	120.8	1.0
Co $2p_{3/2}$	$LiCoO_2$ (~780 eV)	780.3	0.8	780.5	0.6		
	satellite (+~10 eV)	790.1		788.6			
	Co-Al-O-F (CoF_2 ~783.7 eV)					783.1	7.4
	satellite (+~6 eV)					788.3	

The surface concentration of F bound in LiF increased from 0.9 (pristine) to 5.0 (after 1 cycle) and 5.3 at.% (after 20 cycles) while that of F bound in $Li_xPF_yO_z$ increased from 0 (pristine) to 4.8 (after 1 cycle) and 7.0 at.% (after 20 cycles). The surface layers of LiF and $Li_xPF_yO_z$, which were presumably formed from the degradation of the electrolyte and side reactions between the electrolyte and Li_xCoO_2, is relatively thin as the surface concentration of the carbon black component is reduced by only about 50% relative to pristine bare electrode. Second, in contrast to the cycled bare electrode, which mainly had surface buildups of LiF and $Li_xPF_yO_z$ during cycling, considerable amounts of Co-containing and Al-containing oxyfluorides (F/Co ratios close to 1.7) were detected on the cycled coated electrodes. A very small amount (barely detectable) Co-containing oxyfluoride species was detected on the cycled bare electrodes. The surface concentrations of Co bound to oxygen atoms in pristine bare and coated electrodes were 1.4 at.% and 0.8 at.%, respectively. The surface concentrations of Co for bare electrodes did not change much during cycling (2.5 at.% after 1 cycle and 2.2 at.% after 20 cycles). In contrast, the surface concentration of Co in the pristine coated electrode of 0.8 at.% remained relatively the same after 1 cycle (~0.6 at.%) but increased to 7.4 at.% after 20 cycles. Furthermore, the surface chemistry of Co changed from the trivalent state in pristine coated $LiCoO_2$ to a divalent state in a Co-containing fluoride and/or oxyfluoride after 20 cycles. The surface concentration of Al remained relatively unchanged during cycling. However, a significant change in Al chemistry occurred during cycling. Al was present in the trivalent state but with 70 % of Al bound to oxygen and 30 % bound to F for the pristine coated electrode. After one cycle, roughly 27 % of Al was bound to oxygen and 73 % was bound to F while the entire Al was bound to F after 20 cycles. As the carbon black component in the C 1s spectrum and Li_3PO_4 component in the P 2p spectrum are no longer visible for the cycled coated electrode after 20 cycles, a relatively thick layer of metal fluorides and/or oxyfluorides was formed on the particle surface. Third, the surface concentration of P increased from 0.5 at.% (pristine coated electrode) to 1.3 at.% (after 1 cycle) and 10.5 at.% (after 20 cycles). The P 2p spectra of the coated electrode after 20 cycles showed that 95 % of P was present in the pentavalent state in a hydroxyfluoride environment such as $PF_x(OH)_y$ and the remainder (5 %) was due to the $LiPF_6$ in the electrolyte. The $PF_x(OH)_y$ type of species could be promoted in the presence of surface coating materials,

namely $LiAlO_2$ or heavily Al-doped $LiCoO_2$ in this study, which could provide additional hydroxyls to the coated samples. For example, AlO(OH) (Al 2s ~118.9 eV) and/or $Al(OH)_xF_{3-x}$ (Al 2s ~120.8 eV) could exist in the coated pristine electrode. Furthermore, the formation of $PF_x(OH)_y$ (e.g., $PF_3(OH)_2$) may proceed via the following reactions deduced from the previous study[89]: 1) $LiPF_6 \Rightarrow LiF + PF_5$, 2) $PF_5 + H_2O \Rightarrow PF_3O + 2HF$; $PF_3O + H_2O \Rightarrow PF_3(OH)_2$. It should be noted that such reaction paths need to be verified with additional experiments.

2.3.5 Proposed Mechanism of Enhanced Capacity Retention for Coated $LiCoO_2$

Figure 2-19 shows the proposed surface chemical compositional changes of bare and "$AlPO_4$"-coated $LiCoO_2$ during cycling to 4.7 V vs. Li, from which the mechanism of enhanced capacity retention by coating is discussed. We have previously shown that the coating material – "$AlPO_4$" consists of two major phases.[12] One is a 10 nm-thick film of Al-rich $LiCo_{1-y}Al_yO_2$ solid solution. The other is a non-uniform distribution of Li_3PO_4 with thickness up to ~100 nm. In our previous study,[12] we have reported that the amount of carbonate specie (i.e.: Li_2CO_3) is reduced by about 70% for the coated $LiCoO_2$ relative to bare "$LiCoO_2$". Having more surface Li_2CO_3 on $LiCoO_2$ has been reported to lead to higher impedance growth as suggested by previous studies.[101] However, other previous studies have shown that Li_2CO_3 can readily dissolve during electrochemical cycling[61] or upon exposure to the electrolyte that typically contains a trace amount of HF.[82] In this study, we are unable to discuss the effect of having more Li_2CO_3 alone on the electrode impedance growth of bare and coated $LiCoO_2$ during cycling. The presence of the coating layer promotes the formation of Co-containing and Al-containing oxyfluorides, and species such as $PF_x(OH)_y$, as shown in Figure 2-19. These Co and Al-containing oxyfluorides can be formed by reactions between HF in the electrolyte and $LiCoO_2$ or $LiCo_{1-y}Al_yO_2$. Having surface Co in the form of oxyfluoride species in the cycled coated electrodes (Figure 2-3) is in agreement with the increasing acidity in the solid-superacid-model[52,57,58] with the addition of coating materials to the electrolyte. However, this observation is in an apparent disagreement with the HF-scavenge-model reported previously[53,54]. In this study, we propose that once Co-containing and Al-containing

oxyfluorides and species like $PF_x(OH)_y$ were developed on the surface of the cycled coated electrodes, the following processes may take place to reduce further electrode impedance growth and enhance capacity retention relative to bare electrodes during extensive cycling. First, they can lower the Co dissolution from the cycled coated electrodes and deposition of Co-containing species on the negative electrode during subsequent cycling, where deposition of Co species is shown to increase electrode impedance.[66] Second, further degradation of $LiPF_6$ on active Li_xCoO_2 particles can be reduced relative to the bare electrode during subsequent cycling. As the molar volume of CoF_2 is two times greater than that of LiF, and a large fraction of coated $LiCoO_2$ particle surface is covered by $PF_x(OH)_y$ like species developed on the cycled coated electrodes, and Li_3PO_4 present in the original coating layer, none of active particle surface in the cycled coated electrodes is exposed to the electrolyte in comparison to a relatively large fraction of active particle surfaces in the cycled bare electrodes. This argument is different from the removal of insulating species such as Li_2CO_3 and LiOH by HF proposed in the solid-superacid model.[52,57,58] Third, oxygen loss from bulk and structural damage of active particles can be reduced by the thick surface layer as synchrotron X-ray diffraction data have revealed no noticeable changes for cycled coated electrodes but selective broadening of discharged bare electrode after 20 cycles (Figure 2-4). The key hypothesis in the proposed mechanism is that coating materials can promote the formation of oxyfluorides and species like $PF_x(OH)_y$ during initial charge and discharge processes, which is essential to reduce the growth of highly resistant films upon subsequent cycling. If the hypothesis were true, one can improve the cycling performance of $LiCoO_2$ to high voltages by mixing $LiCoO_2$ with coating materials such as Al_2O_3, where similar surface compositional changes on the cycled electrodes to cycled "$AlPO_4$"-coated electrodes may occur.

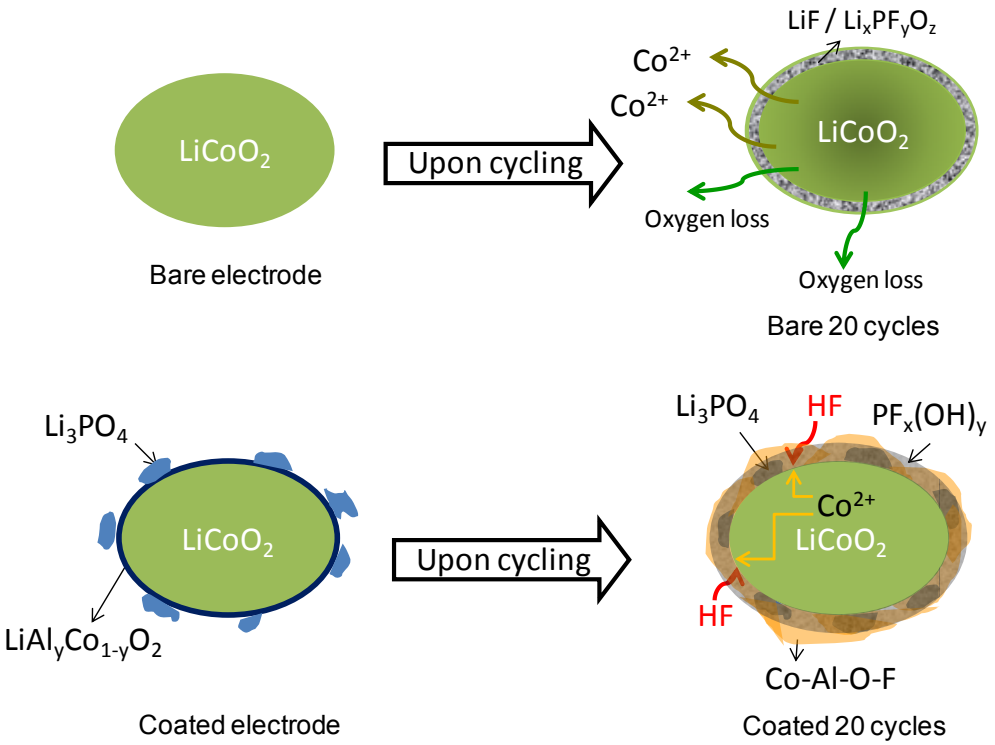

Figure 2-19. Proposed working mechanism of "$AlPO_4$"-coated $LiCoO_2$. Al substituted solid-solution layer react with HF and trap dissolved Co ion from the bulk. The coating materials reduce further Co dissolution as well as surface reactions between active particles and electrolyte by forming "Co-Al-O-F" type of thin film on the surface. In contrast, the bare "$LiCoO_2$" particles are exposed to and react with the electrolyte, continuously to form highly resistant decomposition product of electrolyte, and then isolate the active particle. Co dissolution and oxygen loss also lead to structural instabilities such as formation of the stacking fault.

Test of Proposed Mechanism. In order to verify the hypothesis, we mixed 5 wt.% **γ**-Al_2O_3 nanoparticles with a commercial $LiCoO_2$ (Alfa Aesar, 99.5% metals basis; the X-ray powder diffraction pattern is shown in Figure 2-1; the surface chemistry characterization of **γ**-Al_2O_3 by XPS is shown in Figure 2-20.) and investigated the effects of Al_2O_3 addition on the capacity retention upon cycling to 4.7 V vs. Li. Figure 2-21 show the galvanostatic voltage profiles of a commercial bare $LiCoO_2$ electrode and an electrode consisting of the commercial $LiCoO_2$ mixed with 5 wt.% **γ**-Al_2O_3 nanoparticles (<50 nm, Sigma-Aldrich),

respectively. These test conditions included a C/5 rate (bare: 0.24 mA/cm^2, mixed: 0.25 mA/cm^2) and cycling between voltage limits of 2.5 V and 4.7 V vs. Li for 40 cycles. It is remarkably to note that the cell with a mixture of commercial $LiCoO_2$ and Al_2O_3 exhibits better capacity retention and smaller polarization upon cycling relative to commercial bare $LiCoO_2$. Below we compare the changes in the surface compositions of cycled Li_xCoO_2 electrode with and without Al_2O_3 with those of bare and coated electrodes discussed above.

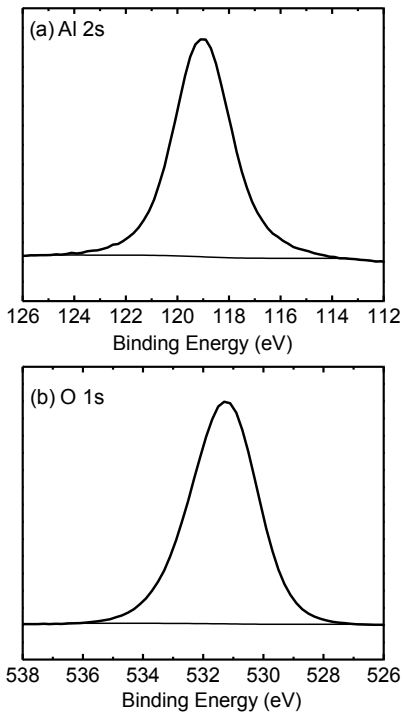

Figure 2-20. XPS spectra of the (a) Al 2s and (b) O 1s photoemission line for the γ-Al_2O_3 nanopowder used in the testing experiment for the proposed mechanism. XPS analysis of the γ-Al_2O_3 nanopowder reveals a surface region composition, which consists of 3.9% C, 61.0% O, and 35.1% Al. After accounting for oxygen bound to carbon, the ratio of O to Al is estimated to be close to 1.6~1.7 indicating that the surface composition of the γ-Al_2O_3 nanopowder is better described as $Al_2O_{(3-x)}(OH)_{2x}$. In addition, the binding energies of the Al 2p and O 1s lines of 74.1 and 531.2 eV, respectively, are close to those reported for Al_2O_3 and AlOOH (Bose, O., et al., *Fresenius J. Anal. Chem.* **358**, 175-179, (1997))

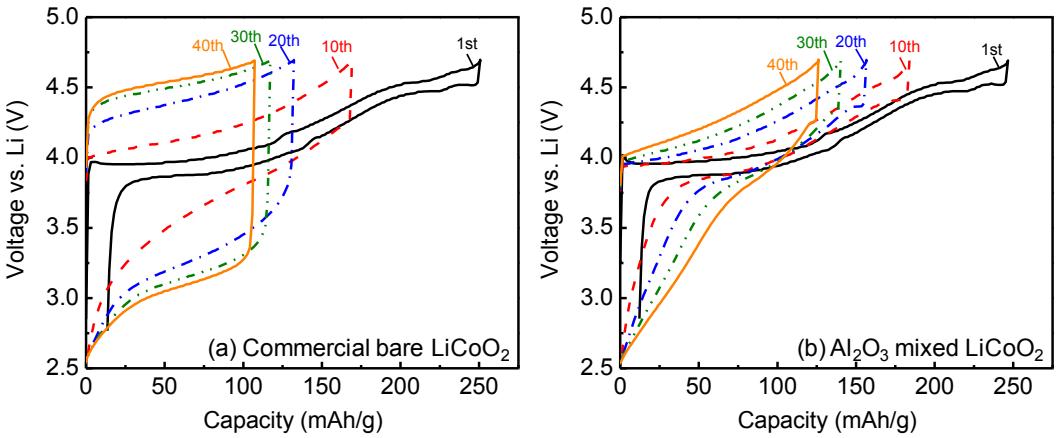

Figure 2-21. Voltage profiles of (a) commercial bare $LiCoO_2$ and (b) commercial bare $LiCoO_2$ mixed with 5 wt.% Al_2O_3 during cycling between 2.5 and 4.7 V at a C/5 rate for 40 cycles.

The surface chemical compositions of the commercial bare $LiCoO_2$ electrode and the mixed electrode of $LiCoO_2$ and Al_2O_3 before and after cycling were analyzed by XPS. The Co 2p and Al 2s spectra are shown in Figure 2-22. Co 2p spectra in Figure 2-22a show that the surface of the mixed electrode after 40 cycles exhibits only one component corresponding to Co-containing fluorides and/or oxyfluorides (~3.4 at.%) while the cycled commercial bare $LiCoO_2$ electrode shows that some surface Co ions are bound to fluorine (~2.0 at.%) and others are bound to oxygen in $LiCoO_2$ (~0.7 at.%). These Co-containing fluoride and/or oxyfluoride species on the cycled commercial and mixed electrodes can be removed by sputtering for 3 and 6 minutes, respectively. A higher amount of Co-containing fluoride and/or oxyfluoride species was detected on the commercial bare electrodes after 40 cycles relative to the bare electrodes after 20 cycles. This difference may be attributed to the facts that the cycling conditions are not exactly identical, and the commercial $LiCoO_2$ is less lithium over-stoichiometric than bare "$LiCoO_2$", as evidenced by observed phase transitions in the voltage profile in Figure 2-21a. In addition, the Al 2s spectrum of the cycled mixed electrode after shifts to higher binding energy relative to the pristine electrode shown in Figure 2-21b. The peak at 121.4 eV can be attributed to aluminum ions in fluorides based on the binding energy of AlF_3 (~121.6 eV). It should be noted that the binding energy for the Al 2s of pristine mixed

electrode (~120.7 eV) was found ~1.7 eV higher than that of γ-Al_2O_3 powder (~119.0 eV). This peak is likely due to aluminum ions in fluorine and oxygen environment, which can result from a chemical interaction between Al in γ-Al_2O_3 powder and the fluorine in PVDF as discussed previously. These observations suggest that not only coated $LiCoO_2$ but also adding Al_2O_3 in the $LiCoO_2$ electrode leads to increased surface coverage of Co- and Al-containing fluoride and/or oxyfluoride species during cycling, which can prevent further Co dissolution and side reactions between the electrolyte and the active material and reduce impedance growth during cycling to high voltages. The detailed mechanism on how the fluoride and/or oxyfluoride species stabilizes active materials and affect the electrode impedance characteristics during cycling is not understood, which will be examined in future studies.

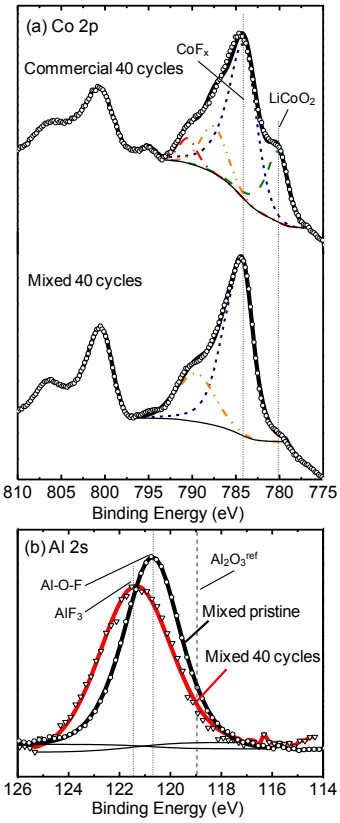

Figure 2-22. XPS spectra of (a) Co 2p and (b) Al 2s for cycled commercial bare $LiCoO_2$ and commercial bare $LiCoO_2$ mixed with 5 wt.% Al_2O_3 in the discharged state after 40 cycles.

2.4 Conclusions

SEM and XPS studies have shown that the surface morphological and chemistry changes of cycled bare and coated electrodes are considerably different. A very thin surface layer that predominately consists of LiF and $Li_xPF_yO_z$ grows during cycling of the bare electrode and partially covers the surfaces of active particles. In contrast, a thick surface layer that primarily include Co- and Al- containing fluorides and/or oxyfluorides and $PF_x(OH)_y$ like species, which completely covers the surfaces of Li_xCoO_2. It is hypothesized that Al-containing oxides on the surfaces of coated $LiCoO_2$ particles promote the formation of Co-Al-O-F species on the particle surfaces. It is proposed that these surface species serve to protect active particles from further side reactions with the electrolyte and possibly prevent bulk oxygen loss as suggested by synchrotron X-ray diffraction data, and reduce impedance growth relative to cycled bare electrodes during cycling to high voltages. This hypothesis is further supported by an experiment, which shows that addition of Al_2O_3 powder to $LiCoO_2$ leads to enhanced stability and reduced electrode impedance growth upon cycling, where similar electrode surface chemistry changes during cycling have been found to cycled "$AlPO_4$"-coated electrodes.

Chapter 3. Quantifying the Intrinsic Activity of Oxygen Reduction Reaction in Li^+-Containing Nonaqueous Media

Reproduced in part with permission from (1) Yi-Chun Lu, Hubert A. Gasteiger, Ethan Crumlin, Robert McGuire, and Yang Shao-Horn, Electrocatalytic Activity Studies of Select Metal Surfaces and Implications in Li-Air Batteries, **J. Electrochem. Soc.** 2010, 157, A1016-A1025, Copyright 2010 The Electrochemical Society; (2) Yi-Chun Lu, Hubert A. Gasteiger, and Yang Shao-Horn, Method Development to Evaluate the Oxygen Reduction Activity of High-Surface-Area Catalysts for Li-Air Batteries, **Electrochem. Solid State Lett.** 2010, 14, A70-A74, Copyright 2011 The Electrochemical Society.

3.1 Introduction

Rechargeable Li-air (or Li-O_2) batteries have the potential to provide specific energy three or four times that of conventional Li-ion batteries.[102] The discharge reaction in the Li-O_2 battery is the reduction of oxygen with lithium ions to form lithium (per)oxide: (1) $2Li + O_2 \leftrightarrow Li_2O_2$ at 2.96 V_{Li}[25,102]; (2) $4Li + O_2 \leftrightarrow 2Li_2O$ at 2.91 V_{Li}[25,102] (V_{Li} refers to the potential measured vs. metallic lithium in the same electrolyte). During charge, these oxides need to be decomposed electrochemically to regenerate lithium and oxygen. There are a number of challenges that need to be overcome in order to make rechargeable Li-air batteries practical, which include poor cycle life,[31,32,36] low round-trip efficiency[31], and rate capability.[27,35] The reaction kinetics of oxygen reduction reaction (ORR) and oxygen evolution reaction (OER) are strongly related to these critical challenges.

Testing carbon-containing composite air electrodes in the Li-O_2 batteries has been applied to study Li-O_2 reactions. However, this approach alone may not be successful in quantifying the intrinsic reaction kinetics nor differentiating catalytic activity of different electrocatalysts. That is, the correlation between the reported discharge capacities/voltages and the intrinsic activities of different catalysts are not necessarily straightforward due to the facts that: (i) oxygen mass transport resistances are likely to

affect cell voltage and are known to impact electrode capacity due to the blocking effect of insoluble lithium (per)oxide formed during discharge inside the air electrode pores;[27,29] (ii) the catalyst surfaces may be partially blocked by lithium (per)oxide discharge products;[27] (iii) the activity of the electrode can be influenced greatly by the ORR activity of carbon, as its mass fraction in these electrodes is large (60 to 75 wt.% carbon[31,39,103]). Therefore, we have developed a rotating disk electrode (RDE) technique to enable quantitative determination of the catalytic activity of various electrode materials in the absence of the above-described constraints.

In this chapter, we report a method to quantify the reaction kinetics of the surface of glassy carbon (GC) as well as high-surface-area Vulcan carbon (VC) dispersed as a thin-film layer (~1 to ~5 μm) on the GC RDE without interference from undefined oxygen mass transport resistances,[104] analogous to that developed for ORR activity measurements in aqueous electrolytes.[105,106]

3.2 Experimental Session

All experiments in this chapter were conducted in 1 M $LiClO_4$ in PC:DME (1:2 v/v) electrolyte, prepared from lithium perchlorate, propylene carbonate (PC), and 1,2-dimethoxyethane (DME) from Sigma-Aldrich (all <50 ppm H_2O) at room temperature. It should be noted that PC has been reported to be react with superoxide ions.[36,107] However, PC solvent or co-solvent has been used in most Li-air studies to date[23,27,28,31,35,39,108-111] due to its low volatility, its high solubility for lithium salts (i.e., $LiPF_6$ and $LiClO_4$), and its consequently high conductivity.

Rotating Disk Electrode Measurements. A three-electrode cell for RDE measurements containing 20 ml of the electrolyte was assembled in a dry argon filled glove box to prevent moisture, oxygen, or nitrogen contamination, as shown in Figure 3-1. The gas lines to supply dry oxygen and argon were purged for 20 minutes before each experiment. The counter electrode was assembled by embedding Li foil into a nickel foam (INCOFOAM^{TM}) support (≈0.5 cm^2) with an attached nickel wire (Alfa Aesar, 99.995%), which was sealed

into a ground glass plug. The lithium-nickel foam assembly was wrapped in Celgard 2350 battery separator material to prevent convective oxygen transport to the Li metal. The Ag/Ag^+ reference electrode (non-aqueous Ag/Ag^+ electrode, BASi, USA) consisted of a Ag wire immersed into 0.1 M tetrabutylammonium hexafluorophosphate ($TBAPF_6$) (Sigma-Aldrich) and 0.01 M $AgNO_3$ (BASi, USA) in PC:DME (1:2 v/v) solution and was connected to the main compartment by a Vycor frit. All potentials in this chapter, however, are referenced to the Li/Li^+ potential, V_{Li}, obtained by calibration of the reference electrode against a fresh lithium wire prior to the experiments (0 V vs. Li/Li^+ corresponding to -3.53 ± 0.02 V vs. Ag/Ag^+). The working electrodes were polished with 0.05 µm alumina powder, rinsed in de-ionized water, dried in a vacuum oven, and then embedded into a Teflon® RDE-holder (Pine, USA).

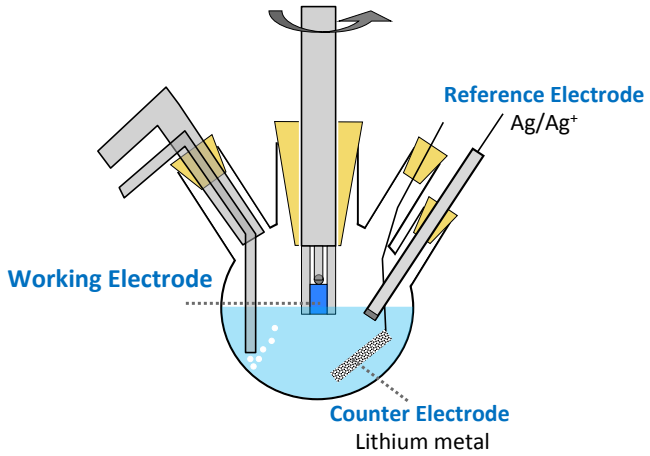

Figure 3-1. Schematic representation of experimental apparatus for nonaqueous RDE measurements.

Two types of working electrode including plain GC electrode disk and high-surface-area thin film electrode were prepared as following. GC disks (0.196 cm^2 disks; Pine, USA) were polished to a 0.05 µm mirror-finish before each experiment. Thin films of pure Vulcan XC-72 (Premetek, USA) were prepared by drop-casting catalyst inks with a Nafion®/carbon weight ratio of 0.5/1 onto a glassy carbon disk, yielding carbon loadings ranging from 0.2 to 0.02 mg_{carbon}/cm^2_{disk}. The carbon inks were composed of Vulcan,

lithiated Nafion® (LITHion™ dispersion, Ion-Power, USA), and 20% 2-propanol (Sigma-Aldrich) in de-ionized water. All working electrodes were subsequently dried in air for 24 hours before testing. The working electrode was attached to a rotating shaft and assembled into the cell by means of a plug with a ball-bearing seal. Once removed from the glove box, the cell was immediately purged with dry argon at sufficiently high flow rates (≈0.1 slpm) to prevent the back-diffusion of air through the ball-bearing seal. The current density is referenced to the geometric disk electrode area (0.196 cm^2) unless specified otherwise.

The working electrode was immersed into the Ar or O_2-purged electrolyte for 30 minutes prior to each cyclic voltammetry (CV) experiment. In pure Ar-saturated electrolyte, steady-state cyclic voltammograms (CVs) were recorded between 2.0 V_{Li} and 4.4 V_{Li} at a voltage sweep rate of 5 or 20 mV/s for capacitive control measurements. For ORR measurements with the plain GC electrodes, pure or Ar-diluted oxygen was bubbled through the cell at ambient pressure and stead-state CVs were recorded at various rotating speeds (100 to 900 rpm). For ORR measurements with the high-surface-area thin film electrodes, the 1st scan CV is defined as follows: after steady-state CVs were obtained in Ar, the cell was purged with O_2 for 20 minutes, and then the potential was scanned from 3.5 V_{Li} to the low voltage limit, followed by a voltage scan to the upper potential limit of 4.4 V_{Li} and then back to 3.5 V_{Li}. The IR-correction to remove ohmic losses was performed by considering a total cell resistance of ~60 Ω measured by AC impedance. The capacitive-corrected ORR currents were obtained by subtracting the current measured under Ar from that found in pure oxygen under identical scan rates, rotation speeds, and carbon loadings. Kinetic currents, i_k, were obtained by correcting the net ORR currents, i_{ORR}, for a known value of the O_2 diffusion-limited current, i_d, using the Levich equation for a first order reaction ($i_k = i_d \times i_{ORR} / [i_d - i_{ORR}]$).

3.3 Results and Discussion

3.3.1 ORR on Well-Defined GC Electrodes

Figure 3-2a shows the steady-state CV of a GC electrode for 1M $LiClO_4$ in PC:DME (1:2 v/v) both in the absence (argon purged) and presence of oxygen (oxygen purged) at a rotation rate of 100 rpm (blue solid line) and a scan rate of 5 mV/s. As expected, no significant anodic or cathodic current was observed in the background CV in Ar, which suggests that the electrolyte used in this system is relatively stable from 2.0 V_{Li} to 4.4 V_{Li}. In 100% O_2, the onset of the reduction current on GC occurs below ≈2.8 V_{Li}, which was found to be unchanged with (1M $LiClO_4$ in PC:DME having 1:2 v/v) and without PC (1M $LiClO_4$ in DME) in the electrolyte.

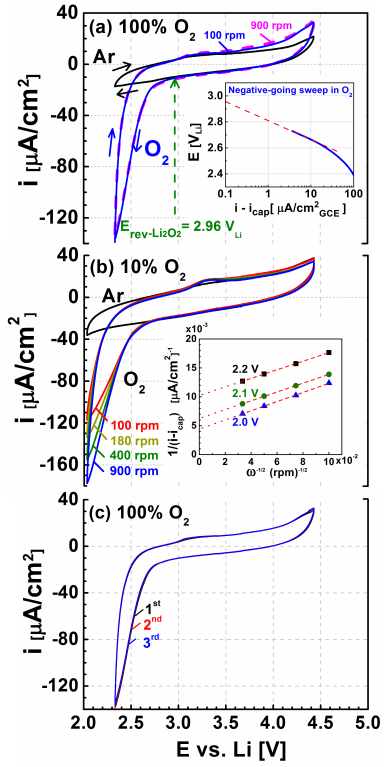

Figure 3-2. (a) CVs of a GC electrode in 1M $LiClO_4$ PC:DME (1:2 v/v) at 5 mV/s saturated with either Ar at 100 rpm (black line) or O_2 at both 100 rpm (blue solid-line) or 900 rpm (pink dotted line). The inset shows the net ORR current density for the negative-going sweep;

which was obtained by up-shifting the reduction current in O_2 by 0.9 $\mu A/cm^2$ so that the net current density for the ORR after the capacitive correction (i.e., $i-i_{cap}$) is zero at the equilibrium potential of 2.96 V_{Li}; the red dashed line is a guide-to-the-eye in order to estimate the potential at lower current densities. (b) CVs of a GC electrode in 1M $LiClO_4$ PC:DME (1:2 v/v) in Ar and 10 % O_2 at 20 mV/s collected at 100, 180, 400 and 900 rpm. Inset: Levich-Koutecky plot of the capacitive-corrected net ORR currents ($i-i_{cap}$) at 2.2, 2.1 and 2.0 V_{Li} with slopes of 77 ± 3 $cm^2 \cdot rpm^{0.5}/mA$ (corresponding to 8.1 ± 0.3 $cm^2 \cdot s^{0.5}/mA$). (c) Reproducibility of subsequent voltammetric scans illustrated by the 1st (black line), 2nd (red line), and 3rd (blue line) scan.

We show the observed reduction current in Figure 3-2a is indeed due to reactions with dissolved oxygen in the electrolyte by examining the rotation-rate-dependence of reduction current with 100% (Figure 3-2a) and 10% O_2 (Figure 3-2b). Unfortunately, no difference in the ORR current was observed between 100 rpm (blue solid line) and 900 rpm (pink dotted line) in 100% O_2 (Figure 3-2a). This could be explained if the diffusion-limited current density (i_d) were much larger than the kinetic current density (i_k). The former can be obtained from the Levich equation:

$$i_d = 0.62nFD_O^{2/3}\nu^{-1/6}C_O^*\omega^{1/2} \tag{3-1}$$

where n is the overall number of transferred electrons, F is the Faraday constant (96485 As/mol), D_O is the diffusion coefficient of O_2, ω is the rotation rate (in radian/s), ν is the kinematic viscosity of the solution, and C_o^* is the saturated O_2 concentration in the electrolyte. Since D_O, ν, and C_o^* in PC:DME (1:2 v/v) with 1 M $LiClO_4$ are not expected to be significantly different from that with 1 M $LiPF_6$, their values can be estimated from those provided by Read et al.[28] The estimated oxygen solubility for PC:DME (1:2 v/v) is C_o^* $=4.46 \cdot 10^{-6}$ mol/cm^3 with a dynamic viscosity of $\eta=1.98 \cdot 10^{-2}$ Pa/s equivalent to $\nu=0.02$ cm^2/s for an average density of 0.98 g/cm^3. In 1M $LiPF_6$ PC:DME (1:1 v/v), D_O and η were given as $7.0 \cdot 10^{-6}$ cm^2/s and $2.59 \cdot 10^{-2}$ Pa/s,[28] which by means of the Stokes-Einstein relation yields an estimated value of $D_O=9.2 \cdot 10^{-6}$ cm^2/s for PC:DME (1:2 v/v). Using these values in Eq. 3-1, one can estimate the values of the minimum diffusion-limited current densities (i.e., that for

the one-electron reduction to LiO_2), equating to ≈750 μA/cm^2 and ≈2200 μA/cm^2 at 100 and 900 rpm, respectively. These diffusion-limited current densities are more than 5-fold larger than the measured current densities (≈140 μA/cm^2, see Figure 3-2a), which explains the lack of rotation rate dependence and indicates that the ORR current density is essentially kinetically limited with 100% O_2. We then performed RDE measurements with 10% O_2 balanced with Ar (Figure 3-2b), which lowers the diffusion limiting current density by a factor of 10 compared to 100% O_2 due to the 10-fold lower oxygen concentration following Henry's Law. A clear rotation-rate dependence of the ORR currents below ≈2.3 V_{Li} was noted in the steady-state CVs on GC with 10% O_2/Ar in Figure 3-2b, which confirmed that the observed reduction currents involved dissolved oxygen. Interestingly, the reduction current for 10% O_2 had a lower onset potential of ≈2.6 V_{Li} compared to ≈2.8 V_{Li} for 100% O_2, the cause of which will be discussed in detail later. A linear relationship (the Levich-Koutecky analysis) was found between RDE current and $\omega^{-1/2}$ at constant-potential lines (Figure 3-2b inset), with a slope of with a value of 8.1 ± 0.3 cm^2·s$^{0.5}$/mA. In principle, the slope can be used to determine the number of electrons such as n=1 for LiO_2, n=2 for Li_2O_2, and n=4 for Li_2O transferred in the rate-limiting step using the following relationship:

$$slope = (0.62 \cdot n \cdot F \cdot D_O^{2/3} \cdot \nu^{-1/6} \cdot C_O^*)^{-1} \tag{3-2}$$

provided that precise values of D_O, ν, and C_o^* were available. Unfortunately, the values of D_O, ν, and C_o^* are only reported in a similar electrolyte (i.e., 1M $LiPF_6$ in PC:DME (1:1 v/v)[28]) but are not available for 1M $LiClO_4$ in PC:DME (1:2 v/v) used in our study. Therefore, it is not possible to extract the accurate number of electron transfer from RDE data reported here.

3.3.2 Quantifying Intrinsic ORR Activity of GC Electrodes and Implications in Li-O_2 Cells

The net ORR kinetic current density (after capacitive correction) is shown as a function of voltage in the inset of Figure 3-2a. It should be noted that the maximum IR correction is only ≈2 mV (the highest total current is ≈30 μA; the measured resistivity of the system is ≈60 Ω), so that no ohmic potential drop corrections were applied here.

Interestingly, the ORR kinetic current density at 2.7 V_{Li} is ≈4 $\mu A/cm^2_{GCE}$, which is much higher (by 20 times) than the ≈0.2 $\mu A/cm^2_{carbon}$ extracted from currents used in previous studies based on 70 mA/g_{carbon} and a carbon BET (Brunauer-Emmet-Teller) area of ≈40 m^2/g_{carbon}.[31,39,103] This result indicates that the intrinsic activity of carbon itself is high enough to explain the discharge voltage plateaus observed in previous studies on carbon-based electrodes with or without additional catalyst.[21,30,31,39,103,112,113] Therefore, the catalyst-independent discharge voltages (≈2.6 V_{Li})[39] reported for Li-O_2 electrodes with different catalysts mixed with Super S carbon (60 to 75 wt.% carbon[39]), are likely to result from the high activity of carbon.

It should be noted, however, that even though similar discharge voltages were reported for all the different catalysts added to the carbon-based Li-O_2 electrodes in the work by Débart et al.,[39] large differences were observed with regards to capacity and capacity retention. As shown previously,[23] capacity can be reduced significantly with decreasing cathode void volume, which is available for lithium (per)oxide formation. Therefore, for a rigorous comparison, electrodes with different catalysts would have to have identical void volumes, as was done in a recent study on various catalysts for Li-O_2 electrodes.[102] Unfortunately, no information was provided by Débart et al.[39] regarding the morphologies of the different catalysts used (particle size, particle shape, catalyst surface area). It is, therefore, not possible to determine whether differences in cathode void volume may have caused the observed differences in capacity between the differently catalyzed O_2-electrodes. Therefore, as far as ORR activity is concerned, capacity and capacity retention of electrodes with potentially very different electrodes are not meaningful descriptors. It is hypothesized here that the observed differences in capacity retention may be related to differences in lithium (per)oxide decomposition activities of the various catalysts on charge.

Consequently, ORR activity tests solely using carbon-based electrodes are not ideal to examine the *intrinsic* activity of cathode due to the interference from carbon support and/or carbon additives, an artifact avoided by the RDE technique shown in this chapter, which enables a more straightforward evaluation of ORR activity. However, while the specific activity (i.e., the surface area normalized activity) of high-surface area carbons used

in Li-O_2 electrodes should be reasonably similar to that of a GC electrode yet not identical, a quantitative comparison requires further measurements of the ORR activity of high-surface area carbons in an RDE configuration as was developed for fuel cell catalysts,[105] which will be discussed in the later session.

3.3.3 Proposed Soluble and Insoluble ORR Products on GC Electrodes

We here discuss the dissolution of ORR product(s) based on the imbalance between reduction and oxidation columbic charges. Although the onset of an oxidation current at ≈3.6 V_{Li} on GC in the positive-going scan of Figure 3-2a is in agreement with charging curves of Li-O_2 batteries with carbon electrodes which show a charging voltage plateau starting from ≈3.9[21] to ≈4.5 V_{Li},[39] the coulombic charge upon oxidation is only ≈10% of the preceding oxygen reduction charge. As there was no difference between the first negative-going scan of a fresh electrode and all subsequent cycles (Figure 3-2c), the accumulation of surface insoluble ORR products upon cycles can be excluded. Therefore, we believe that a significant fraction of ORR products (e.g., Li_2O_2, Li_2O, or LiO_2) formed below ≈3 V_{Li} dissolves into the electrolyte (20 ml) in our RDE measurements (much less dissolution of ORR products is expected in Li-O_2 cells as the ratio of electrolyte volume to electrode surface area is many orders of magnitude lower), which is reported to have finite Li_2O_2 and Li_2O solubility,[114] particularly with trace amounts of H_2O.[115] The minute solubility required for (partial) dissolution is illustrated by integrating the net reduction current shown in Figure 3-2a and assuming a two-electron reduction formation of Li_2O_2: only 6 nmol of Li_2O_2 are produced per reduction sweep, which, if dissolved into the electrolyte (20 ml), would give a concentration of 0.3 μM; since the total number of cycles in each experiment was on the order of fewer than 30, a solubility of ≈10 μM would support the above hypothesis, assuming a sufficiently fast dissolution rate. Unfortunately, we have no experimental means to quantify a possible solubility of Li_2O_2 at the 10 μM level (46 μg/l), so that we cannot confirm/reject this possibility. At the same time, it is also quite feasible that LiO_2 which may be formed as intermediate could be solubilized by the electrolyte as was suggested by Laoire et al.[116]

To test this hypothesis, we extended the negative potential limit to 2.0 V_{Li} (green dashed line in Figure 3-3a), which increased the amount of ORR products by a factor

of two (assuming Li_2O_2), amounting to 12 nmol per reduction sweep. This led to increased oxidation current/charge in the positive sweep (suggesting an increased amount of ORR products on or near the GC surface available for electro-oxidation), where a new oxidation peak appeared between 3.1 and 3.4 V_{Li} and a slight increase of the oxidation current above ≈3.6 V_{Li} was noted. Comparing oxidation currents with and without rotation provides further evidence for partial dissolution of ORR product(s).

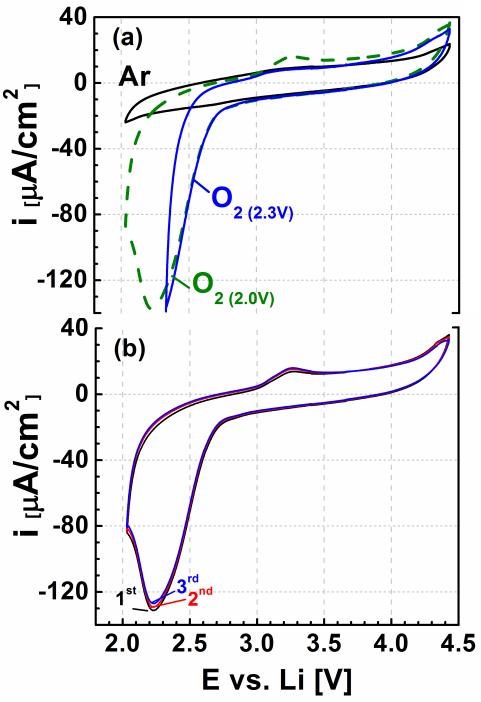

Figure 3-3. CVs of a GC electrode in 1 M $LiClO_4$ PC:DME (1:2 v/v) at 5 mV/s and 100 rpm. (a) 1st voltammetric scans between 2.3 V_{Li} and 4.4 V_{Li} in Ar (black line) and pure O_2 (blue line) as well as with an extended negative potential limit of 2.0 V_{Li} in pure O_2 (green dashed line). (b) Repeat experiment under identical conditions with freshly prepared electrode, showing the 1st (black line), 2nd (red line), and 3rd (blue line) scans, indicating good reproducibility and negligible difference between 1st and 3rd scans (within 10 mV).

Figure 3-4 shows that the oxidation charge in the positive-going scan is increased in stagnant electrolyte (0 rpm) compared to forced convection at 100 rpm (the amounts of electro-oxidation charge are comparable at rotations greater than 100 rpm up to 900 rpm), despite the rotation rate independent ORR charge in the negative-going scan. With

rotation, dissolved ORR species can move away from GC surface into the bulk of the electrolyte leading to the decreased electro-oxidation current. The oxidation peak between 3.1 and 3.4 V_{Li} appears to resemble the small inflection point at ≈3.1 V_{Li} in the initial charging of a Li-O_2 cell with a non-catalyzed carbon cathode which was discharged to 2 V_{Li}.[39,102] It should be noted that the electro-oxidation rate of Li_2O_2 on carbon electrodes is nearly zero below 4 V_{Li},[102,103] so that the anodic peak initiating near 3 V_{Li} is not due to Li_2O_2 oxidation. On the other hand, LiO_2 has only been observed as a bulk phase at ≈15 K[117,118] and was never observed at room temperature, therefore, the reversible potential for LiO_2 decomposition is not available. However, interestingly, Laoire et al.[116] have suggested a reversible potential of 3.0 V_{Li} for LiO_2 decomposition, unfortunately, no references to the thermodynamic database underlying its derivation were provided. Since this oxidation peak is very close to the reversible potential for Li_2O_2 or potentially LiO_2 decomposition, it is postulated that the oxidation of soluble and/or adsorbed LiO_2-like species, is responsible for the anodic peak between 3.1 – 3.4 V_{Li}, considering that the formation and oxidation of $O_2^{\bullet -}$ radicals in organic electrolytes in the absence of metal ions was shown to be a highly reversible reaction.[119]

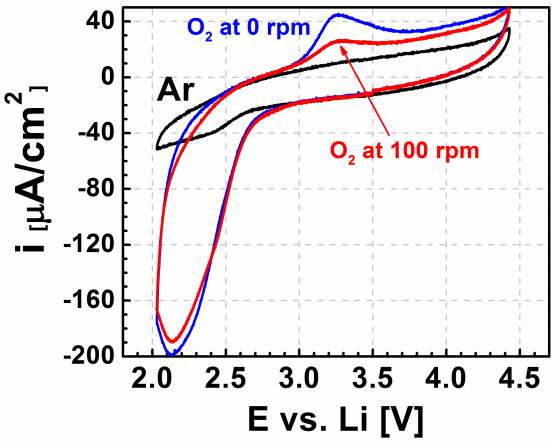

Figure 3-4. CVs of a GC electrode in 1M $LiClO_4$ PC:DME (1:2 v/v) in Ar (black line) or O_2 saturated electrolyte at 20 mV/s and 0 rpm (blue line) or 100 rpm (red line).

The formation of insoluble (surface-adsorbed and/or solid) ORR products is apparent from the decrease of the reduction current with decreasing voltage at 100 rpm (green

dashed line in Figure 3-3a) leading to electrode poisoning below 2.3 V_{Li}. Unlike previous studies with a positive voltage limit of 3 V_{Li} by Aurbach and co-workers[107] that show ORR products blocking further O_2 reduction on the electrode surface for Au and Ag electrodes upon subsequent cycles, ORR discharge products were removed from the electrode surface with a positive potential limit of 4.4 V_{Li} chosen in our RDE experiments, leading to steady-state CVs with negligible difference in ORR activity between the first and all subsequent cycles. This is shown for the repeat experiment with a freshly prepared glassy carbon electrode in Figure 3-3b, demonstrating that the 1st, 2nd, and 3rd voltammetric scans are within ≈10 mV in for this and all other experiments reported in this work. In these previous studies, ORR currents were only observed in the first negative-going scan on a fresh electrode, which is related to the fact that their positive voltage scan limit of 3 V_{Li} is too low for lithium (per)oxide decomposition;[107] the same was also observed in galvanostatic experiments with lithium ions[120] as well as in other studies using zinc and other metal cations.[119] This good agreement with subsequent voltammetric scans thus enables the unambiguous quantification of the catalytic activity of a clean electrode surface in the potential region near the onset of the ORR current, where self-poisoning by discharge product in voltammetric scans between the selected potential window (2.0 V_{Li} – 4.4 V_{Li}) can be excluded.

3.3.4 Reaction Order of PO_2 on the ORR Kinetics on Well-Defined GC Electrodes

Since practical Li-air batteries would be operated with air instead of oxygen, it is critical to understand the effect of oxygen partial pressure, p_{O2}, on cathode performance and its ORR reaction kinetics. For example, for an air utilization of ≈50% (ratio of air consumed in the reaction over that of air supplied to the battery), typically used in proton exchange membrane fuel cells (PEMFCs),[33] the concentration of oxygen at the exiting air stream would only be 10%. While mathematical modeling of oxygen mass transport in electrolyte-flooded pores of a Li-O_2 electrodes shows that lowering p_{O2} reduces its discharge capacity,[29] supported by the experimentally observed, reduced capacity when using electrolytes with low oxygen solubility or when using low oxygen partial pressures,[28] we report, for the first time, the reaction order with respect to oxygen partial pressure obtained for the ORR kinetics in aprotic organic electrolytes.

The significant negative-shift of the cell voltage with decreasing p_{O2} from 100% to 1% O_2 in Figure 3-5 can be deconvoluted into kinetic and thermodynamic effects by a simple kinetic analysis assuming Tafel kinetics for the ORR current density, i_{ORR} (commonly used to model the ORR kinetics in PEMFCs[121]):

$$i_{ORR} \propto p_{O_2}^{\gamma} \cdot e^{\frac{\alpha \cdot F}{R \cdot T} \cdot \eta_{ORR(p_{O_2})}} \propto p_{O_2}^{\gamma} \cdot e^{\frac{\alpha \cdot F}{R \cdot T} \cdot \left(E_{rev(p_{O_2})} - E_{cathode}\right)} \tag{3-3}$$

where γ is the reaction order with respect to p_{O2}, α is the cathodic transfer coefficient, T and F are temperature and the Faraday constant, and η_{ORR} is the overpotential of the cathode reaction. It should be noted that the so-called Tafel-slope is defined as $2.303 \cdot RT/(\alpha \cdot F)$. Conducting the analysis under the assumption that Li_2O_2 is the major discharge product on non-catalyzed carbon (consistent with ex-situ Raman[21] and also assumed in recent density functional theory calculations[26]), η_{ORR} is the difference between the p_{O2}-dependent reversible potential for Li_2O_2 formation, $E_{rev(p_{O2})}$, (amounting to $2.303 \cdot RT/(2 \cdot F) \approx 30$ mV per decade of p_{O2} described by the Nernst equation) and the actual cathode potential. Therefore, the dependence of ORR current density with oxygen partial pressure at a *constant electrode potential* contains both the purely kinetic term γ and a thermodynamic term due to the p_{O2} dependence of the equilibrium potential, $E_{rev(p_{O2})}$:

$$\left(\frac{\partial log(i_{ORR})}{\partial log(p_{O_2})} \right)_{E_{cathode}} = \gamma + \frac{\alpha}{2} \tag{3-4}$$

On the other hand, if evaluated *at a constant overpotential*, the decrease of the i_{ORR} with p_{O2} only depends on the kinetic parameter γ, which provides insights into the ORR reaction mechanism:

$$\left(\frac{\partial log(i_{ORR})}{\partial log(p_{O_2})} \right)_{\eta_{ORR}} = \gamma \tag{3-5}$$

As shown in the inset of Figure 3-5, γ is determined to be 0.63±0.02 at overpotentials of 540 and 590 mV. These values are quite similar to what was reported for PEMFC cathodes ($\gamma \approx 0.5$[121]), and the significant dependence of p_{O2} on the ORR current suggests that the initial

adsorption of oxygen is a rate-determining step on GC electrodes, which is probably related to the relatively weak carbon-oxygen bond strength (≈1.8 eV for O adsorption on graphite (001)[122]).

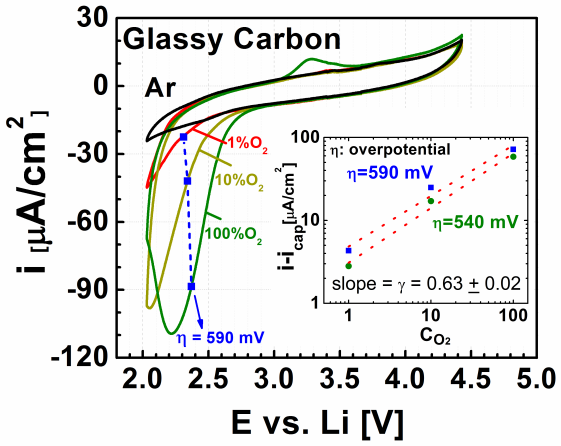

Figure 3-5. CVs of a GC electrode in 1M $LiClO_4$ PC:DME (1:2 v/v) in Ar and 1, 10, and 100% O_2 at 5 mV/s and 900 rpm. The inset shows the ORR reaction order, γ, with respect to oxygen concentration obtained at constant overpotentials, η, (i.e., η=540 and 590 mV based on $E_{rev\text{-}Li2O2}$ = 2.96 V_{Li}. for 100% O_2).

3.3.5 ORR on High-Surface-Area Vulcan Carbon Thin Film Electrodes

RDE polarization curves with different carbon loadings were used to determine the oxygen diffusion limiting current density at a rotation rate of 100 rpm. Figure 3-6a shows the first CV scan at 100 rpm of a GC RDE and of Vulcan thin-films supported on a GC RDE with loadings ranging from 0.02 to 0.2 mg_{carbon}/cm^2_{disk} in the presence of oxygen. As expected, the onset potential for the ORR shifts positively and the overall current normalized to geometric surface area increases with increasing carbon loading, simply related to the increase of electrochemically active surface area with increasing catalyst loadings. Corresponding capacitance-corrected ORR polarization curves (see experimental section) for the negative-going scans are shown in Figure 3-6b, from which the charge associated with the ORR can be obtained. Assuming an external surface area of 100 m^2/g_{carbon} for Vulcan XC-72

(based on a spherical approximation for primary carbon particles having a diameter of ~30 nm and a carbon bulk density of ~2 g/cm^3),[123] the potentials at which ~1 monolayer (ML) of LiO_2 (~200 $\mu C/cm^2_{LiO2}$)[107] is formed on the carbon surface in the negative-going scans can be estimated (see dots in Figure 3-6b). As the carbon loading increases from 0.02 to 0.1 mg_{carbon}/cm^2_{disk}, the potential corresponding to the buildup of 1 ML of adsorbed LiO_2 shifts to more negative values. The fact that no apparent O_2 diffusion-limited ORR currents are observed for these electrodes, suggests that ORR discharge products accumulate on the carbon surface and poison its ORR activity. This hypothesis is consistent with the presence of a O_2 diffusion-limited current density of ~3.0 mA/cm^2_{disk} below 2.2 V_{Li} for the highest carbon loading of 0.2 mg_{carbon}/cm^2_{disk}, for which the total accumulated ORR charge never reaches the 1 ML equivalent on the carbon surface during the negative-going potential scan down to 2.0 V_{Li} (see Figure 3-6b). The decreasing ORR current densities (upward bending curves) below 2.1 V_{Li} for carbon loadings of $\leq$ 0.1 mg_{carbon}/cm^2_{disk} can be attributed to poisoning of the ORR by the accumulation of adsorbed ORR discharge products.

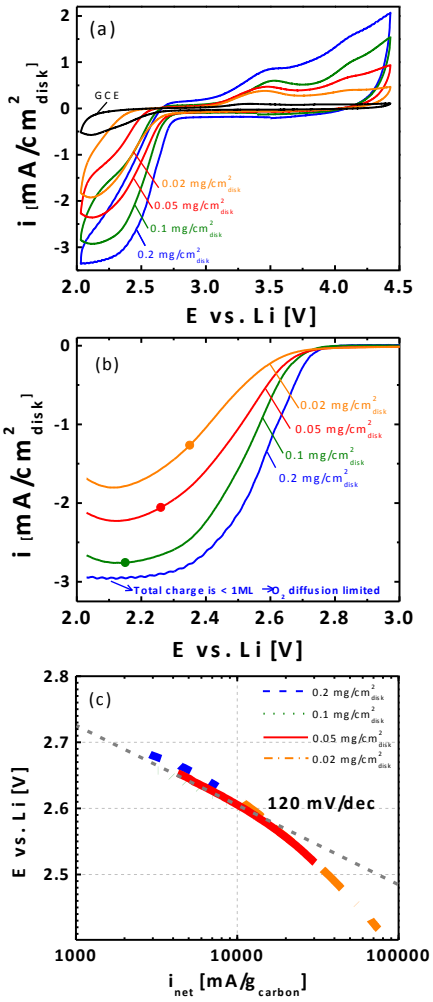

Figure 3-6. (a) 1st CV scan (50 mV/s) at a rotation rate of 100 rpm between 2.0 V_{Li} and 4.4 V_{Li} (see experimental section for definition) on glassy carbon and pure Vulcan carbon electrodes with various loadings (0.02 to 0.2 mg_{carbon}/cm^2_{disk}) in oxygen-saturated PC:DME (1:2 v/v) with 1 M $LiClO_4$. (b) Capacitive-corrected net ORR current densities during the negative-going scan based on the data in Figure 3-6a. The solid-dots indicate the voltage at which the accumulated charge reaches a one-monolayer equivalent of LiO_2 (200 $\mu C/cm^2_{carbon}$) for each carbon loading; for 0.2 mg_{carbon}/cm^2_{disk}, the total accumulated charge remains less than one monolayer down to the negative potential limit. (c) Capacitance-corrected, O_2 mass transport-corrected ($i_d = 3$ mA/cm^2_{disk}), and IR-corrected Tafel plots for the ORR on pure Vulcan carbon electrodes, whereby the maximum IR-correction is ~12 mV.

The net ORR current densities of electrodes of various carbon loadings were used to extract the intrinsic mass activity of Vulcan carbon. To this purpose, the capacitance-corrected data shown in Figure 3-6b were corrected both for ohmic losses (IR-correction) and for O_2 mass-transport resistances (i.e., using the Levich Equation with the observed limiting current of $i_d \sim 3.0$ mA/cm$^2_{disk}$). These kinetic ORR current densities were then normalized by the respective carbon loadings, yielding the *carbon mass activities* (in units of mA/g_{carbon}), which is plotted vs. potential shown in Figure 3-6c. It should be noted that the data in Figure 3-6c are based only on ORR activity data for which the net ORR current density is two times larger than the corresponding capacitive current density and smaller than 1/3 of the observed oxygen diffusion limiting current density of 3 mA/cm$^2_{disk}$, so that errors in the capacitive and O_2 mass-transport corrections are negligible. If one were to assume that the thin-film RDE method enables the extraction of the intrinsic carbon mass activity, one would expect that the ORR activities for all electrodes would superimpose, exactly as is observed in Figure 3-6c. Furthermore, for carbon mass activities below ~15000 mA/g_{carbon}, the ORR activity can be described by a single Tafel slope of ~120 mV/decade (see dashed line in Figure 3-6c). Above ~15000 mA/g_{carbon}, obtained only for electrodes with 0.02 and 0.05 mg$_{carbon}$/cm^2 loadings (orange dash-dot and red solid lines in Figure 3-6c), the ORR activity strongly deviates from the 120 mV/decade Tafel line, which can be explained by the fact that the poisoning by ORR discharge product(s) initiates at increasingly more positive potentials as the carbon loading is decreased (see Figure 3-6b). The observed apparent Tafel slope of ~120 mV/decade in the region below ~15000 mA/g_{carbon} suggests a one-electron rate-limiting ORR having a Tafel-slope of $2.303 \cdot RT/(n \cdot \alpha \cdot F)$, where R is the gas constant, T is the temperature, n is the number of electron transfer in the rate-limiting step (equal to 1 for ~120 mV/decade), F is the Faraday constant (96485 As/mol), and the transfer coefficient α is 0.5).[124] This one-electron reduction of oxygen is consistent with the formation of lithium superoxide ($Li^+ + O_2 + e^- \rightarrow LiO_2$) as proposed by in our previous work[125] and Laoire et al.[116]

Since the poisoning of the ORR activity by discharge products becomes negligible with increasing carbon loadings as shown in Figure 3-6, the Levich-Koutecky analysis can in principle be applied to determine the number of electrons, *n*, exchanged in the rate-limiting step (e.g., *n*=1 for LiO_2). Here, the slope of the Levich-Koutecky plot of the

inverse of the ORR net current, i_{net}, versus the inverse of the square root of the rotation rate is described in Eq. (3-2).[124] Unfortunately, the precise values of the physical properties of the electrolyte (i.e., D_O, C_o^*, ν) that are required to determine the value of *n,* are not known. These electrolyte properties, however, can be estimated, if the lithium cations are replaced by tetrabutyl ammonium (TBA) cations, under the reasonable assumption that the nature of the cation does not significantly affect D_O, C_o^*, and ν, as long as the total salt concentration is unchanged. Since the ORR in the presence of TBA^+ cations in aprotic organic electrolytes exhibits a quasi reversible oxygen/superoxide-radical redox behavior ($O_2 + e^- \leftrightarrow O_2^-$)[119] with *n* = 1, the Levich-Koutecky slope (which is proportional to $D_O^{-2/3} \cdot v^{1/6} \cdot (C_O^*)^{-1}$) with TBA^+ should provide a good estimate of the electrolyte properties when TBA^+ is replaced by Li^+.

This approach is illustrated in Figure 3-7. Figure 3-7a shows that well-defined O_2 diffusion-limited currents are obtained for the ORR on a glassy carbon electrode in PC:DME (1:2 v/v) with 1 M $TBAClO_4$, analogous to that reported for acetonitrile with 1 M $TBAPF_6$.[116] The fact that the O_2 diffusion-limited current density in PC:DME (1:2 v/v) with 1 M $TABClO_4$ at 100 rpm ($i_d \sim 3$ mA/cm$^2_{disk}$) is identical with that observed in Figure 3-6a for 1 M $LiClO_4$-based electrolyte, already suggests that the initial ORR discharge product in the presence of lithium ions is LiO_2. The capacitance-corrected Levich-Koutecky plots in the presence of TBA^+ obtained from Figure 3-7a at 2.0 V_{Li} (*Slope*=2.0 $cm^2_{disk} \cdot rpm^{0.5}/mA$) and 1.4 V_{Li} (*Slope*=2.5 $cm^2_{disk} \cdot rpm^{0.5}/mA$) are shown in Figure 3-7c.

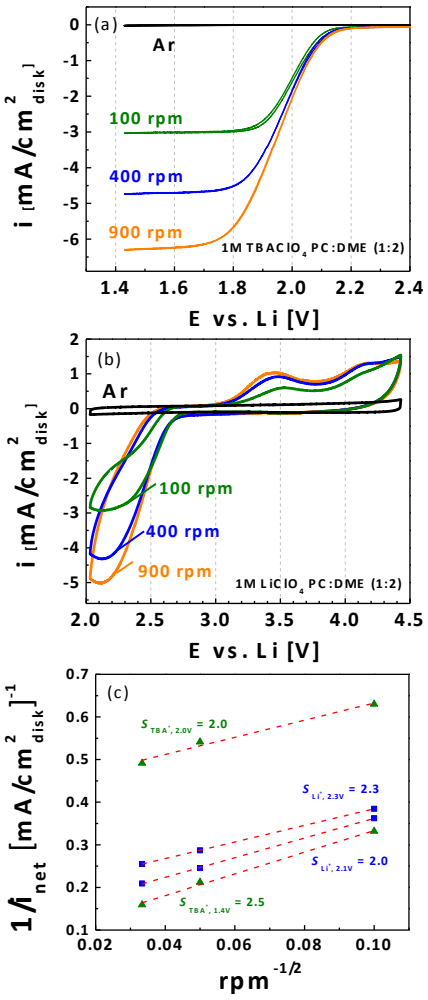

Figure 3-7. (a) Steady-state CVs of a glassy carbon RDE in PC:DME (1:2 v/v) with 1 M $TBAClO_4$ at 20 mV/s between 2.0 V_{Li} and 4.4 V_{Li} in Ar (900 rpm) and in pure O_2 (100, 400 and 900 rpm. (b) 1st voltammetric scans (see experimental section) of a Vulcan carbon electrode (0.1 mg_{carbon}/cm^2_{disk}) in PC:DME (1:2 v/v) with 1 M $LiClO_4$ at 50 mV/s between 2.0 V_{Li} and 4.4 V_{Li} in pure O_2 (100, 400 and 900 rpm); the Ar steady-state CV at 900 rpm is also shown for reference. (c) Levich-Koutecky-plots from the ORR data shown in Figure 3-7a and b, whereby the values of the slopes, *S*, indicated in the figure are given in units of $cm^2_{disk} \cdot rpm^{0.5} / mA$.

Figure 3-7b shows the CVs of a Vulcan carbon electrode (0.1 mg_{carbon}/cm^2_{disk}) in PC:DME (1:2 v/v) with 1M $LiClO_4$ at various rotation rates, with a clearly pronounced

rotation rate dependence of the ORR currents. Similarly the capacitance-corrected Levich-Koutecky slopes were obtained between 2.3 and 2.1 V_{Li} (see Figure 3-7c), which has both significant rotation rate dependence of the ORR currents ($\leq 2.3\ V_{Li}$) and negligible poisoning by ORR discharge products ($\geq 2.1\ V_{Li}$; see Figure 3-6b). The Levich-Koutecky slopes in the presence of Li^+ (2.3 and 2.0 $cm_{disk}^2 \cdot rpm^{0.5}/mA$ at 2.3 and 2.1 V_{Li}, respectively) are comparable to those in the presence of TBA^+ within experimental errors (see Figure 3-7c), which supports that the ORR in the presence of Li^+ on Vulcan carbon first proceeds by an one-electron reduction to LiO_2, consistent with the ORR mechanism proposed by Laoire et al.[116] It should be noted that the slopes obtained for Li^+ and TBA^+ cations in 100% O_2 (~2.3 $cm_{disk}^2 \cdot rpm^{0.5}/mA$) agree nicely with our previous work (translating 8.1 $cm_{disk}^2 \cdot s^{-0.5}/mA$ to 25 $cm_{disk}^2 \cdot rpm^{0.5}/mA$ in 10% O_2).[125] However, the observed slopes in Figure 3-7c are roughly 5 times smaller than the value estimated based on published electrolyte properties (13.3 $cm_{disk}^2 \cdot rpm^{0.5}/mA$),[125] which can be attributed to typically large errors in O_2 diffusivity and solubility measurements. This highlights the need for more careful evaluation of electrolyte properties for Li-air battery development. The approach presented here can provide insights into the initial ORR product formed for this self-poisoning reaction, but this approach can of course not resolve the subsequent reactions which might occur outside the analyzed potential window. It is believed that initially formed LiO_2 will further react to form Li_2O_2 ($2LiO_2 \rightarrow Li_2O_2 + O_2$)[116,125] and/or get further reduced to Li_2O_2 at lower potentials ($LiO_2 + e^- + Li^+ \rightarrow Li_2O_2$),[26] which both would equate to an overall $2e^-$ reduction reaction.

3.4 Conclusions

In this study, we show a new method for the quantitative evaluation of the electrocatalytic activity of well-defined GC electrodes as well as high-surface-area carbon in a RDE configuration. The intrinsic ORR activity of GC and Vulcan carbon is sufficiently high to dominate all the discharge voltages reported previously for composite air electrodes of different catalysts having carbon greater than 60 wt.% as an additive. In addition, the reaction order of the nonaqueous Li^+-ORR with respect to oxygen partial pressure, p_{O2}, was found to

be 0.5, which suggests that the initial adsorption of oxygen is a rate-determining step on GC electrodes. Tafel analysis shows that the ORR activity of Vulcan carbon can be described by a Tafel slope of 120 mV/dec and Levich-Koutecky analysis of the RDE data on Vulcan carbon suggests that the ORR in the presence of Li^+ on Vulcan carbon first proceeds by an one-electron reduction to LiO_2 in the rate-limiting step.

Chapter 4. Catalyst Effects and Reaction Mechanism of the Discharge Reaction of Rechargeable Li-Air Batteries in Li^+-Containing Nonaqueous Media

4.1 Introduction

Research efforts toward better understanding of the nonaqueous oxygen reduction reaction (ORR) mechanism and the design principles of highly active ORR catalysts are critical to improve the discharge performance, which directly affects the deliverable gravimetric energy and power of Li-air (or Li-O_2) batteries.[38,126] Nanometer-scale catalysts based on precious metals (Au: 2.8 V_{Li} at 100 mA/g_{carbon} or 0.04 mA/cm^2_{geo};[127] Pd: 2.87 V_{Li} at 0.12 mA/cm^2_{geo} [128]) are reported to have higher discharge voltages than metal oxides (e.g., α-MnO_2: 2.75 V_{Li} at 70 mA/g_{carbon};[31] Fe_2O_3: 2.6 V_{Li} at 70 mA/g_{carbon}[39]). However, it is difficult to correlate reported geometric and carbon-mass-normalized currents of these catalysts to the intrinsic ORR activity such as true-surface-area-normalized ORR currents and ORR catalyst-mass-normalized currents of these catalysts. This is because the catalyst particle sizes and catalyst loadings can be significantly different among these studies. Further complication arises from the fact that carbonate-based electrolytes used in these studies[31,39,127,128] are unstable against ORR reaction intermediates such as superoxide O_2^- to form species such as

lithium carbonate instead of lithium peroxide or oxides expected for Li^+-ORR.[36,110,129-133] The parasitic reactions between the ORR intermediates and the carbonate-based solvents can greatly influence the discharge voltages, and hamper the development of highly active catalysts for Li^+-ORR in stable electrolytes necessary for rechargeable Li-O_2 batteries.

In this chapter, we report systematic ORR studies on four different polycrystalline metal catalysts including palladium (Pd), platinum (Pt), ruthenium (Ru), gold (Au) as well as glassy carbon (GC) via rotating-disk electrode (RDE) in 0.1 M $LiClO_4$ 1,2-dimethoxyethane (DME). Previous studies on ORR electrocatalysis in aqueous electrolytes have shown that the activity can be governed by the oxygen binding to the catalyst surface.[134-137] The activity trend for Li^+-ORR on these surfaces is correlated with oxygen adsorption energy, which can serve as predictive tools for the design and screening of highly active catalysts. In addition, the activity trend obtained on these polycrystalline surfaces translates well to that of high-surface-area thin film catalysts supported on GC electrode via RDE, and early discharge voltages of the Li-O_2 cells. Furthermore, we use pure Vulcan carbon and 40 wt% Au-nanoparticles supported on Vulcan carbon as examples to demonstrate the catalyst effects on the discharge rate capability of Li-O_2 cells. Lastly, we discuss the nonaqueous Li^+-ORR mechanism, the rate-determining steps, and compare the nonaqueous Li^+-ORR to the ORR in aqueous media.

4.2 Experimental Session

All the RDE measurements reported in this chapter were collected from a three-electrode cell with O_2-saturated 0.1 M $LiClO_4$ DME (Novelyte USA, <20 ppm) in a water-free glovebox (H_2O < 0.1 ppm, O_2 < 1 %). All electrodes were vacuum-dried at 75 ^oC for at least 12 hours followed by direct transfer from the vacuum oven to the water-free glovebox without exposure to the ambient. DME was used as the solvent to study the ORR as it is reasonably stable during ORR unlike carbonate-based solvents.[107,126,129,138] The stability of DME in the operation window in this study (3.1 – 2.0 V_{Li}) is within the stable window of DME reported by Aurbach et al. (4.5 – 1.0 V_{Li} on Pt).[139]

ORR Stability and the Poisoning Effect of DME. To investigate the stability and reversibility of $O_2/O_2^{-\bullet}$ on Pt in DME, we examine the oxygen reduction reaction on the Pt disk in 0.5 M $TBAClO_4$ DME as shown in Figure 4-1. Two observations are noted. First, no reaction current was observed in the range of 3.1 – 2.0 V_{Li} (the potential window used in this study), which suggests that there was no significant reaction associated with Pt, oxygen and DME solvent. Second, the $O_2/O_2^{-\bullet}$ redox couple is stable and reversible even at a slow scan rate of 5 mV/s. This suggests that O_2^- radical is reasonably stable on Pt electrode in DME.

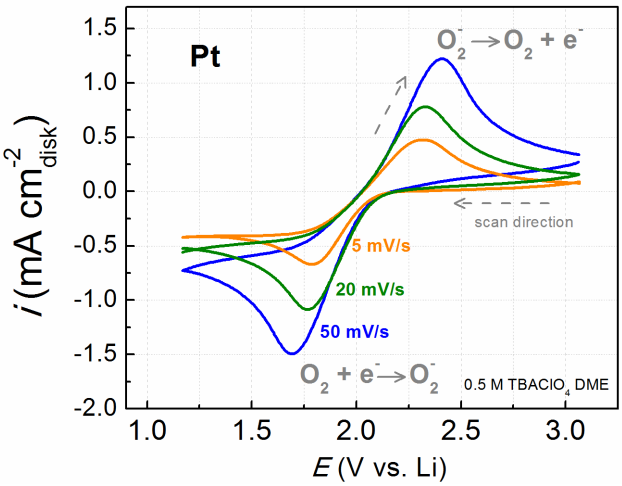

Figure 4-1. Steady-state cyclic voltammogram of ORR on a Pt disk in O_2-saturated 0.5 M $TBAClO_4$ DME at 5, 20, and 50 mV/s and 0 rpm.

In addition, to investigate the poisoning effect of DME molecules on the catalyst surfaces (e.g., Pt disk), we examine the ORR activity of the Pt disk in 0.1 M KOH in the presence of 100 mM DME. The results are compared to that in the pure 0.1 M KOH. Figure 4-2 shows the polarization curves of ORR on a Pt disk in 0.1 M KOH (orange) and 100 mM DME - 0.1 M KOH (blue) at 10 mV/s and 900 rpm. We note that the Pt ORR activity is barely influenced by the presence of DME. The difference is 7 mV at 1 mA/cm^2_{disk}.

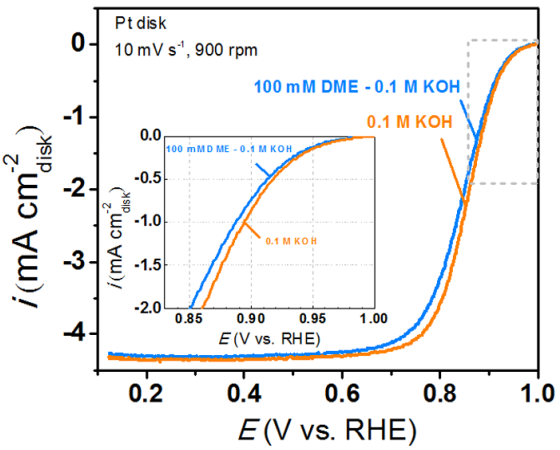

Figure 4-2. Polarization curves (positive-going scans) of ORR on a Pt disk in 0.1 M KOH (orange) and 100 mM DME - 0.1 M KOH (blue) at 10 mV/s and 900 rpm.

RDE Measurements of Bulk Disks. Three-electrode cells were prepared by following procedures. Polycrystalline palladium (Pd), platinum (Pt), gold (Au), glassy carbon (GC) (0.196 cm^2 disks; Pine, USA), and ruthenium (Ru) (0.196 cm^2 disks; Princeton Scientific Corp., USA) surfaces were polished to a 0.05 μm mirror-finish, ultra-sonicated in de-ionized water (18.2 MΩ·cm, Millipore) for 10 min and followed by vacuum-drying at 75°C for 12 hours before each experiment. All electrodes were kept in the vacuum oven and directly transferred to a water-free glovebox (H_2O < 0.1 ppm, Mbraun, USA) without exposing to the ambient. The three-electrode cell used for RDE measurements consists of a lithium-foil counter electrode, a reference electrode based on a silver wire immersed into 0.1 M $TBAPF_6$ (Sigma-Aldrich) and 0.01 M $AgNO_3$ (BASi) in DME which was calibrated against Li metal in 0.1 M $LiClO_4$ DME (0 $V_{Li} \approx -3.64 \pm 0.01$ V vs. Ag/Ag^+), and a bulk disk as the working electrode. The RDE experiments were performed in the water-free glovebox. The electrolyte was 0.1 M $LiClO_4$ DME (H_2O < 20 ppm Novolyte, USA). The working electrode was immersed into an Ar-purged electrolyte for 15 minutes prior to each cyclic voltammetry (CV) experiment. After steady-state CVs were obtained in Ar (2 - 3.15 V_{Li} at 100 rpm, 20 mV/s), the potential was scanned between 3.15 – 3.0 V_{Li} at 100 rpm, 20 mV/s for 20 cycles followed by 1 cycle between 3.15 – 2.0 V_{Li} at 100 rpm, 20 mV/s (the Ar background scan used for capacity correction). Subsequently, the cell was purged with O_2 for 15 min with potential cycling between 3.0 – 3.15 V_{Li}, and then the potential was scanned from 3.15 V_{Li} to 2.0 V_{Li} at

100 rpm, 20 mV/s. The IR-correction was performed by considering the total cell resistance of 3.1 KΩ measured by EIS.

RDE Measurements of High-Surface-Area Thin Film Catalysts. Catalyst thin films and three-electrode cells were prepared by following procedures. Glassy carbon disks were polished to a 0.05 μm mirror-finish, ultra-sonicated in de-ionized water (18.2 MΩ·cm, Millipore) for 10 min and followed by vacuum-drying at 75°C for 3 hours before thin film casting. Thin films of Vulcan carbon (VC), 40 wt.% Au/Vulcan (Au/C), 40 wt.% Ru/Vulcan (Ru/C), 40 wt.% Pt/Vulcan (Pt/C), 40 wt.% Pd/Vulcan (Pd/C) (Premetek, USA) were prepared by drop-casting catalyst inks with a Nafion®/carbon weight ratio of 0.5/1 onto a GC disk, yielding carbon loadings of 0.05 mg_{carbon}/cm^2_{disk}. The catalyst inks were composed of the high-surface-area catalysts, lithiated Nafion® (LITHion™ dispersion, Ion-Power, USA), and 20% 2 propanol (Sigma-Aldrich) in de-ionized water. The catalyst thin-films were subsequently dried in vacuum at 75°C for 24 hours before testing. All electrodes were kept in the vacuum oven and directly transferred to a water-free glovebox (H_2O < 0.1 ppm, Mbraun, USA) without exposing to the ambient. The description of the three-electrode cell can be found in the previous session (bulk disk). The working electrode was immersed into Ar-purged electrolyte for 15 minutes prior to each CV experiment. After steady-state CVs were obtained in Ar (2 - 3.15 V_{Li} at 900 rpm, 5 mV/s), the potential was scanned between 3.15 – 3.0 V_{Li} at 900 rpm, 5 mV/s for 20 cycles followed by 1 cycle between 3.15 – 2.0 V_{Li} at 900 rpm, 5 mV/s (the Ar background scan used for capacity correction). Subsequently, the cell was purged with O_2 for 15 min with potential cycling between 3.0 – 3.15 V_{Li}, and then the potential was scanned from 3.15 V_{Li} to 2.0 V_{Li} at 900 rpm, 5 mV/s. The capacitive-corrected ORR currents were obtained by subtracting the current measured under Ar from that found in pure O_2 under identical scan rates, and rotation speeds. The IR-correction was performed by considering the total cell resistance of 3.1 KΩ measured by EIS.

CVs of Bulk Electrodes (Pt, Pd, Au) and the High-Surface-Area Catalysts (Pt/C, Pd/C, Au/C) for Electrochemical Surface Area (ESA) Determination. Mirror-polished (0.05 μm mirror-finish) Pt, Pd, and Au disk electrodes and the Nafion-bonded high-surface-area (Pt/C,

Pd/C, Au/C) thin film catalysts on GC electrode (0.05 mg_{carbon}/cm^2_{disk}) were mounted to a rotator and immersed into 0.5 M H_2SO_4 (Fluka). A spiral Pt wire was employed as the counter electrode, and a saturated calomel electrode (SCE, Analytical Sensor, Inc.) was used as the reference electrode. The potential of SCE with respect to the reversible hydrogen electrode (RHE) was calibrated from RDE measurements of hydrogen oxidation. All the potential values reported in this paper for aqueous media refer to that of the RHE (V_{RHE}). After the electrolyte was bubbled with Ar for half an hour, the (Pt & Pt/C), (Pd & Pd/C), and (Au & Au/C) working electrodes were scanned between 0.045 - 1.20 V_{RHE}, 0.36 - 1.35 V_{RHE}, and 0.44 - 1.7 V_{RHE}, respectively, at a sweep rate of 50 mV/s, 0 rpm to reach steady state at room temperature. Finally, steady-state CVs were recorded at 10 mV/s in the same potential ranges.

CO stripping voltammetry of Ru disk and Ru/C.[140,141] Mirror-polished (0.05 μm mirror-finish) Ru disk electrode and Nafion-bonded high-surface-area Ru/C thin film catalysts on GC electrode (0.05 mg_{carbon}/cm^2_{disk}) were mounted to a rotator and immersed into 0.5 M H_2SO_4 (Fluka). After the electrolyte was bubbled with Ar for half an hour, steady-state CV of the Ru working electrodes were obtained between 0.05 – 0.95 V_{RHE}, at a sweep rate of 20 mV/s, 0 rpm. CO was adsorbed by holding the potential at 0.075 V_{RHE} for 3 min in a CO-saturated cell. The electrode was then transferred to an Ar-saturated cell immersed under potential control at 0.075 V_{RHE} followed by potential scan from 0.075 V_{RHE} to 0.95 V_{RHE} at 20 mV/s.

Determination of ESA and the Roughness Factor of the Catalysts. The determination of Pt surface area was done as follows: 1) integrating the net (i.e., with double-layer capacitance subtraction) charge formation of hydrogen adsorption region (negative-going scan from 0.4 V_{RHE} – 0.045 V_{RHE}) and hydrogen desorption region (positive-going scan from 0.045 V_{RHE} – 0.4 V_{RHE}). Double-layer capacitance background was assumed by linear-extension from the double-layer region; 2) Average the net charge from hydrogen adsorption and desorption; 3) the averaged net charge (μC) was then divided by the converting factor for Pt surface,[1] 210 $\mu C/cm^2$, and yield the ESA of Pt. Considering a geometric area of 0.196 cm^2, the roughness factor of the Pt disk was determined to be 3.3. The ESA of Pt/C was determined to be 96 m^2/g_{Pt}.

The determination of Pd surface area was done as follows: 1) integrating the net (i.e., with double-layer capacitance subtraction) charge formation of palladium oxides (negative-going scan from 1.00 V_{RHE} – 0.40 V_{RHE}). Double-layer capacitance background was assumed by linear-extension from the double-layer region; 2) the net charge (μC) was then divided by the reported converting factor (i.e., 400 μC/cm^2 for the potential window being 1.35 V_{RHE})[142] yielding the ESA of Pd. Considering a geometric area of 0.196 cm^2, the roughness factor of the Au disk was determined to be 2.1. The ESA of Pd/C was determined to be 89 m^2/g_{Pd}.

The determination of Au surface area was done as follows: 1) integrating the net (i.e., with double-layer capacitance subtraction) charge formation of AuO or $Au(OH)_2$ (negative-going scan from 1.34 V_{RHE} – 0.92 V_{RHE}). Double-layer capacitance background was assumed by linear-extension from the double-layer region; 2) the net charge (μC) was then divided by the reported converting factor (i.e., 350 μC/cm^2 for the potential window being 1.7 V_{RHE})[143] yielding the ESA of Au. Considering a geometric area of 0.196 cm^2, the roughness factor of the Au disk was determined to be 4.6. The ESA of Au/C was determined to be 27 m^2/g_{Au}.

The determination of Ru surface area was done as follows: 1) integrating the net charge formation of CO adsorption (positive-going scan from 0.075 V_{RHE} – 0.95 V_{RHE}); 2) the net charge (μC) was then divided by the reported converting factor (i.e., 420 μC/cm^2 assuming a 1:1 ratio of CO to each metal site)[141] yielding the ESA of Ru. Considering a geometric area of 0.196 cm^2, the roughness factor of the Au disk was determined to be 4.4. The ESA of Ru/C was determined to be 185 m^2/g_{Ru}.

The determination of GC surface area was done as follows: 1) the specific capacitance of carbon (μF/cm$^2_{carbon}$) in 0.1 M $LiClO_4$ DME was determined to be 10.17 μF/cm$^2_{carbon}$, which was estimated from the capacitance of high-surface-area VC (BET: 222 m^2/g_{carbon}) (0.05 mg_{carbon}/cm^2_{disk}) in 0.1 M $LiClO_4$ DME. 2) the specific capacitance obtained above is used to calculate the true surface area of GC assuming the specific capacitance of VC is similar to that of GC in the same electrolyte.[123] Considering a geometric area of 0.196 cm^2, the roughness factor of the GC disk was determined to be 16.

Li-O_2 Cell Measurements. Li-O_2 cells consisted of a lithium metal anode (15 mm in diameter and ~0.45 mm thickness) and a lithiated Nafion®-bonded air electrode (12.7 mm in diameter) of either VC, Au/C, Ru/C, Pt/C, Pd/C. Air electrodes with a Nafion®/carbon weight ratio of 0.5/1 were prepared by coating ultrasonicated inks composed of catalyst, lithiated Nafion®, and 2-propanol onto the separator (Celgard C480). After air-drying at 20 ^oC for 20 minutes, the air electrodes were subsequently vacuum-dried at 75 ^oC for 3 hours, weighed, vacuum-dried at 75 ^oC for at least 12 hours prior to transferring into a glovebox (H_2O < 0.1 ppm, O_2 < 0.1 ppm, Mbraun, USA). All electrodes were kept in the vacuum oven and directly transferred to the glovebox without exposing to the ambient. All electrodes were soaked in 0.1 M $LiClO_4$ DME for 12 hours in the glovebox prior to use. The carbon loadings of air electrodes were $\approx 0.4\ mg_{carbon}/cm^2_{electrode}$. The average electrode thickness for all electrodes was 20 ± 3 μm. All Li-O_2 single cells were assembled in a glovebox (H_2O < 0.1 ppm, O_2 < 0.1 ppm) with 0.1 M $LiClO_4$ DME as electrolyte and tested at room temperature in the glovebox. Li-O_2 cells were assembled in the following order: 1) placing a lithium foil onto the stainless steel current collector of the cell, 2) adding 50 μl electrolyte, 3) placing two pieces of the separator (Celgard C480, vacuum-dried at 75 ^oC for at least 12 hours, transferred without exposing to the ambient) onto the lithium foil, 4) adding 50 μl electrolyte, 5) placing the air electrode onto the separator, 6) adding 50 μl electrolyte, 7) placing a current collector (316 stainless steel mesh and spring) on top, and, 8) purging the cell with dry O_2 for 10 minutes in a water-free glovebox (H_2O < 0.1 ppm). Li-O_2 cells were discharged galvanostatically (Solartron 1470) at a rate of 100 mA/g_{carbon} with a low voltage limit of 2.0 V_{Li}.

X-ray Powder Diffraction Measurements. X-ray powder diffraction **(**XRD) patterns of pristine and discharged VC and Au/C electrodes were collected using a Rigaku Rotaflex X-ray diffractometer (Tokyo, Japan) with a copper rotating anode (Cu Kα) under the glancing-angle mode with an incident X-ray angle of 5°. Kapton® film sealed glass holders were used to hold discharged electrodes for XRD analysis. The XRD sample preparation of discharged electrodes were all done in the glovebox. A continuous scan rate of 0.3 °/min and 0.24 ^{o}/min from 30 to 70° of 2θ was used for samples discharged at 100 mA/g_{carbon} and 2000 mA/g_{carbon}, respectively.

X-ray Absorption Near Edge Structure Analysis. O and Li K edge X-ray Absorption Near Edge Structure (XANES) spectra were obtained at the Canadian Light Source (CLS) on the spherical grating monochromator (SGM) and the plane grating monochromator (PGM) beamline, respectively. XANES spectra were recorded in the surface sensitive total electron yield (TEY) using specimen current and bulk sensitive fluorescence yield (FY) using a multi-channel plate detector. The probing depth of XANES K edge TEY is less than 10 nm[144] while O K edge FY is on the order of hundreds of nanometers,[145] which is comparable to XRD that capture information from the bulk particles. On the other hand, the probing depth of Li K edge FY XANES is around tens of nanometers,[145] which is more surface sensitive compared to O K edge FY. Discharged VC, Au/C electrodes and six reference samples were examined. Reference powder samples included Li_2O_2 (90% Aldrich), Li_2O (99.5%, Alfa Aesar), LiOH (99.95%, monohydrate, Aldrich), Li_2CO_3 (99%, Alfa Aesar), $LiClO_4$, and lithiated Nafion®. Samples were prepared in an Ar-filled glove-bag before being loaded into the vacuum chamber. The low grating at SGM and medium grating at PGM was used with exits slits at 20 mm and 50 mm, respectively. The flux was $2 \cdot 10^{11}$ photons/s at PGM and $4 \cdot 10^{12}$ photons/s at SGM. The beam spot size was ~ 0.5 mm. The pressure in the characterization chamber was better than $2.8 \cdot 10^{-6}$ Torr. The absolute photon energy at PGM was calibrated by Ni L-edge XANES of Ni mesh. To make the comparison between the samples acceptable all collection was made within one day so energy shift issues were minimized.

4.3 Results and Discussion

4.3.1 Activity Trends of Nonaqueous Li^+-ORR Activity on Well-Defined Bulk Surfaces

Figure 4-3 shows the polarization curves of polycrystalline Pd, Pt, Ru, Au and GC electrodes in Ar-saturated (steady-state) and O_2-saturated (1st scan) 0.1 M $LiClO_4$ DME electrolyte during the negative-going scan normalized by the geometric surface area of the electrode. The capacitive-corrected ORR currents can be calculated by subtracting the current measured under Ar from that found in pure O_2 under identical scan rates, and rotation speeds.

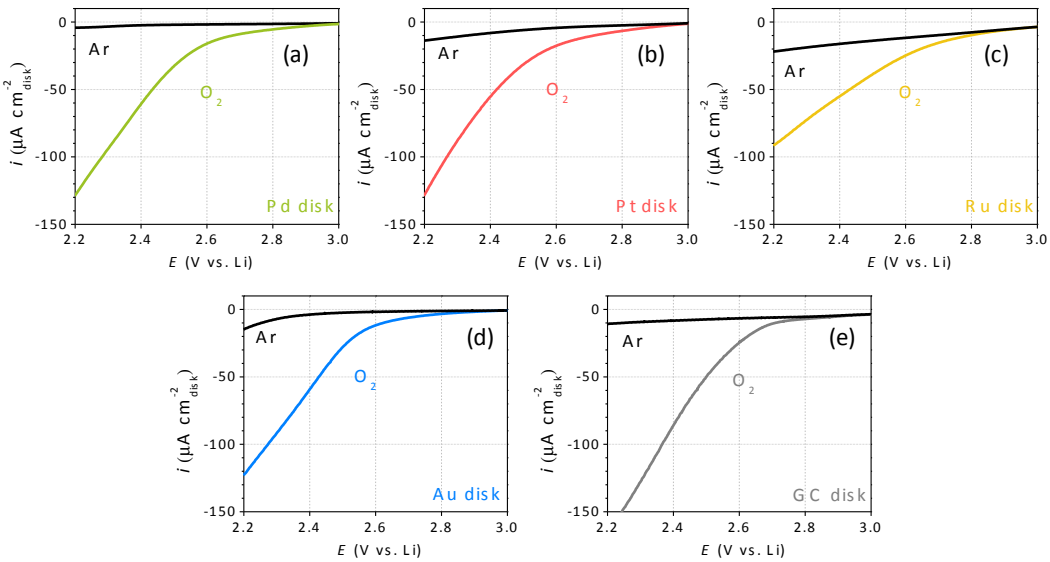

Figure 4-3. Polarization curves in Ar (steady-state) and in O_2 (1st scan) during the negative-going scan of polycrystalline (a) Pd, (b) Pt, (c) Ru, (d) Au, and (e) GC disks in 0.1 M $LiClO_4$ in DME 20 mV/s and100 rpm.

To obtain the intrinsic ORR activity of each catalyst, we normalized the capacitive-corrected ORR currents with respect to the true electrochemical surface area (ESA) of each electrode, which is estimated from electrochemical measurements as described in the experimental session. The real-surface-area-normalized net ORR current densities of the five electrode disks, termed specific activity (is, μA /cm^2_{real}), are shown in Figure 4-4.

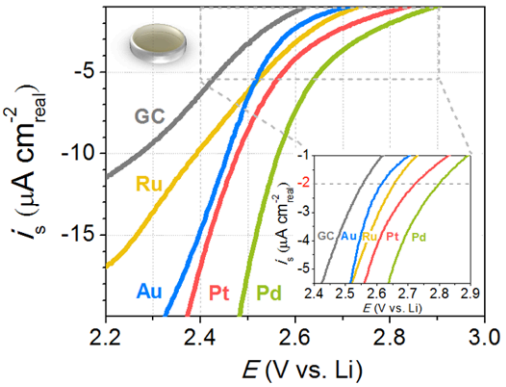

Figure 4-4. Background- and IR-corrected specific ORR polarization curves of polycrystalline Pd, Pt, Ru, Au and GC surfaces in O_2-saturated 0.1 M $LiClO_4$ DME at 100 rpm and 20 mV/s.

The Li^+-ORR activity was found to be Pd > Pt > Ru ≈ Au > GC. As these surfaces exhibited similar Tafel slopes of ~150 mV per decade up to 2 $\mu A/cm^2_{real}$, the dashed line in Figure 4-4 inset shows the intrinsic activity for each surface can be assessed by the potential to achieve a given specific ORR current density. To obtain a reliable intrinsic nonaqueous ORR activity of the bulk surfaces, it is necessary to consider the degree of background correction and the self-poisoning due to solid product formation. To balance these two considerations, we select a specific net ORR current density of 2 $\mu A/cm^2_{true}$, where the self-poisoning is less than 10% of one monolayer solid product formation and the capacitive-correction is less than 50% as shown in Table 4-1 (based on Figure 4-4). The monolayer of the solid product is based on a reported value of 200 $\mu C/cm^2$ for LiO_2.[107] It should be noted that this assumption does not imply the formation of LiO_2 for all surfaces but rather represents the most conservative estimation for monolayer product formation since the charge for one monolayer material would be higher for Li_2O_2 ($2e^-/O_2$) and Li_2O ($4e^-/O_2$). Consequently, for Pd, Pt, Ru, Au and GC, the specific activity of 2 $\mu A/cm^2_{real}$ can be reached at a potential of 2.80 (± 0.02), 2.72 (± 0.02), 2.65 (± 0.01), 2.60 (± 0.03), and 2.57 (± 0.01) V_{Li}, respectively.

Table 4-1. Capacitive-correction and the self-poisoning evaluation at a specific ORR current of 2 $\mu A/cm^2_{true}$.

At 2 $\mu A/cm^2_{true}$	E (V_{Li})	i_{O2} ($\mu A/cm^2_{true}$)	i_{Ar} ($\mu A/cm^2_{true}$)	Capacitive correction i_{Ar}/i_{O2} (%)	Accumulated charge ($\mu C/cm^2_{true}$)	Monolayer fraction (%)
Pd	2.80	-2.6	-0.7	26	10.2	5
Pt	2.72	-2.9	-0.9	32	12.7	6
Ru	2.66	-4.3	-2.3	53	9	5
Au	2.62	-2.3	-0.4	16	11	6
GC	2.56	-2.4	-0.4	18	8	4

Interestingly, the intrinsic Li^+-ORR activities of the five surfaces exhibit a volcano shape as a function of the oxygen adsorption energy relative to that of Pt (per oxygen atom relative to an atom in the gas phase),[122,146] as shown in Figure 4-5.

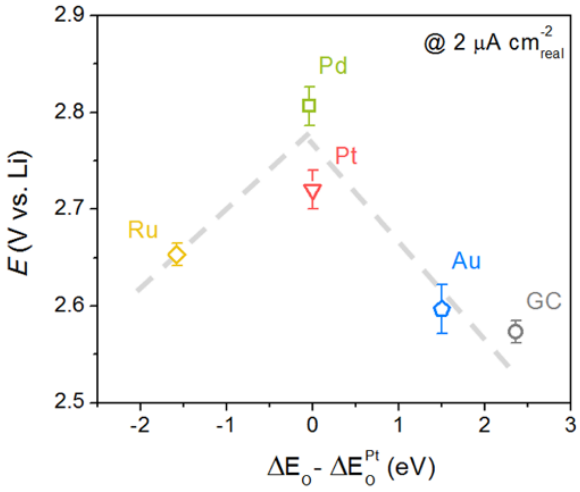

Figure 4-5. Nonaqueous Li^+-ORR potentials at 2 $\mu A/cm^2_{real}$ as a function of calculated oxygen adsorption energy, ΔE_O (per oxygen atom relative to an atom in the gas phase) (Hammer, B. et al., *Adv. Catal.* **45**, 71-129, (2000)), relative to that of Pt. The oxygen adsorption energy on GC is estimated from the oxygen adsorption energy on graphite (Sorescu, D. C. et al., *J. Phys. Chem. B* **105**, 11227-11232, (2001)). Error bars represent standard deviations of at least three independent measurements.

The activity increases from GC to Au followed by Pt and peaks at Pd as the oxygen adsorption energy increases. A further increase in the oxygen adsorption energy on Ru, results in a decrease in the activity compared to the peak (Pd), forming a so-called 'volcano'-type relationship. This volcano dependence suggests that the strength of oxygen binding on the catalyst surface greatly influences the ORR activity, at least in the present case of submonolayer coverages with discharge product. It should be noted that the ORR potential for GC in Figure 4-5 is lower than those typically found for carbon in the Li-O_2 cells. This difference can be attributed at least in part to the fact that the specific current of 2 $\mu A/cm^2_{real}$, which is constrained by ORR surface poisoning and background current correction, is much higher than those typically used in the Li-O_2 cells (≈ 0.1-0.2 $\mu A/cm^2_{carbon}$)[31,39,127,147]

4.3.2 Activity Trends of Nonaqueous Li^+-ORR Activity on High-Surface-Area Thin Film Catalysts

To bridge the intrinsic Li^+-ORR activity trends on the well-defined bulk surfaces to the discharge voltages of Li-O_2 cells, the activities of high-surface-area catalysts supported on Vulcan carbon (VC with 40% metal catalyst loading, Premetek, USA) were examined subsequently using RDE measurements. The weight percent of metal loading is defined as the weight of metal normalized to the weight of metal and carbon (metal/metal + C). We used a method developed recently[106,148] for the quantitative evaluation of the activities of high-surface-area catalysts dispersed as thin films on a GC RDE, where mass-transport resistances were negligible. Figure 4-6 shows the background- and IR-corrected (see Experimental Session) ORR current densities of Pd/C, Pt/C, Ru/C, Ru/C, Au/C and VC thin films normalized to carbon weight. It should be noted that current densities shown here are comparable to those typically used in the Li-O_2 cells (≈ 100 - 500 mA/g_{carbon}).[31,39,127] For Pd/C, Pt/C, Ru/C, Au/C and VC, the ORR activity of 100 mA/g_{carbon} can be reached at potential of 2.95, 2.86, 2.84, 2.76 and 2.74 V_{Li}, respectively. This is in agreement with the fact that at ~100 mA/g_{carbon}, the ORR voltage on carbon estimated from the RDE data in Figure 4-6 is ~2.7 V_{Li} is very consistent with those reported by a large number of Li-air cell studies.[31,39,127]

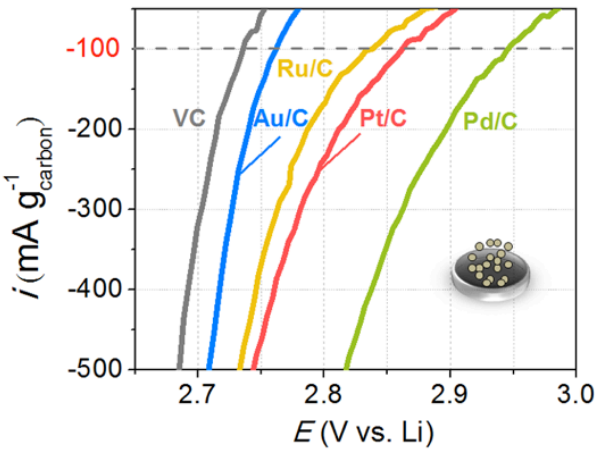

Figure 4-6. Background- and IR-corrected ORR polarization curves of Pd/C, Pt/C, Ru/C, Au/C, and VC thin films on GC (0.05 mg_{carbon}/cm^2_{disk}) in O_2-saturated 0.1 M $LiClO_4$ DME at 900 rpm and 5 mV/s.

With further consideration of estimated true surface area of each catalyst (see Experimental Session), the specific ORR current densities of high-surface-area catalysts were obtained as shown in Figure 4-7. The results are in reasonable agreement with the activity trend of polycrystalline surfaces shown in Figure 4-4. It should be noted that the specific current range evaluated for these high-surface-area catalysts (Figure 4-7) are comparable to those used typically in Li-O_2 cells (≈ 0.1-0.5 μA/$cm^2_{catalyst}$).[31,127,147]

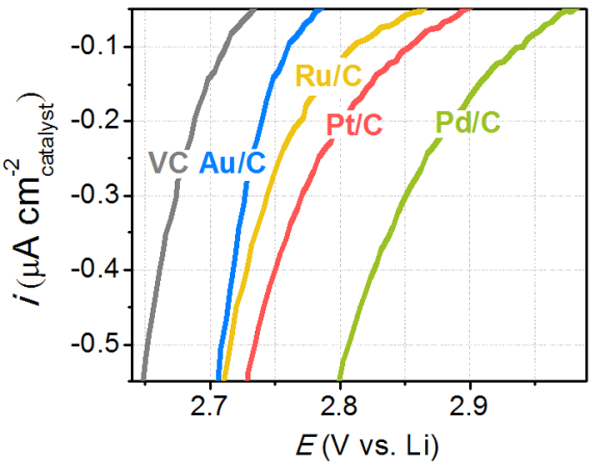

Figure 4-7. Capacitive and IR-corrected nonaqueous ORR polarization curves normalized by the true surface area of each catalyst for the Pd/C, Pt/C, Ru/C, Au/C and VC thin film RDE in 0.1 M $LiClO_4$ DME 5 mV/s and 900 rpm.

4.3.3 Discharge Voltage Trends of Li-O_2 Cells

We further show that the ORR activity trends found on bulk surfaces and high-surface-area catalysts from RDE measurements can be translated well to the discharge voltage trends of Li-O_2 cells. To eliminate water or air contaminations, all the Li-O_2 cells were tested in the water-free glovebox. All the air electrodes and separators (Celgard, C480) were vacuum-dried at 75 ^oC for at least 12 hours prior to transferring into an Ar-filled, water-free glovebox (H_2O < 0.1 ppm, O_2 < 0.1 ppm). The electrodes and the separators were kept in the vacuum oven and directly transferred to the glovebox without exposure to the ambient. The Li-O_2 cell consists of lithium foil, two Celgard separators, 150 μL O_2-saturated 0.1 M $LiClO_4$ DME as the electrolyte. The composition and weight of the O_2-electrode are available in the Experimental Session. To minimize the self-poisoning effect, the initial discharge voltage

profiles were used to access the activities of the catalysts as shown in Figure 4-8, where full discharge profiles are shown in Figure 4-9.

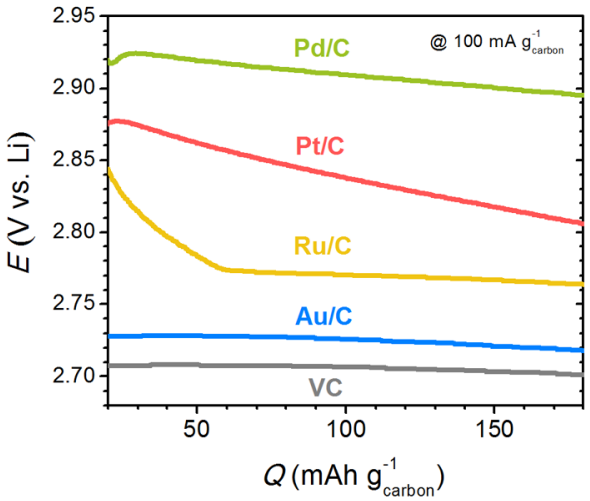

Figure 4-8. Initial discharge profiles of Li-O_2 cells of Pd/C, Pt/C, Ru/C, Au/C, and VC at 100 mA/g_{carbon}.

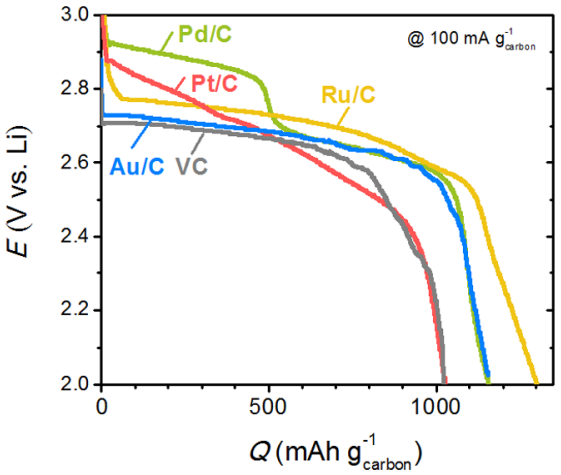

Figure 4-9. Discharge profiles of VC, Au/C, Ru/C, Pt/C and Pd/C in Li-O_2 cells at 100 mA/g_{carbon}.

The initial discharge voltages of the Li-O_2 cells were compared to those found in the high-surface-area thin film RDE at 100 mA/g_{carbon} (Figure 4-6) as shown in Figure 4-10, confirming a good agreement between the two methods.

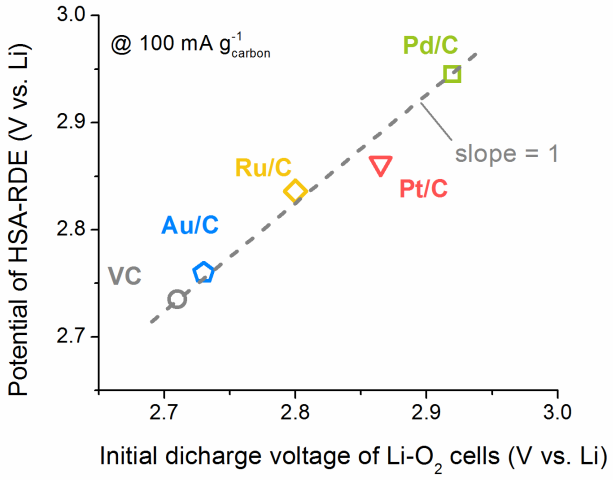

Figure 4-10. The potentials of the high-surface-area thin film RDE at 100 mA/g_{carbon} as a function of the initial discharge voltages (at Q = 40 mAh/g_{carbon}) of the Li-O_2 cells at 100 mA/g_{carbon}.

4.3.4 Proposed ORR Mechanisms in Li^+-Containing Nonaqueous Solvents

Based on the observed volcano-type dependence on the nonaqueous Li^+-ORR activity and several previous studies,[116,119,131,149] we here propose the ORR mechanism in Li^+-containing nonaqueous solvents as shown in Figure 4-11.

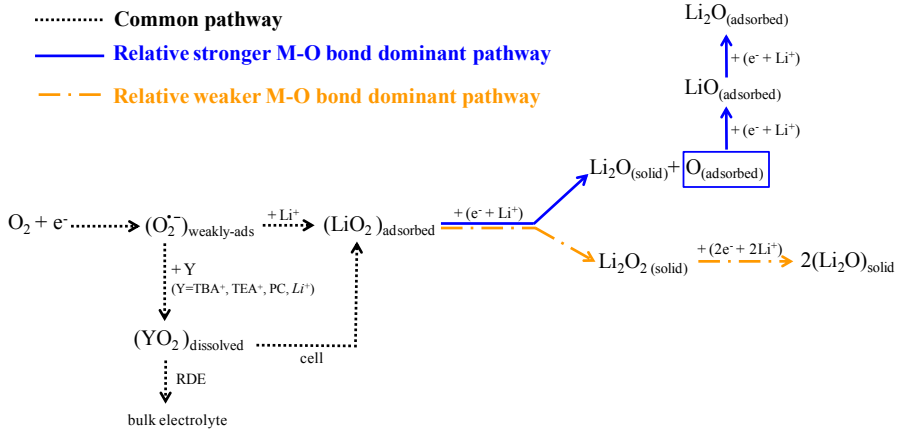

Figure 4-11. Proposed ORR mechanisms for Li^+-containing nonaqueous solvents.

The first step in the ORR in Li^+-containing nonaqueous solvents may proceed according to:

$$O_2 + e^- \rightarrow \left(O_2^{\bullet -}\right)_{weakly-adsorbed} \qquad (4\text{-}1a)$$

forming superoxide radicals as a weakly adsorbed species, which might be subsequently solvated by various species such as salt cations (TBA^+, TEA^+ or Li^+) or solvents (PC)[107] and then diffuse into the bulk of the electrolyte, particularly when the electrode is rotated (RDE method):

$$\left(O_2^{\bullet-}\right)_{weakly-adsorbed} \xrightarrow{+Y\ (Y=TBA^+,\ TEA^+,\ PC,\ Li^+)} \left(YO_2\right)_{dissolved} \xrightarrow{RDE} \text{bulk electrolyte} \quad (4\text{-}1b)$$

which is consistent with the observed imbalance of cathodic and anodic charges. Alternatively, the weakly adsorbed superoxide radicals could react with Li^+ to form surface adsorbed LiO_2:

$$\left(O_2^{\bullet-}\right)_{weakly-adsorbed} + Li^+ \rightarrow (LiO_2)_{adsorbed} \quad (4\text{-}1c)$$

It should be noted that the sum of Reactions 4-1a and 4-1c corresponds to the first reduction step proposed in a recent DFT study on the ORR in Li-air batteries.[26] Furthermore, the species $(YO_2)_{dissolved}$ for Y=Li in Eq. 4-1b could also diffuse and adsorb onto the active surface to form surface adsorbed LiO_2, particularly for a very small ratio of electrolyte volume to electrode surface area as is the case in a Li-O_2 cell:

$$\left(LiO_2\right)_{dissolved} \xrightarrow[cell]{adsorption} (LiO_2)_{adsorbed} \quad (4\text{-}1d)$$

The subsequent dominant pathways are considered strongly dependent on the oxygen adsorption nature of the catalyst surface. In the case of relative weakly oxygen chemisorptions (e.g., carbon), the surface adsorbed LiO_2 can be reduced to Li_2O_2[26] (Eq. 4-2a) and/or undergo disproportionation to Li_2O_2,[131] (Eq. 4-2b) which is supported by the fact that Li_2O_2 has been detected on the surfaces of carbon and carbon-MnO_2 composites by ex-situ[21,31] and in-situ[131] Raman spectroscopy.

$$(LiO_2)_{adsorbed} + e^- + Li^+ \rightarrow (Li_2O_2)_{solid} \quad (4\text{-}2a)$$

$$(LiO_2)_{adsorbed} + (LiO_2)_{adsorbed} \rightarrow (Li_2O_2)_{solid} + O_2 \quad (4\text{-}2b)$$

Further reduction of Li_2O_2 to Li_2O is thermodynamically possible in the typical discharge potential range of Li-O_2 batteries (2.8 to 2.0 V_{Li}):

$$(Li_2O_2)_{solid} + 2e^- + 2Li^+ \rightarrow 2(Li_2O)_{solid}, \text{ with } E_{rev} = 2.86\ V_{Li}^{25} \quad (4\text{-}2c)$$

which is not an elementary step. On the other hand, in the case of catalysts forming a strong bond with atomic oxygen, e.g., in the case of Pt in contrast to carbon (≈4.2 eV[146] vs. ≈1.8 eV[122]), the ORR in aprotic electrolytes with lithium ions may mostly proceed via a reaction mechanism analogous to that established for the ORR on platinum metals in aqueous electrolytes[150]:

$$(LiO_2)_{adsorbed} + e^- + Li^+ \rightarrow (Li_2O)_{solid} + O_{adsorbed} \quad (4\text{-}3a)$$

$$O_{adsorbed} + e^- + Li^+ \rightarrow (LiO)_{adsorbed} \quad (4\text{-}3b)$$

$$(LiO)_{adsorbed} + e^- + Li^+ \rightarrow (Li_2O)_{adsorbed} \quad (4\text{-}3c)$$

Considering the ORR pathways outlined above and the fact that the dominant ORR product on Au and Pt in aqueous solutions is H_2O_2 and H_2O, respectively, the nature of the Li^+-ORR products are likely to depend on the catalyst too, with a preference for Li_2O_2 formation for catalysts that have low oxygen adsorption strength (e.g., Au and C), and a preference for Li_2O for catalysts with high oxygen-catalyst bond strength (e.g., Pt). We will examine the discharge products with and without catalyst in the later session. Furthermore, it is interesting to note that the nonaqueous Li^+-ORR activity trend observed in this work is well-correlated to that for alkaline ORR, as shown in Figure 4-12.

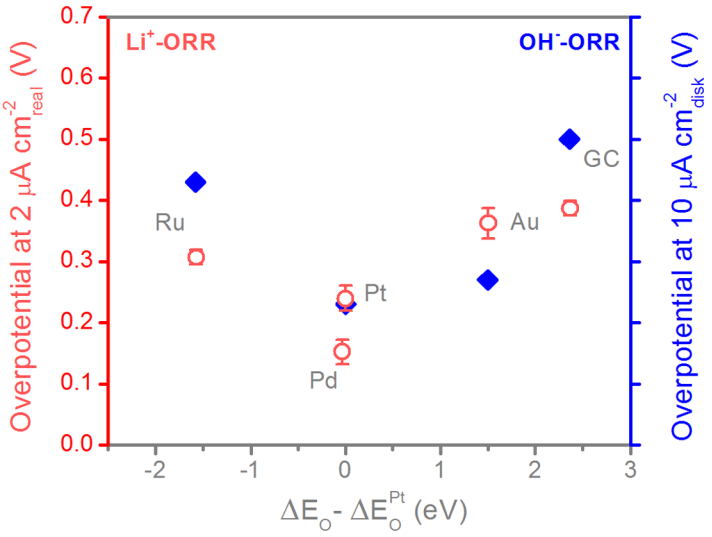

Figure 4-12. The overpotentials of the nonaqueous Li^+-ORR at 2 μA/cm^2_{real} and alkaline OH^--ORR at 10 μA/cm^2_{disk} (Ru is estimated from Lima, F. et al., *J. Phys. Chem. C* **111**, 404-410, (2007)) as a function of calculated oxygen adsorption energy, ΔE_O (Hammer, B. et al., *Adv. Catal.* **45**, 71-129, (2000)), (Sorescu, D. C. et al., *J. Phys. Chem. B* **105**, 11227-11232, (2001)).

4.3.5 Catalyst Effects on the Discharge Rate Capability of Li-O_2 Cells

To examine the catalyst effects on the discharge rate capability of the Li-O_2 cells, we compare the rate capability of Li-O_2 cells with pure Vulcan carbon (VC) and 40 weight percent (wt%) Au-nanoparticles supported on Vulcan carbon (Au/C).

Rate Capability Data of Li-O_2 cells. Four key observations can be made from the rate capability data of Li-O_2 cells shown in Figure 4-13. First, the discharge voltages of Li-O_2 cells with Au/C are higher than those with VC at all current densities. The enhancement in the initial discharge voltage at ~50 mAh/g_{carbon} associated with Au/C at low rates can be attributed to the higher ORR activity of Au relative to VC, which will be discussed in detail. Second, similar specific capacities (normalized by carbon mass) were obtained for Li-O_2 single cells tested at relatively low rates (i.e., 100 – 500 mA/g_{carbon}). The results support that the discharge capacity is mainly influenced by the electrode structures (i.e., porosity),[151] and electrolyte formulations.[27,28,151] By comparing with discharge capacities

reported in previous work, we will discuss how the low-rate discharge capacity is governed primarily by oxygen solubility in the electrolyte. Third, the discharge capacities and voltages of Li-O_2 cells with Au/C and VC were found to reduce significantly with increasing current densities. Unlike previous studies with PC-containing electrolytes,[27,28] we show that the discharge capacity and voltage of Li-O_2 cells at high current densities are not likely limited by O_2 concentration gradients across the electrode thickness based on the electrolyte transport properties with DME, which will be presented in detail below. Fourth, although solid ORR products form during discharge, the voltage enhancement due to Au/C in the Li-O_2 cells at low rates is evident over the entire discharge process, which suggests that ORR is catalyzed by Au throughout most of the discharge, analogous to what has been reported previously for Li-O_2 cells using a PC:DME-based electrolytes,[125,127] and for the ice formation during ORR in a fuel cell at -20°C.[34]

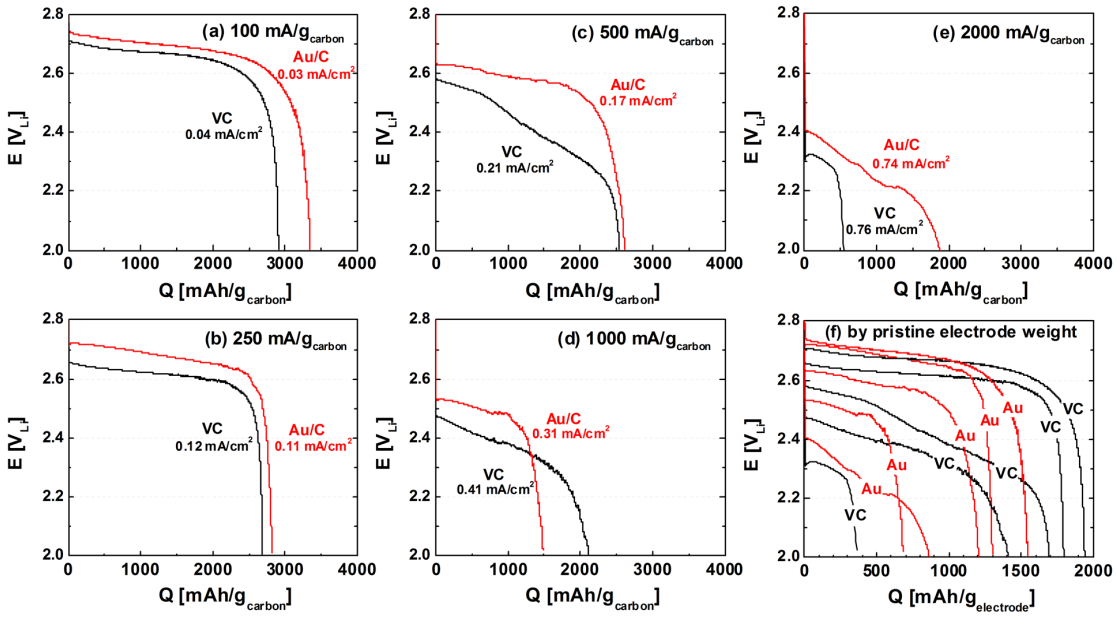

Figure 4-13. Discharge profiles of Li-O_2 single cells of VC and Au/C at (a) 100 mA/g_{carbon}, (b) 250 mA/g_{carbon}, (c) 500 mA/g_{carbon}, (d) 1000 mA/g_{carbon}, and (e) 2000 mA/g_{carbon}. (f) Data shown in Figure 4-13a to Figure 4-13e were normalized by the total weight of air electrode before discharge (carbon + catalyst + binder).

Proposed Physical Origin of the Enhancement in the Discharge Voltage of Li-O_2 Cells with Au/C Relative to VC. At very low rates (100 and 250 mA/g_{carbon}), the discharge voltages of Li-O_2 cells with Au/C are consistently higher than those of VC, as shown in Figure 4-13a and Figure 4-13b. The increase in the discharge voltage promoted by Au/C was ~40 mV (2.74 V_{Li} vs. 2.70 V_{Li}) at 100 mA/g_{carbon}, ~70 mV (2.72 V_{Li} vs. 2.65 V_{Li}) at 250 mA/g_{carbon}. The enhancement can be mainly attributed to intrinsically higher ORR activity on Au than carbon measured by RDE discussed previously. The ORR potential of pure Au surface is about 90 mV higher than that of pure GC as shown in Figure 4-4. Interestingly, the enhancement in the discharge voltage associated with the Au nanoparticles increases as rate increases. For instance, Figure 4-13c shows that the increase in the discharge voltage due to Au at 500 mA/g_{carbon} can be greater than 100 mV, which is greater than the difference in the ORR potential between pure Au and pure carbon (Figure 4-4). Therefore, the results from RDE alone cannot fully explain the enhancement observed in the rate capability test at rates larger than 500 mA/g_{carbon}. We will discuss possible explanations in the later session.

The discharge voltages of Li-O_2 cells found in this study compare well with those reported previously,[27,35,37,102,127] as a function of currents normalized to geometric electrode area in Figure 4-14a and carbon mass in the electrode in Figure 4-14b. There is visible scattering in the discharge voltage at a given geometric electrode current density across multiple studies[27,35,37,102,127] with different electrode thicknesses and formulae, as shown in Figure 4-14a. Although the current based on the geometric area has direct practical engineering implications for the development of Li-air battery technologies, the current normalized to the true surface area of the electrode or electrode carbon mass is better correlated to the catalytic activity of electrode material. Surveying all the studies, where both currents normalized to the geometric electrode area and electrode carbon mass are available, the currents normalized to carbon mass were found to greatly influence the discharge voltages (Figure 4-14b), where the discharge voltage decreased with increasing carbon-mass-normalized currents. Although Au/C catalyst promotes the discharge voltage of Li-O_2 cells under all current densities relative to VC, the difference is more pronounced when the carbon-mass-normalized current is used for comparison. Both O_2 transport

resistance in the electrolyte-filled pores of the electrode and the resistance in the solid-state diffusion of Li^+ in the ORR discharge products may contribute to the discharge voltage decrease with increasing current densities.

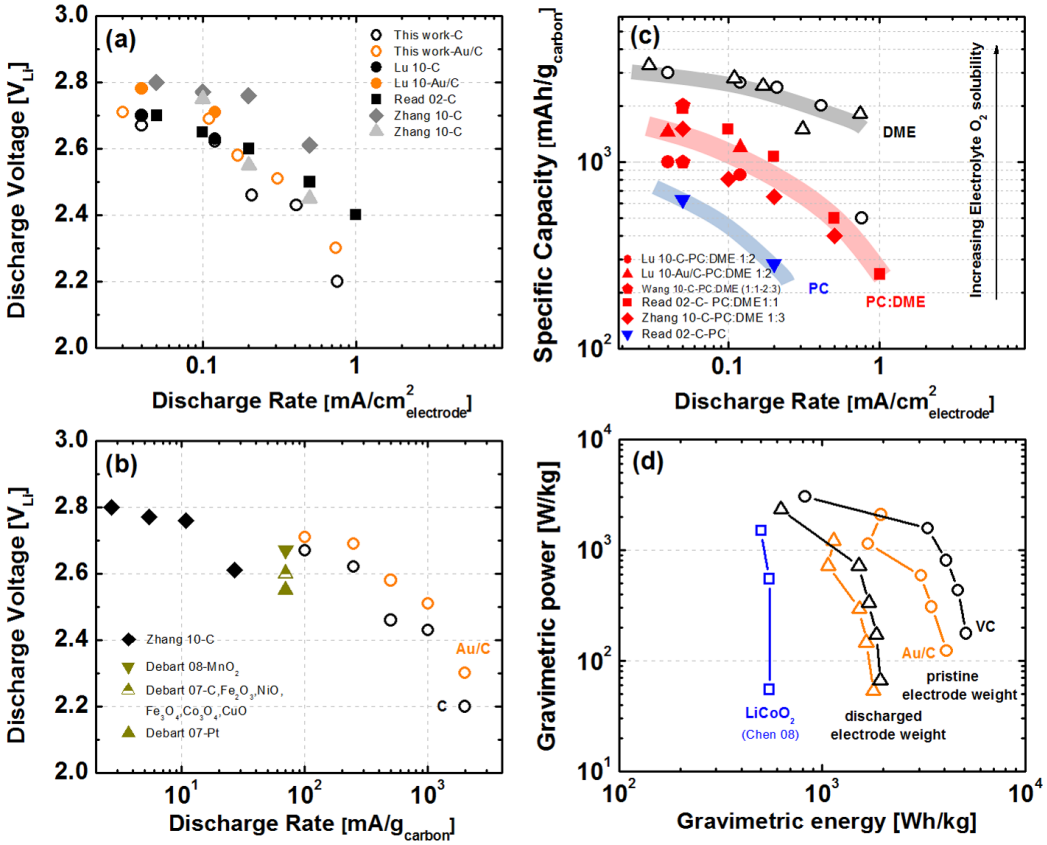

Figure 4-14. Comparison of the discharge voltage (a),(b) and discharge capacity (c) of Li-O_2 cells at various rates normalized to electrode geometric area (a), (c) and carbon mass (b). Rogone plot (d) for Li-O_2 cells with VC electrode (by pristine electrode weight (carbon + catalyst + binder): black circles; by discharged electrode weight (carbon + catalyst + binder + discharge products): black triangles), Au/C electrode (by pristine electrode weight (carbon + catalyst + binder): orange circles; by discharged electrode weight (carbon + catalyst + binder + discharge products): orange triangles) and conventional Li-$LiCoO_2$ cell reported previously[152] (Chen, H. et al., *Chemsuschem* **1**, 348-355, (2008).) (blue squares).

The Influence of O_2 Solubility in the Electrolyte on the Discharge Capacity at Low Current Densities. Similar discharge capacities (normalized by carbon mass) on the order

of 2500 to 3000 mAh/g_{carbon} were obtained for Li-O_2 single cells with Au/C and VC tested at low current densities (i.e., 100 – 500 mA/g_{carbon}). It is interesting to note that having Au/C with higher ORR activity than VC does not influence the discharge capacity at low rates. In addition, the discharge capacities found in this study are considerably larger than those reported previously,[31,35,39,108] as shown in Figure 4-14c. This difference can be attributed to much higher O_2 solubility in DME used in this work than PC-containing electrolytes in the previous work (Table 4-2).

Table 4-2. Properties of electrolytes with DME, PC:DME (1:2) and PC, which were cited and derived from previous work including Read, J. et al, *J. Electrochem. Soc.* **150**, A1351-A1356, (2003), Saito, Y. et al., *J. Mater. Sci.* **35**, 809-812, (2000), and Hayamizu, K. et al., *Electrochim. Acta* **49**, 3397-3402, (2004).

Property	0.1 M Li^+ in DME	1 M Li^+ in PC:DME (1:2)	1 M Li^+ in PC
Solubility of O_2 in the electrolyte (M)	**0.00876** (Read 03)	**0.0041** (Read 03)	**0.0021** (Read 03)
D_{O2} in the electrolyte (cm^2/s)	**$4 \cdot 10^{-5}$** (Ref.[126])	**$9 \cdot 10^{-6}$** (Ref.[126])	**$2.2 \cdot 10^{-6}$** (Ref.[126])
Lithium transference number	**0.4 - 0.5** (Saito 00)	**0.43** (Ref.[126])	**0.35** (Ref.[126])
D_{Li+} in the electrolyte (cm^2/s)	**$\approx 1 \cdot 10^{-5}$** (Hayamizu 04 & Saito 00)	**$8 \cdot 10^{-7}$** (Ref.[126])	**$3 \cdot 10^{-7}$** (Ref.[126])

Gravimetric Energy and Power Characteristics of Li-O_2 Cells. As Au nanoparticles in Au/C significantly add to the electrode weight, the discharge capacities of Li-O_2 cells with Au/C, which were normalized to the total electrode weight in the pristine state (before discharge), were found largely smaller than those of VC electrodes, as shown in Figure 4-14d. The gravimetric energy of Li-O_2 cells before discharge (carbon + catalyst + binder) was obtained by integrating the area underneath the discharge voltage profile, and the gravimetric power was calculated by normalizing the gravimetric energy by the discharge time (Figure 4-14d). Although both Au/C and VC electrodes were found to have comparable gravimetric power, the VC electrodes showed slightly larger gravimetric energy than the Au/C electrodes before discharge. However, the gravimetric difference was

reduced significantly and Au/C and VC electrodes were found to have very comparable gravimetric energy when the weight of discharged electrodes (carbon + catalyst + binder + discharge products). Addition of discharge ORR products to the weight of pristine electrodes under the assumption that all the charge is associated with Li_2O_2 formation was considered (Figure 4-15).

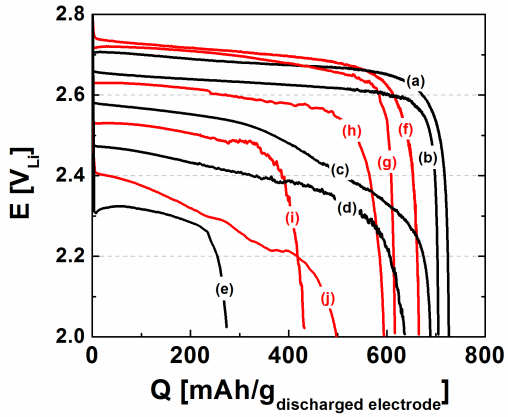

Figure 4-15. Discharge profiles of Li-O_2 single cells of pure Vulcan (a)-(e) and Au/C. The discharge rate is 100 mA/g_{carbon} for (a) and (f), 250 mA/g_{carbon} for (b) and (g), 500 mA/g_{carbon} for (c) and (h), 1000 mA/g_{carbon} for (d) and (i), and 2000 mA/g_{carbon} for (e) and (j).

It should be noted that the enhancement in the voltage associated with Au nanoparticles did not lead to increased gravimetric energy due to additional weight of Au nanoparticles as shown in Figure 4-14d. Lowering the loading of Au nanoparticles on VC and using smaller Au particles (very large 10+ nm Au particles were used here) may potentially increase the gravimetric energy of Au/C electrodes relative to VC electrodes. Interestingly, Au/C and VC electrodes even in the discharged state showed gravimetric energy (~2000 Wh/kg) three or four times higher than that of $LiCoO_2$ (~600 Wh/kg) used for Li-ion batteries reported previously.[152] Using the conventional rule of thumb, where the gravimetric energy of a lithium cell can be estimated as one-third that of the positive electrode, the gravimetric energy of Li-O_2 cells can be estimated as ~670 Wh/kg, which is significantly greater than those projected for Li-ion batteries. It should be noted that on the volumetric basis, the advantage of Li-O_2 cells relative to Li-ion batteries will be much smaller than that estimated on the weight basis shown in Figure 4-14d as the apparent

densities of O_2 electrodes used here are considerably lower than that of $LiCoO_2$ electrodes used in Li-ion batteries.

Proposed Physical Origin of the Reduction of the Discharge Voltage and Capacity with Increasing Current Densities. At high rates (1000 and 2000 mA/g_{carbon}), not only the discharge voltages but also the discharge capacities were reduced considerably relative to those at low current densities. Previous studies[27,151] have reported that the discharge capacity at high current densities is limited by the oxygen flux in the electrolyte-filled pores across the electrode thickness for electrolyte-flooded O_2 electrodes.[28,29,151] Considering the electrode thickness of 20 μm and estimated Li^+ and O_2 diffusion coefficients of 0.1 M $LiClO_4$ in DME (Table 5-2), the limiting flux of Li^+ and O_2 across the electrolyte-flooded electrode is $3\cdot10^{-7}$ and $9\cdot10^{-8}$ $mol\cdot cm^{-2}\cdot s^{-1}$, respectively. These values are much higher than that of $4\cdot10^{-9}$ $mol_{O2}\cdot cm^{-2}\cdot s^{-1}$ corresponding to 0.8 mA/cm^2 – the highest current density used in this study. Therefore, it is believed that the reduction in the discharge capacity is not caused by the depletion of O_2 in the electrolyte-filled pores across the electrode thickness.

To further support that O_2 flux in the O_2 electrode does not limit the discharge capacity of Li-O_2 cells at current densities tested in Figure 4-13, we use the following equation reported by Read et al.[28] previously to model the dimensionless concentration of O_2 in the electrolyte-filled pores across the electrode

$$\frac{C(x)}{C_o} = \exp\left(-x\frac{j}{nFC_oD_{eff}}\right)$$

where C(x), C_o, j, n, and D_{eff} are the concentration of O_2 in the electrolyte-filled pores at distance x from the electrode-O_2 interface, the O_2 solubility in the electrolyte, the geometric-area-normalized current density, the number of electrons transferred, and the effective diffusion coefficient of O_2 in the porous electrode**,** respectively ($D_{eff} = D\cdot\varepsilon^{\beta-1}$ where β is the Bruggeman constant of O_2 in the porous electrode (β=3 used)[151] and D the diffusion coefficient of O_2 in the electrolyte). The concentrations of O_2 in the electrolyte-filled pores from the electrode-separator interface to the electrode-O_2 interface are shown in Figure 4-16. Using DME as the electrolyte solvent and at a current density of 0.8

mA/cm^2, there is negligible drop in the O_2 concentration across the electrode thickness with an electrode porosity of 0.73 (circle), which represents the porosity of pristine PTFE or PVDF-bonded electrodes[27] (lower than the average porosity – ~0.85 of pristine VC-based electrodes used in this study).[33] This is in contrast to electrolytes with PC as the solvent or one solvent component, where increasing PC in the electrolyte leads to large reduction in the O_2 diffusivity and solubility and thus large drops in the O_2 concentration across the electrode, as shown in Figure 4-16. In addition, it is interesting to note that even at the end of discharge where the porosity is reduced largely by the ORR products to approximately 0.3 (square), which represents the average porosity at the end of discharge with ~3000 mAh/g_{carbon},[102] the O_2 concentration gradient in the electrode is reasonably small for 0.1 M $LiClO_4$ in DME. In contrast, this is not the case for PC-containing electrolytes as a large concentration gradient of O_2 develops for 1 M $LiClO_4$ PC:DME v:v 1:2 under the same condition. Therefore, it is advantageous to use DME as the electrolyte solvent due to its high solubility of O_2. However, its high volatility and low solubility for Li salts can present some engineering challenges for developing practical Li-air batteries.

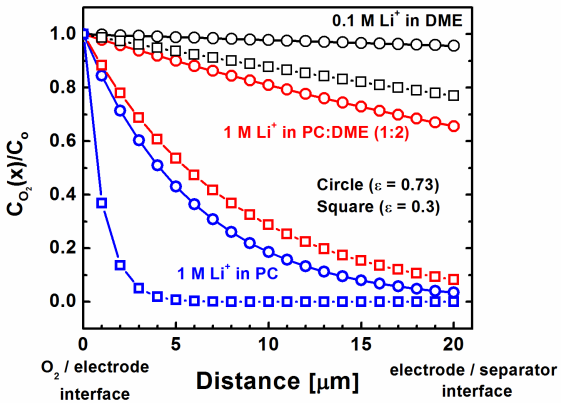

Figure 4-16. Dimensionless oxygen concentration in flooded porous electrode. ε = 0.73 and ε = 0.3 correspond to the electrode porosity at the onset of discharge and a discharge state of ~2500 mAh/g_{carbon} at a rate of j = 0.8 mA/cm^2, respectively.

To explain decreased discharge voltage and capacities at high current densities found in this study such as 1000 and 2000 mA/g_{carbon} (Figure 4-13), we propose that the resistance of Li^+ diffusion in the solid ORR products limits the rate capability of

Li-O_2 cells tested in this study. In order to understand the nature of ORR products formed on discharge, pristine and discharged VC (Figure 4-17a) and Au/C (Figure 4-17b) electrodes at 100 mA/g_{carbon} and 2000 mA/g_{carbon} were examined by XRD, where discharged electrodes were protected in Ar during XRD data collection. The additional peaks in all the discharged electrodes examined compared to pristine electrodes were assigned to lithium peroxide, suggesting that it is the dominant crystalline ORR product. This is consistent with the proposed reaction mechanism shown in Figure 4-11 that the Li^+-ORR dominant products on Au and Carbon surface are lithium peroxide. In addition, considerable broadening was noted in the peaks of lithium peroxide, which could be attributed to the broadening of small crystallite sizes of lithium peroxide, structural defects and/or nonstiochiometry in lithium peroxide such as lithium vacancies resembling $Li_{2-x}O_2$. Moreover, the peaks of lithium peroxide in the discharged electrodes of Au/C are broader than those in the discharged electrodes of VC. Different crystallite sizes and/or different amounts of structural defects and compositional nonstoichiometry may explain this difference, which were examined by SEM and O and Li K edge XANES in detail below, respectively.

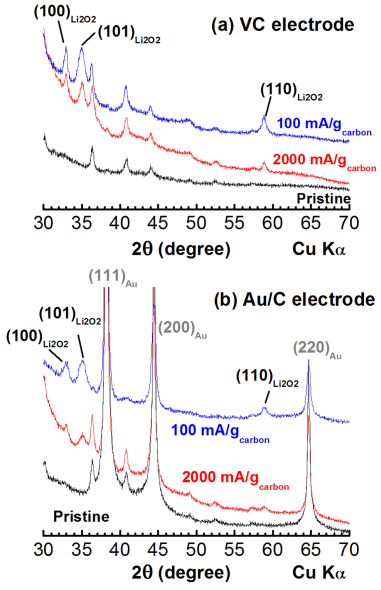

Figure 4-17. XRD patterns of pristine and discharged electrodes supported on a Celgard 480 separator (100 and 2000 mA/g_{carbon}) for VC (a) and Au/C (b). The reflections appeared in the

pristine VC electrode came from Celgard C480 and those appeared in the pristine Au/C electrode came from Au nanoparticles and Celgard C480.

Particle Sizes of Li^+-ORR Product(s) in the Discharged Electrodes. The morphological changes of air electrodes before and after discharge at 100 mA/g_{carbon} for VC and Au/C electrodes are shown in Figure 4-18a to Figure 4-18d.

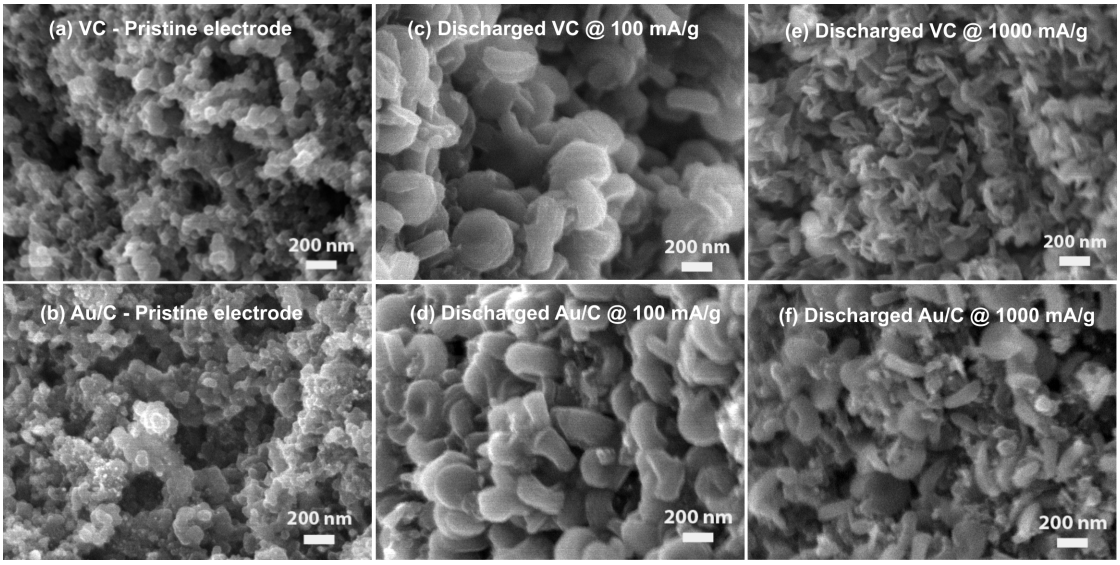

Figure 4-18. SEM images of (a) pristine VC electrode, (b) pristine Au/C electrode, (c) VC electrode discharged at 100 mA/g (2500 mAh/g_{carbon}), (d) Au/C electrode discharged at 100 mA/g (2500 mAh/g_{carbon}), (e) VC electrode discharged at 1000 mA/g (1400 mAh/g_{carbon}), and (f) Au/C electrode discharged at 1000 mA/g (1500 mAh/g_{carbon}). The SEM images were taken from the surface of the air electrode on the O_2 side.

Figure 4-18a shows that VC with primary particle sizes in the range from 50 to 100 nm creates a porous structure to provide electronic conductivity and interconnected pores for electrolyte for both pristine VC and Au/C electrodes. It is important to point out that the addition of Au nanoparticles is not expected to change the electrode porosity/structures as the density of Au (19.3 g/cm^3) is much higher than VC (~2 g/cm^3) thus the volume of gold nanoparticles is negligible compared to carbon particles for 40 wt% Au/C. After discharge at 100 mA/g, the entire electrode surface in the O_2 side for both Au/C and VC was found to be covered by donut-shaped particles (presumably lithium

peroxide) on the order of 350 nm. At a high current density of 1000 mA/g_{carbon}, the particle sizes of ORR product(s) in the discharged electrodes of Au/C and VC are very comparable but smaller than those found at 100 mA/g_{carbon}, as shown in Figure 4-18e and Figure 4-18f, respectively. Assuming that these donut-shaped particles were single-crystalline, which needs to be verified by electron diffraction in the TEM or high-resolution TEM imaging, comparable particle sizes of lithium peroxide found in the electrodes discharged at high rates cannot explain the greater broadening of XRD peaks found for the discharged Au/C electrodes. The greater broadening of XRD peaks could result from more structural defects and/or composition nonstoichiometry of lithium peroxide in the discharged electrodes of Au/C. High-resolution TEM imaging and electron diffraction was used to examine potential structural defects in lithium peroxide particles. However, these particles were found unstable under electron beam at high magnifications. Cryo-TEM will be used to examine discharged electrodes in future studies to minimize the instability of lithium peroxide particles induced by heating associated with electron beam.

Probing O and Li Local Environment in Discharged Electrodes. The O and Li K edge XANES of discharged VC and Au/C electrodes at 100 mA/g_{carbon} and the spectra of reference materials including Li_2O_2, Li_2O and $LiCoO_2$[153] are shown in Figure 4-19. XANES peak position and intensities of reference compounds were used to serve as the fingerprints to identify the local environment of Li and O in the discharged electrodes. All reference materials with known crystal structures display their unique spectroscopy signature in their O and Li K edge XANES, which demonstrates the elegant chemical specification capability of XANES. Figure 4-19a shows that the FY O K edge XANES of discharged VC and Au/C electrodes are in reasonable agreement with both FY and TEY spectra of Li_2O_2, suggesting that the O local environment of the discharge product is Li_2O_2-like. The small difference in the FY O K edge XANES between discharge products and reference Li_2O_2 may suggest the presence of structural defects and/or nonstoichiometry such as lithium vacancies. Li K edge XANES of the discharge products were found to have a major peak at 62.0 eV having a small pre-edge (at 58.0 eV) followed by a broad peak at ~ 70.0 eV. In contrast, the Li K edge XANES spectra of the discharge products do not match well with that of reference Li_2O_2 nor any other references (Figure 4-20). This result

suggests that although XRD data show direct evidence of long-range ordering of lithium and oxygen in the Li_2O_2-like crystal structure, the Li^+ local environment in the lithium peroxide of discharged electrodes is different from that of Li_2O_2. Interestingly, Li K edge XANES spectra of discharge products resemble that of Li_xTiO_2 in both energy and shape while they resemble that of $LiCoO_2$ in shape and have a binding energy about 0.5 eV higher, where Li^+ ions are coordinated with 6 oxygen in Li_xTiO_2 and $LiCoO_2$.[153] It is hypothesized that the spectrum difference between discharge products and reference Li_2O_2 can be attributed to the presence of structural defects in lithium peroxide such as oxygen and/or lithium vacancies, which has been suggested previously in a DFT study.[26] Further studies to understand the role of catalyst on affecting the growth mechanism and the nonstoichiometry and structural defects ORR product(s) are needed to verify the hypothesis proposed in this study.

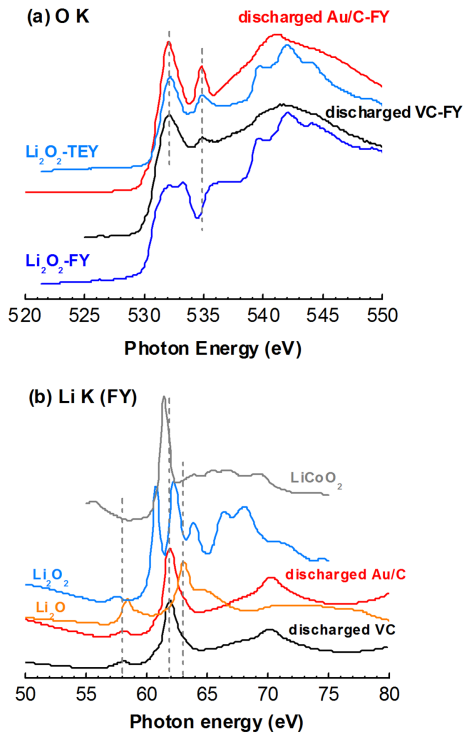

Figure 4-19. (a) O K edge and (b) Li K edge XANES FY spectra of reference compounds Li_2O_2, Li_2O, $LiCoO_2$ (Zhou, J. et al., *J. Mater. Chem.* **19**, 6804-6809, (2009)) and discharged VC and Au/C electrodes at 100 mA/g_{carbon}.

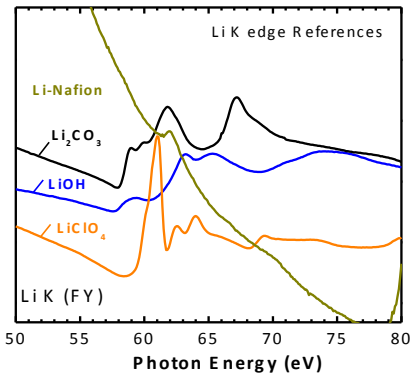

Figure 4-20. Li K edge XANES spectra of reference compounds: Li-Nafion, Li_2CO_3, LiOH, and $LiClO_4$.

4.4 Conclusions

In summary, we show that the Li^+-ORR activity is in order of Pd > Pt > Ru ≈ Au > GC on well-defined bulk surfaces. Such trend can be translated well to that of high-surface-area thin film catalysts supported on GC electrode and early discharge voltages of Li-O_2 cells. Oxygen adsorption energy on the surface can greatly influence Li^+-ORR activities and form a volcano dependence, which may be used to design highly active ORR surfaces with and electrodes with high discharge voltages for Li-air batteries.

In addition, we proposed the ORR mechanism in Li^+-containing nonaqueous solvents and provide insights to explain the observed volcano-type dependence on the nonaqueous Li^+-ORR activity. On surfaces with weak binding with oxygen such as Au and GC, LiO_2 may disproportionate[131] or undergo a second-electron reduction to form lithium peroxide, which is consistent with XRD results reported here. With surfaces with increasing binding energy with oxygen such as Pt and Pd, it is proposed that the kinetics of the second-electron reduction is enhanced to form $Li_2O + O_{adsorbed}$[125] similar to that established for the ORR on Pt and Pt alloy metals in aqueous electrolytes,[136] where $O_{adsorbed}$ subsequently undergoes additional two-electron reduction to form Li_2O.[125,154] However, no direct evidence of Li_2O formation can be found in the literature to date. Further studies involving *in situ*

spectroscopy techniques and differential electrochemical mass spectrometry are needed to verify the formation of Li_2O and the proposed mechanism.

Furthermore, we show that the discharge voltage of Li-O_2 single cells at low rates can be governed by the intrinsic ORR activity of electrode surfaces, where the application of Au nanoparticles enhances the discharge voltage of relative to VC. With increasing rates from 100 mA/g_{carbon} to 2000 mA/g_{carbon}, both the discharge voltages and capacities of Li-O_2 cells decrease for both VC and Au/C electrodes. Unlike PC-containing electrolytes, we show that the reduction in the discharge capacity at high rates is not a result of the depletion of O_2 in the electrolyte-filled pores across the electrode thickness based on the transport properties of 0.1 M $LiClO_4$ DME. We hypothesize that the large reduction in the discharge voltage and capacity with increasing rates can be attributed to the resistance associated with solid-state Li^+ diffusion in the lithium peroxide during discharge. Although XRD, O K edge and Li K edge XANES data suggest the presence of structural defects and/or composition nonstoichiometry such as lithium vacancies in the lithium peroxide formed on discharge, further studies are needed to test this hypothesis. The enhancement in the discharge voltage associated with Au/C relative to VC at high rates may result in part from faster solid-state Li diffusion associated with different structural defects and nonstoichiometry of lithium peroxides catalyzed by Au/C from those of VC, which needs to be examined in future studies.

Chapter 5. Catalyst Effects on the Charge Reactions of Rechargeable Li-Air Batteries in Li^+-Containing Nonaqueous Media

Reproduced in part with permission from (1) Yi-Chun Lu, Hubert A. Gasteiger, Michael C. Parent, Vazrik Chiloyan, and Yang Shao-Horn, The Influence of Catalysts on Discharge and Charge Voltages of Rechargeable Li-Oxygen Batteries, **Electrochem. Solid State Lett.** 2010, 13, A69-A72, Copyright 2010 The Electrochemical Society; (2) Yi-Chun Lu, Zhichuan Xu, Hubert A. Gasteiger, Shuo Chen, Kimberly Hamad-Schifferli, and Yang Shao-Horn, Platinum-Gold Nanoparticles: A Highly Active Bifunctional Electrocatalyst for Rechargeable Lithium-Air Batteries, **J. Am. Chem. Soc.** 2010, 132, 12170-12171, Copyright 2010 American Chemical Society.

5.1 Introduction

One of the most critical challenges facing rechargeable Li-O_2 batteries is the poor round-trip efficiency (53 – 64 %,[39] 70 %,[31]), owing to the enormous overpotential required during lithium (per)oxide decomposition on recharge (OER). Unlike the discharge reaction (ORR), where carbon itself is sufficiently high to provide an average voltage of 2.6-2.7 V_{Li} (≈ an overpotential of 300-400 mV) the charging activity of carbon is extremely poor, with an average voltage plateau of ≈ 4.2-4.5 V_{Li}[39,138] (≈ an overpotential of 1200-1500 mV). Extensive efforts have examined various metal oxides as charging catalyst including MnO_x/C[32] (≈4.2 V_{Li}), λ-MnO_2(≈4.0 V_{Li}),[27] α-MnO_2 nanowires(≈4.0 V_{Li}),[31] and Co_3O_4(≈3.9 V_{Li}).[39]

However, directly comparing the charge catalytic activities of different Li-O_2 cells with different catalysts is complicated due to the fact that the discharge capacities and the morphologies of the discharge products could vary significantly across different cells (i.e., different starting point for charge). Therefore, accessing the intrinsic OER or Li_2O_2-decomposition activity with controlled starting point is necessary for charging catalyst developments. However, unlike ORR, where the reactant (i.e., O_2) is dissolved in the liquid phase and can be controlled by the rotation speed, the intrinsic nonaqueous OER

activity cannot be probed by RDE due to the insufficient solubility of Li_2O_2 or Li_2O in the nonaqueous electrolytes.[114]

To systematically evaluate the OER activity of catalysts, we developed a model system that controls the quantity and the morphology of the reactant, e.g., Li_2O_2, to quantify the Li_2O_2-decomposition reaction rate and directly compare the OER activity across different materials. Here, we examine the effect of catalyzed (40%wt. Au/C or 40%wt. Pt/C) and pure Vulcan-XC72 carbon cathodes on the decomposition of Li_2O_2. In addition, we show that the results obtained from the electro-oxidation of Li_2O_2 are in good agreement with Li-O_2 cell measurements, reflecting the activity associated with electro-oxidation of Li_2O_2 on these catalysts. By applying insights obtained from the model system, we create platinum-gold (PtAu) nanoparticles and examine the discharge and charge activity of such particles supported on carbon in Li-O_2 cells. We demonstrate that the PtAu/C bifunctional catalyst significantly increase the round-trip efficiency (the ratio of discharge to charge voltage) of the rechargeable Li-O_2 batteries.

5.2 Experimental Session

Lithium Peroxide-Filled Composite Electrodes. The activity of Vulcan-XC72, 40%wt. Au/C, and 40%wt. Pt/C catalysts for electro-oxidation of Li_2O_2 (OER) was measured in argon-filled cells (Tomcell type TJ-AC) with lithium anode and Celgard 2500 separator. Kynar®-bonded cathodes with and without Li_2O_2 were prepared from ultrasonicated inks containing carbon or catalyst, poly vinylidene fluoride (Kynar® PVDF) dissolved in N-methyl pyrrolidone (<50 ppm H_2O, Alfa-Aesar), and ground Li_2O_2 (Aldrich 90%) for Li_2O_2-filled electrodes. Inks were coated onto aluminum foil (0.019 mm thick**,** McMaster), vacuum-dried at 70 ^oC, and cut (15 mm diameter). Cathode carbon loadings were within 0.85 ± 0.15 mg (0.48 ± 0.08 mg/$cm^2_{electrode}$) at a PVDF/carbon weight ratio of 3.6/1. The Li_2O_2/carbon weight ratio was 1/1, equating to an estimated charging capacity of 1050 mAh/g_{carbon} for $Li_2O_2 \leftrightarrow 2Li + O_2$ (considering 90% Li_2O_2 sample purity).

Testing of Electro-Oxidation of Li_2O_2. Potentiostatic tests were performed at 4.0 to 4.5 V_{Li} for 10 hours after initial 30 min rest following cell assembly. Net Li_2O_2 electro-oxidation currents were obtained by subtracting carbon-mass normalized currents of Li_2O_2-free electrodes from those filled with Li_2O_2. While Al current collectors were used Li-air cathodes previously,[103] some minor Al corrosion was reported to occur at 4.5 V in $LiClO_4$-based electrolytes (15 $\mu A/cm^2$).[155] We thus examined the background current densities from Li_2O_2-free electrodes, which were one to two orders of magnitude lower than those from Li_2O_2-filled electrodes measured at 4.5 V (>150 $\mu A/cm^2_{electrode}$ or >300 mA/g_{carbon}). This is in agreement with the observation that no apparent change for the Al current collectors was found after any measurements of electrodes without or with Li_2O_2.

Synthesis of PtAu Nanoparticles.[156] 0.25 mmol $HAuCl_4$ (Sigma-Alrich) and 0.25 mmol H_2PtCl_6 (Sigma-Alrich) were dissolved in 20 mL oleylamine (Sigma-Alrich) at 40 °C under an Ar blanket. The solution was then heated up to 160 °C and maintained at 160 °C for 2 h. PtAu particles were collected by adding 100 mL ethanol and following centrifugation. The as-prepared PtAu nanoparticles were dispersed then in non-polar solvents such as hexane and toluene.

Carbon Loading and Thermal Treatment. 150 mg Vulcan XC-72 (Premetek, USA) were pre-dispersed in 400 mL hexane (Sigma-Alrich) by sonicating in ice bath for 5h. As-prepared PtAu nanoparticles (~100mg) were dissolved in hexane and then added dropwise into the Vulcan solution under sonication in ice bath. The solution was further sonicated for 2 h and stirred overnight. The catalyst powders were collected by purging Ar (evaporating hexane) at room temperature and dried in vacuum for 24 hours. The PtAu/C catalyst was finally treated at 250 °C in dry air for 30min to remove surfactant yielding 40 wt.% PtAu/C, which is determined by thermogravimetric analysis (TGA).

Preparation of PtAu/C Catalyst Electrode for Cyclic Voltammogram. Electrodes with a Nafion®/carbon weight ratio of 0.5/1 were prepared by drop-casting ultrasonicated inks composed of carbon or catalyst, Nafion® dispersion (DE520, Ion-Power, USA), and 20 wt.% 2-propanol (Sigma-Aldrich) in de-ionized water (18.2 MΩ·cm, Millipore) onto the glassy carbon disk, yielding a carbon loading of 0.2 mg/mL.

Calculation of Particle Size Distribution of Carbon Supported PtAu Nanoparticles. The particle size distribution of PtAu nanoparticles was examined in a JEOL 2010F TEM operated at 200 kV with a point-to-point resolution of 0.19 nm. Nanoparticles were first immersed in ethanol and subsequently dispersed on a lacey carbon grid and dried in air for TEM observations. One hundred and thirty-six randomly selected nanoparticles from HRTEM images were used to produce particle size distributions of PtAu/C. For each distribution, the number-averaged diameter d_n was determined by $d_n = \frac{\sum_{i=1}^{n} d_i}{n}$ while the volume-surface-area-averaged diameter was calculated by $d_{v/a} = \frac{\sum_{i=1}^{n} d_i^3}{\sum_{i=1}^{n} d_i^2}$ where d_i is the diameter of individual particles. The specific surface area of nanoparticles based on the volume-surface-area-averaged diameter from TEM measurements was determined by $6(1000/(\rho_{pt} d_{v/a}))$.

Scanning Transmission Electron Microscope (STEM) Images of Carbon Supported PtAu Nanoparticles. The compositional distributions of Pt and Au of individual PtAu nanoparticles were examined by X- ray energy dispersive spectroscopy (EDS) in a JEOL 2010F TEM at room temperature using a beam voltage of 200 kV and INCA control software (Version 4.08, Oxford Instruments Analytical Limited). Pt $L_{\alpha 1}$ (~9.442 keV) and Au $L_{\alpha 1}$ (~9.674 keV) signals were used for composition quantification. The chemical compositions of individual PtAu nanoparticles were determined from signals collected for 275 s with a scanning beam of 2 nm in diameter, which provided sufficient signal-noise ratios for quantification of Pt and Au atomic fractions. Errors in the Pt and Au atomic fractions in the analysis of each spectrum were generated by INCA, which were related to the standard deviation of X-ray signal counting.

Preparation of Air-Electrode for Li-O_2 Cell. Air-electrode with a Nafion®/carbon weight ratio of 0.5/1 were prepared by coating ultrasonicated inks composed of catalyst, lithium-ion-exchanged Nafion® dispersion (Ion-Power, USA), and 2-propanol (Sigma-Aldrich) onto the separator (Celgard C480). The electrodes were air-drying at 20°C for about 20 minutes and subsequent vacuum-drying for 3 hours.

Cyclic Voltammetry. As-prepared electrodes were then mounted to a rotator (Pine Instruments) and immersed into 0.5 M H_2SO_4 (Fluka). A spiral Pt wire was employed as the counter electrode, and a saturated calomel electrode (SCE, Analytical Sensor, Inc.) was used as the reference electrode. The potential of SCE with respect to the reversible hydrogen electrode (RHE) was calibrated from rotating disk electrode measurements of hydrogen oxidation. All the potential values reported in this paper refer to that of the RHE (V_{RHE}). After the electrolyte was bubbled with argon (Ar) for half an hour, the working electrodes were scanned between 0.02 and 1.7 V_{RHE} at a sweep rate of 50 mV/s for 3 times. Steady-state cyclic voltammograms were recorded at 50 mV/s in the same potential range at room temperature.

Determination of Electrochemical Surface Area (ESA) of Pt and Au. The determination of Pt surface area was done as follows: 1) integrating the net (i.e., with double-layer capacitance subtraction) charge formation of hydrogen adsorption region (negative-going scan from 0.4 V_{RHE} – 0.02 V_{RHE}) and hydrogen desorption region (positive-going scan from 0.02 V_{RHE} – 0.4 V_{RHE}). Double-layer capacitance background was assumed by linear-extension from the double-layer region; 2) Average the net charge from hydrogen adsorption and desorption; 3) the averaged net charge (μC) was then divided by the most accepted converting factor for Pt surface,[1] 210 μC/cm^2, and yield the ESA of Pt. The determination of Au surface area was done as follows: 1) integrating the net (i.e., with double-layer capacitance subtraction) charge formation of AuO or $Au(OH)_2$ (negative-going scan from 1.34 V_{RHE} – 0.92 V_{RHE}). Double-layer capacitance background was assumed by linear-extension from the double-layer region; 2) the net charge (μC) was then divided by the reported converting factor (i.e., 350 μC/cm^2 for the potential window being 1.7 V_{RHE})[2] yielding the ESA of Au. Two experiments were conducted and the results show that ESA for Pt is (23 ± 4) m^2/g_{PtAu} and for Au is (15 ± 1) m^2/g_{PtAu}. The specific ESA of PtAu/C is (38 ± 4) m^2/g_{PtAu}. The surface atomic ratio of Pt/Au is (60 ± 2%)/(40 ± 2%).

Li-O_2 Cell Assembling Configurations and Testing Conditions. Li-O_2 cell tests were conducted at room temperature in 1 M $LiClO_4$ in PC:DME (1:2 v/v) electrolyte, prepared from $LiClO_4$, propylene carbonate (PC), and 1,2-dimethoxyethane (DME) from Sigma-

Aldrich (all <30 ppm H_2O). The Li-O_2 battery configuration used in this study consists of a lithium foil (15 mm diameter), two pieces of Celgard separator (C480) (17 mm diameter) and a Nafion®-bonded cathode (12.7 mm diameter) coated on a Celgard C480 using either pure Vulcan XC-72 carbon, 40%wt. PtAu/C (Vulcan), 40%wt. Au/C (Vulcan) (Premetek, USA), or 40%wt. Pt/C (Vulcan) (Premetek, USA). Li-O_2 cells were assembled in the following order: 1) placing a lithium foil onto the cell's stainless steel current collector, 2) adding 10 µl electrolyte, 3) placing two pieces of the separator onto the lithium foil, 4) adding 10 µl electrolyte, 5) placing the cathode-coated separator onto the separator, 6) adding on top a cathode current collector (316 stainless steel mesh and spring), and, 7) purging the cell with PC/DME-saturated oxygen for 10 minutes. Afterwards, cells were sealed and tested galvanostatically (Solartron 1470) at various rate (50mA/g_{carbon} – 250 mA/g_{carbon}) with a low voltage limit of 2.0 V_{Li} and upper limits of 4.5 V_{Li} (pure carbon, subsequently hold at 4.5 V_{Li} for 5 hours before the next discharge), 4.4 V_{Li} (Au/C, no holding) and 4.0 V_{Li} (PtAu/C and Pt/C, no holding) to avoid electrolyte decomposition. In addition, the charging step in cycling testing at 100 mA/g_{carbon} was designed to be terminated when the high cut-off voltage was reached or after a maximum of 20 hours (=2000 mAh/g_{carbon}).

5.3 Results and Discussion

5.3.1 Quantitative Determination of Li_2O_2-Oxidation Activity

The activity for electro-oxidation of Li_2O_2 on Vulcan carbon, Au/C and Pt/C was measured by potentiostatic charging of Li_2O_2-filled cathodes. For carbon cathodes, net currents of ≈150 mA/g_{carbon} were obtained at 4.2 V_{Li} (Figure 5-1a) and the current was negligible at 4.0 V_{Li}, which is consistent with Li-O_2 cell data reported in literature.[39,138] In addition, the accumulated charge agrees, within experimental error, with the estimated charging capacity (see Experimental Session). The same was observed for galvanostatically charged Li_2O_2-filled Super-S carbon-based cathodes,[103] even though their charging voltage (≈4.5 V_{Li} at 10 mA/g_{carbon}) is substantially higher than that of the Vulcan-based cathodes shown in Figure 5-1a (4.2 V_{Li} at ≈100 mA/g_{carbon}), probably due to the faster reaction rates per

gram of carbon obtained for Vulcan with higher surface area (240 m^2/g) than Super S (40 m^2/g). While it is clear that the charging current density must decrease with increasing time (specific capacity) as Li_2O_2 is being depleted by oxidation (Figure 5-1a), the origin of the initial increase in current density is not understood, which might be related to the increase of available surface reaction sites during the initial stages of Li_2O_2 oxidation. At 4.0 V_{Li}, the Li_2O_2 electro-oxidation current density was found the highest for Pt/C, then Au/C and lowest for carbon, which mirrors the trend in the charging voltage of Li-O_2 cells (Figure 5-1b). It is interesting to note that the Pt/C cathode can provide a charging capacity >200 mA/g_{carbon} at 4.0 V_{Li}, which is more active for electro-oxidation of Li_2O_2 than manganese oxide having 10 mA/g_{carbon} at ≈4.3 V_{Li} in similar experiments.[103] The intrinsic Li_2O_2 electro-oxidation activities on Au/C and Pt/C were obtained by normalizing current densities to the metal surface area in the cathode, as shown in Figure 5-1c. It shows that Pt/C has slightly higher Li_2O_2 decomposition activity than Au/C.

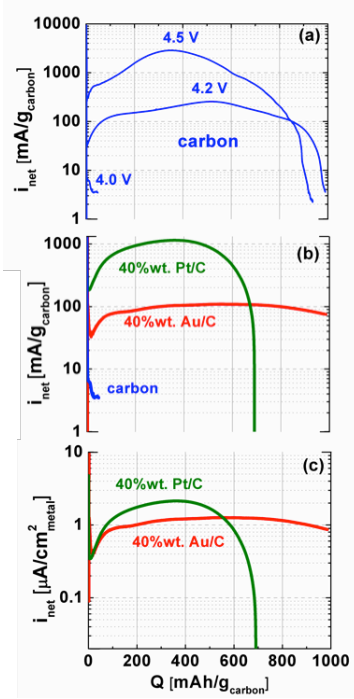

Figure 5-1. Net Li_2O_2 decomposition currents, i_{net}, versus integrated charge of Li_2O_2–filled cathodes under argon: (a) carbon cathodes at various potentials; (b) carbon, 40%wt. Au/C, and 40%wt. Pt/C at 4.0 V_{Li}; (c) same as (b), but currents normalized to Pt and Au surface areas.

5.3.2 PtAu Nanoparticles as An Electrocatalyst for Rechargeable Li-Air Batteries

Characterization of PtAu Nanoparticles. PtAu nanoparticles[157] were synthesized by reducing $HAuCl_4$ and H_2PtCl_6 in oleylamine[156] (see Experimental Session) and then loaded onto Vulcan carbon (XC-72) to yield 40 wt% PtAu/C. The catalyst was thermally treated at 250 °C in dry air to remove the nanoparticle surfactant before battery assembly (see Experimental Session for details). Transmission electron microscopy (TEM) shows that PtAu nanoparticles are uniformly distributed on carbon (Figure 5-2), having a number-averaged particle size of 6.8 ± 1.4 nm (Figure 5-3, see Experimental Session for details) and a volume-averaged diameter of 7.3 nm (yielding a dispersion of 40 m^2/g_{PtAu}). In addition, X-ray diffraction data of PtAu/C indicate that Pt and Au atoms form a solid-solution (Figure 5-4), which is in agreement with previous reported powder diffraction file (PDF#01-074-5396) database for $Pt_{0.5}Au_{0.5}$.[158] This is further supported by energy-dispersive X-ray (EDX) mapping by scanning transmission electron microscopy revealing Pt and Au atoms distributed uniformly within individual particles (Figure 5-5).

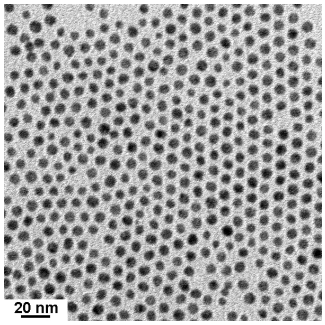

Figure 5-2. A representative TEM image of as-prepared PtAu nanoparticles.

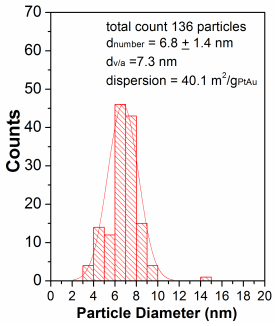

Figure 5-3. Particle size histogram of carbon supported PtAu nanoparticles obtained from HRTEM images.

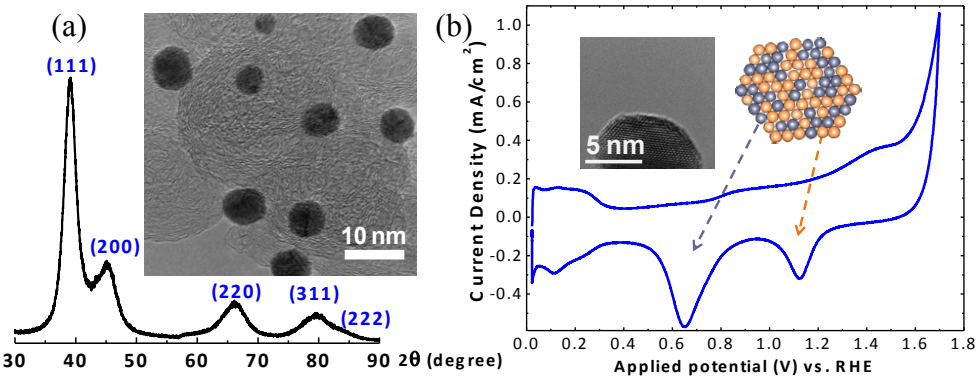

Figure 5-4. (a) A representative TEM image (top right) and X-ray diffraction data of PtAu/C. (b) Cyclic Voltammograms of PtAu/C collected in Ar-saturated 0.5 M H_2SO_4 between 0.05 V-1.7 V vs. RHE (room temperature and 50 mV/s). Inset: (Left) HRTEM image of PtAu/C. (Right) Schematic representation of PtAu with arrows indicating the CV signatures for Pt (gray) and Au (yellow).

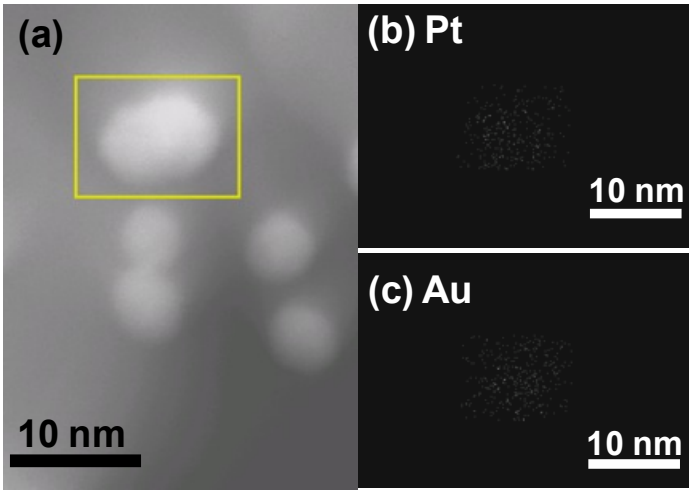

Figure 5-5. (a) High-angle annular dark-field (HAADF) image of PtAu nanoparticles. The image was taken with JEOL 2010F TEM in STEM mode. (b) and (c) Energy-dispersive X-ray (EDX) mapping of the region in yellow rectangular of (a), where (b) is Pt disctribution quantified from Pt $L_{\alpha 1}$-line, and (c) is Au distribution quantified from Au $L_{\alpha 1}$-line.

As electrocatalytic activity is dominated by nanoparticle surface compositions, we use well-established CV methods[143,159] to obtain the electrochemical

surface area (ESA) of Pt and Au of PtAu nanoparticles, from which surface atomic fractions can be estimated. The ESA of Pt and Au were estimated from the charge associated with hydrogen adsorption/desorption on Pt and the oxide desorption on Au from CV data in Figure 5-4b, respectively. The specific ESA is 38 ± 4 m^2/g_{PtAu}, which is in reasonable agreement with the dispersion estimated from TEM data. Surface atomic ratio of Pt/Au was found to be (60 ± 2%)/(40 ± 2%) which is in good agreement with the average particle composition obtained from EDX, as shown in Figure 5-5 (Pt 56 ± 5% and Au 44 ± 5%) (see Experimental Session for details).

The Electrocatalytic Activity of PtAu/C for Discharge and Charge Reactions of Li-O_2 Batteries. The electrocatalytic activity of PtAu/C for discharge and charge was examined in Li-O_2 cells, which was compared with those of pure carbon (Vulcan XC-72), Pt/C and Au/C (Premetek, 40wt% on Vulcan XC-72). Cell configuration and the making of air electrodes were included in the Experimental Session. All air electrodes had very comparable carbon-loadings. Catalyzed-carbon catalysts (i.e., 40 wt% Pt/C, 40 wt% Au/C and 40 wt% PtAu/C) had carbon-loadings of 0.50 ± 0.02 mg. Pure carbon electrodes had carbon-loadings of 0.65 ± 0.11 mg over an area of 1.27 cm^2. The thicknesses for all the air electrodes were 14 μm ± 2 μm. As the metal volume fraction was negligible and the void volume fraction of catalyzed and non-catalyzed air electrodes was essentially the same,[33] all our air electrodes were expected to have similar void volume for Li_xO_2 storage, and thus similar specific capacities.

The discharge and charge voltages of Li-O_2 cells can be influenced greatly by PtAu nanoparticles used in the air electrode. While Li-O_2 cells of PtAu/C and pure carbon exhibited similar specific capacities (≈1200 mAh/g_{carbon}), air electrodes with PtAu/C was found to have a higher round-trip efficiency than that with carbon only, as shown in Figure 5-6a. During discharge, the discharge voltage of PtAu/C is consistently higher than pure carbon by ≈360 – 150 mV. During charge, the charge voltages of PtAu/C fell in the range from 3.4 V_{Li} to 3.8 V_{Li} (with an average of ≈3.6 V_{Li}), which is substantially lower (by 900 mV) than that of pure carbon (with an average voltage of ≈4.5 V_{Li}).

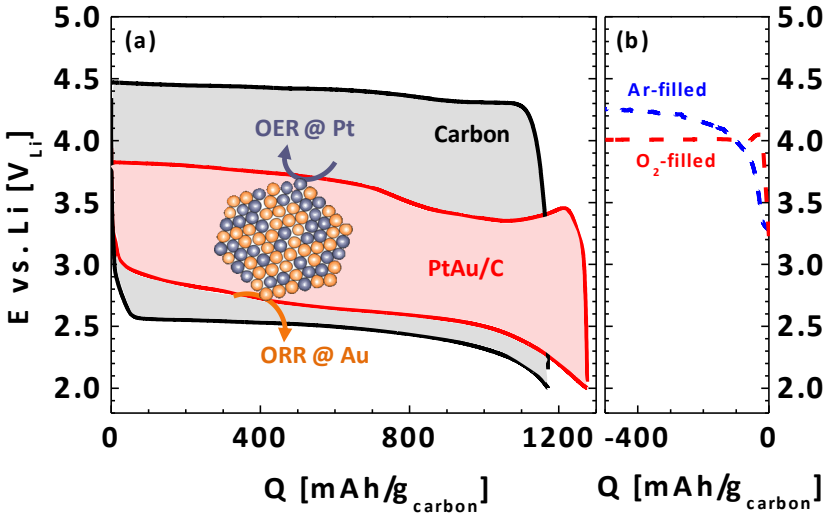

Figure 5-6. (a) Li-O_2 cell discharge/charge profiles of carbon (black) and PtAu/C (red) in the third cycle at 0.04 mA/cm$^2_{electrode}$ (100 mA/g_{carbon} for PtAu/C, 85 mA/g_{carbon} for carbon) (b) Background measurement during charging at 100 mA/g_{carbon} of an Ar and O_2-filled cell (charging first) for PtAu/C.

To verify that the charging current of voltages lower than 4 V_{Li} is not a result of electrolyte decomposition, cells were charged under both Ar and O_2. The charge associated with electrolyte decomposition on PtAu/C became significant only above 4.0 V_{Li} (on pure carbon and Au/C is ≥4.7 V_{Li}, Figure 5-6b),[102] proving that PtAu/C catalyzes the oxidation of lithium (per)oxide discharge products at voltages as low as 3.4 V_{Li}. The round-trip efficiency of the PtAu/C cathode in Li-O_2 cells was 73%, which is much improved relative to 57% found for the pure carbon cathode. Interestingly, the PtAu/C catalyst exhibits considerably lower charging voltages than MnO_x/C[32] (≈4.2 V_{Li}), λ-MnO_2,[27] α-MnO_2 nanotubes,[31] and Co_3O_4[39] (≈4.0 V_{Li}) at a comparable current density of 70 mA/g_{carbon}. Moreover, PtAu/C shows higher charging activity than pyrolyzed cobalt phthalocyanine supported on carbon reported previously,[21] where below 3.6 V_{Li}, PtAu/C has a charging capacity of ~500 mAh/g_{carbon} (at 0.04 mA/cm$^2_{electrode}$) while the cobalt-based catalyst delivers ≈60 mAh/g_{carbon} at similar conditions (0.05 mA/cm$^2_{electrode}$; rate in mA/g_{carbon} not reported).

In order to understand the roles of surface Pt and Au atoms of PtAu/C in catalyzing the reaction kinetics, first discharge and charge voltages of Li-O_2 cells with PtAu/C were compared with those with Pt/C and Au/C at the same rate, as shown in Figure 5-7a. The discharge voltages with PtAu/C are comparable to those with Au/C while charging voltages with PtAu/C are comparable to those with Pt/C. This result indicates that surface Pt and Au atoms on PtAu/C are responsible for discharge and charge reaction kinetics, respectively. Therefore, PtAu/C demonstrates bifunctional catalytic activity for discharge reaction and charge reaction in Li-O_2 cells. Interestingly, the charging voltages of PtAu/C became lower than Pt/C in subsequent cycles as shown in Figure 5-8, which were reproducible over multiple cells. The physical origin of the enhanced charging activity and lowered charging potentials of PtAu/C compared to Pt/C is not understood and will be investigated in future studies.

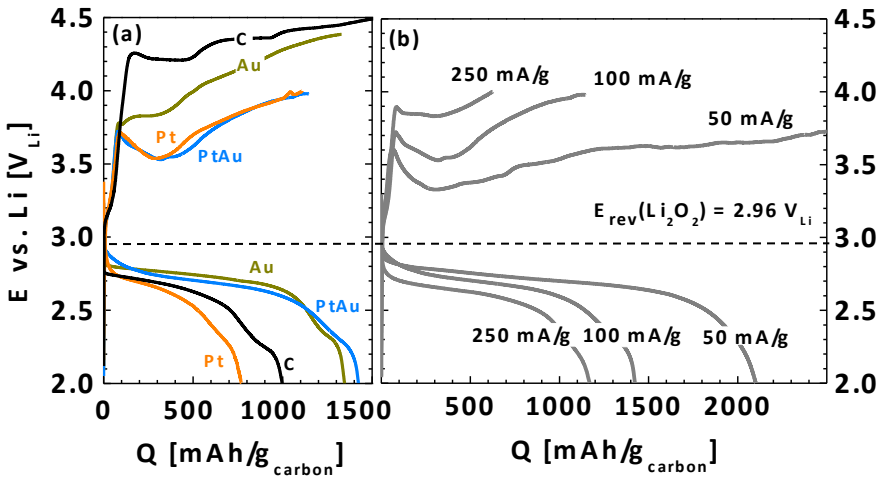

Figure 5-7. (a) Li-O_2 cell 1st discharge/charge profiles of carbon at 85 mA/g_{carbon}, Au/C, Pt/C, and PtAu/C at 100 mA/g_{carbon}. (b) Li-O_2 cell discharge/charge profiles (1st cycle) of PtAu/C at 50 mA/g_{carbon}, 100 mA/g_{carbon}, and 250 mA/g_{carbon}.

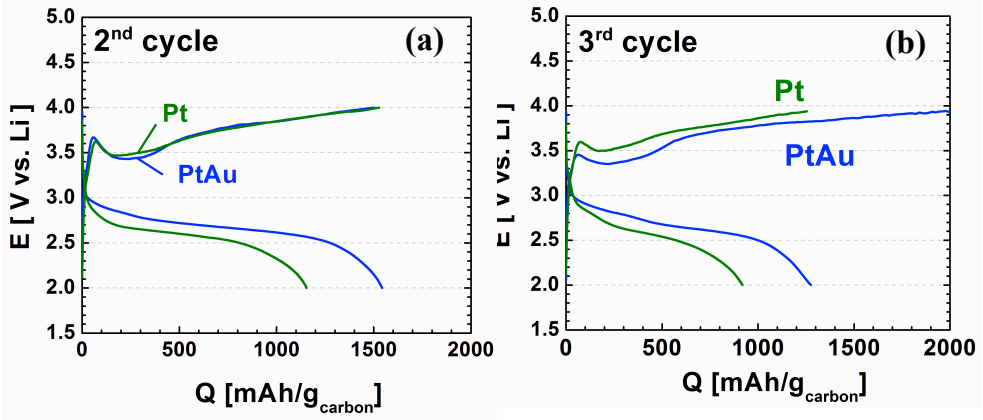

Figure 5-8. Li-O_2 cell (a) 2nd and (b) 3rd discharge/charge profiles of Pt/C, and PtAu/C at 100 mA/g_{carbon}.

We further examine the effect of current density on the discharge and charge voltages of Li-O_2 cells with PtAu/C. With decreasing current densities, the difference between discharge and charge voltages was further reduced considerably, as shown in Figure 5-7b. Remarkably, at 50 mA/g_{carbon}, Li-O_2 cells with PtAu/C can deliver ≈50% (≈1000 mAh/g_{carbon}) of the discharge capacity above 2.7 V_{Li} and ≈50% (≈1000 mAh/g_{carbon}) of the charge capacity below 3.5 V_{Li}, rendering a round-trip efficiency of ≈77%. Figure 5-9 shows the charging background measurement of PtAu/C cells under Ar and O_2-filled environment at 50 mA/g_{carbon}. The results reveal that the charge associated with electrolyte decomposition on PtAu/C became significant at voltages ≈ 4.0 V_{Li} at 50 mA/g_{carbon}.

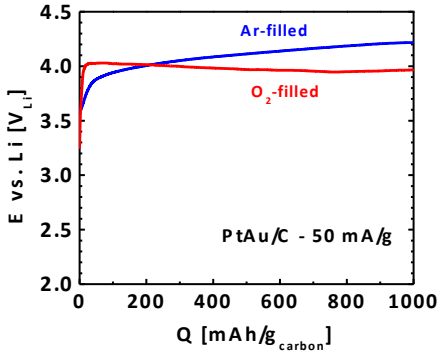

Figure 5-9. Background measurements during charging at 50 mA/g_{carbon} of an Ar and O_2-filled cell (charging first) for PtAu/C.

While it is not surprising to observe increased discharge capacity with decreasing current densities as reported in several previous studies,[27-29] it is interesting to note that charging voltages are lowered by a few hundreds of milli-volts with decreasing current densities by a factor of five, which cannot be explained simply by lowered surface kinetics overpotentials. It is believed that the natures of product formation/distribution could affect the reaction voltages, which requires further studies.

5.4 Conclusions

In this chapter, we have developed model systems by adding controlled quantities of Li_2O_2 into positive electrodes, enabling the evaluation of the intrinsic Li_2O_2 oxidation activity without changing the morphology or composition of the electrode. It is found that Pt/C has remarkable activity toward Li_2O_2 decomposition. With insights gained from the Li_2O_2-filled model system, we demonstrated that PtAu/C exhibits bifunctional catalytic activity, where it is hypothesized that surface Au and Pt atoms are primarily responsible for discharge and charge kinetics in Li-O_2 cells, respectively. To our knowledge, PtAu/C reported here demonstrates the lowest charging voltage and highest round-trip efficiency of Li-O_2 cells reported then.[21,27,31,39] This work shows that placing select atoms (such as Pt and Au) on nanoparticle surfaces can be a promising strategy to develop highly active bifunctional catalysts for Li-O_2 batteries.

Chapter 6. Conclusion and Perspective

Fundamental understanding of the electrochemical and chemical processes between electrode and electrolyte interfaces is key toward rational design for Li-storage. In this thesis, fundamental approaches involving electrochemical characterizations, advanced spectroscopic and microscopic techniques were used to probe the Li-ion and Li-O_2 reaction chemistries.

The first part of the thesis revealed the working mechanism of the "$AlPO_4$" surface coating and identified criteria for efficient electrode-electrolyte interfaces for Li-ion batteries. SEM, XRD and XPS were used to examine the changes in morphology, crystal structure and surface chemistry after cycling to high voltages (4.7 V_{Li}), respectively. The "$AlPO_4$" nanoparticles was found to promote the formation of Co-Al-O-F species on the $LiCoO_2$ particle surfaces. Such cobalt-containing oxyfluoride surface species are expected to protect the active materials from further undesired reactions with the electrolyte and prevent oxygen loss from the lattice. The hypothesis is further supported by the fact that simply adding Al_2O_3 powders to the $LiCoO_2$ electrode yields enhanced stability and promote the formation of cobalt-containing oxyfluoride surface species. This study (**Chapter 2**) identifies the roles of metal-containing oxyfluoride in improving the electrode stability and cell efficiency.

In order to develop high-energy rechargeable Li-O_2 battery as a viable energy storage technology, mechanistic understanding of the reaction kinetics, catalyst effects and reaction mechanism of the Li-O_2 batteries were investigated. First, a nonaqueous RDE configuration with well-defined GC electrode and high-surface-area carbon electrodes was developed to quantify the intrinsic ORR activity of the carbon surface. Results obtained via the RDE method were shown to be comparable to the discharge voltage of carbon electrode in the Li-O_2 cells (**Chapter 3**). In addition, the reaction order of the ORR with respect to oxygen partial pressure and the Tafel analysis suggest that the ORR on carbon first proceeds by a one-electron reduction to LiO_2 with the initial adsorption of oxygen being the rate-determining step.

To examine the catalyst effects on the ORR activity, well-defined bulk surfaces and high-surface-area catalysts were examined with the RDE configuration (**Chapter 4**). It is revealed that the ORR activity is in order of Pd > Pt > Ru ≈ Au > GC, exhibiting a volcano-type dependence as a function of the oxygen adsorption energy of the catalyst surface. This volcano dependence suggests that the oxygen adsorption energy of the catalyst can serve as the ORR activity descriptor for designing highly active ORR catalyst for Li-O_2 batteries. In addition, the application of Au nanoparticles was shown to significantly increase the rate capability of the Li-O_2 cells. It is found that the enhancement associated with the Au catalyst at low rates can be governed by the intrinsic ORR activity of catalyst surfaces. The enhancement observed at high rates may result in part from higher degree of structural defect in the discharge products, Li_2O_2, formed on the Au surfaces compared to that on the carbon, as suggested by XRD. The higher degree of structural defects and/or nonstoichiometry of Li_2O_2 formed on the Au/C may lead to faster solid-state Li diffusion and/or higher electronic conductivity during discharge, and thus enhances the rate capability of the Li-O_2 cells.

The catalyst effects on the charge reaction (OER), or Li_2O_2-decomposition reaction, were studied by potentiostatically oxidizing Li_2O_2-filled electrodes (**Chapter 5**). The model electrodes contain controlled amount and morphology of the commercially available Li_2O_2 with various catalysts. Remarkably, it is found that the electro-oxidation of Li_2O_2 can be significantly catalysed by the presence of Pt nanoparticles. We applied the insights obtained from the model systems to design bimetallic PtAu nanoparticles as bifunctional catalysts for Li-O_2 batteries. Interestingly, the PtAu/C catalyst exhibits comparable discharge profile to the Au/C and resembled the charge activity of the Pt/C catalyst, achieving a remarkable round-trip efficiency (~75%) for rechargeable Li-O_2 batteries.

Perspective. This thesis highlights the importance of surface chemistry in creating efficient oxide-electrolyte interfaces and identifies strong influences of metal catalysts on the nonaqueous Li^+-ORR and Li^+-OER kinetics. Extended from this thesis, the following research areas (Figure 6-1) can further reveal the reaction mechanisms, optimize the electrode structures, and develop cost-effective oxide catalysts for rechargeable Li-O_2

technology. First, in situ techniques that directly probe the reactions under operation conditions are expected to provide the most critical and important insights into the Li-O_2 reaction mechanisms and design principles. For example, in situ ambient pressure XPS can reveal the chemical nature of the Li-O_2 reaction products and correlations between reaction processes and reaction potentials. Such study will provide insights into the origins of the overpotentials for Li-O_2 batteries. In addition, in situ XRD can offer structural information of the reaction products during discharge and charge. This will reveal the role of the defect structure and nonstoichiometry of the reaction products on influencing the reaction overpotential. Furthermore, in situ microscopic characterizations can monitor morphological changes of the reaction products and the filling process in the electrode structures. Second, electrode structures including porosity, surface area, carbon (or other substrate materials) loading, and pore distribution, are important design parameters to maximize the specific capacity and cycle life of Li-O_2 batteries. Finally, the pronounced catalyst effects with precious metals identified in this thesis strongly motivates the search for active earth-abundant oxide materials (i.e., Mn, Fe-based) as cost-effective catalysts for rechargeable Li-O_2 batteries.

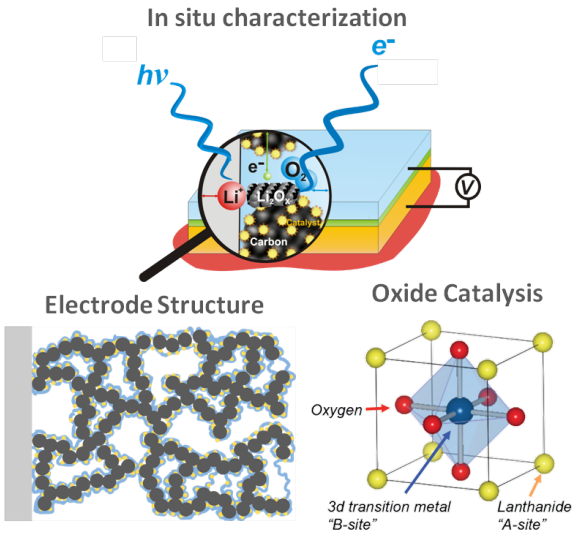

Figure 6-1. Future directions for developing Li-O_2 technologies: In situ spectroscopic and microscopic characterizations, design of electrode structures and oxide materials for O_2-electrocatalysis. Figure source of perovskite structure: Suntivich, J. et al., Nat. Chem. 3, 546-550, (2011)

References

1 Armand, M. & Tarascon, J.-M. Building better batteries. *Nature* **451**, 652-657, (2008).

2 Dunn, B., Kamath, H. & Tarascon, J.-M. Electrical Energy Storage for the Grid: A Battery of Choices. *Science* **334**, 928-935, (2011).

3 Marris, E. Energy: Upgrading the grid. *Nature* **454**, 570-573, (2008).

4 Schiermeier, Q., Tollefson, J., Scully, T., Witze, A. & Morton, O. Electricity without carbon. *Nature* **454**, 816-823, (2008).

5 Tollefson, J. Car industry: Charging Up the Future. *Nature* **456**, 436-440, (2008).

6 Electrical energy storage technology options. Report No. 1020676, (Electric Power Research Institute, Palo Alto, CA, 2010).

7 Dell, R. M. & Rand, D. A. J. Energy storage - a key technology for global energy sustainability. *J. Power Sources* **100**, 2-17, (2001).

8 Liu, C., Li, F., Ma, L. P. & Cheng, H. M. Advanced Materials for Energy Storage. *Adv. Mater.* **22**, E28-E62, (2010).

9 Tarascon, J.-M. & Armand, M. Issues and challenges facing rechargeable lithium batteries. *Nature* **414**, 359-367, (2001).

10 Linden, D., Reddy, T.B. (McGraw-Hill, New York, 2002).

11 Amatucci, G. G., Tarascon, J. M. & Klein, L. C. Cobalt dissolution in $LiCoO_2$-based non-aqueous rechargeable batteries. *Solid State Ion.* **83**, 167-173, (1996).

12 Appapillai, A. T., Mansour, A. N., Cho, J. & Shao-Horn, Y. Microstructure of $LiCoO_2$ with and without "$AlPO_4$" Nanoparticle Coating: A Combined STEM and XPS Studies. *Chem. Mat.* **19**, 5748-5757, (2007).

13 Jang, Y. I., Huang, B. Y., Wang, H. F., Sadoway, D. R. & Chiang, Y. M. Electrochemical cycling-induced spinel formation in high-charge-capacity orthorhombic $LiMnO_2$. *J. Electrochem. Soc.* **146**, 3217-3223, (1999).

14 Kim, Y. J., Cho, J. P., Kim, T. J. & Park, B. Suppression of cobalt dissolution from the $LiCoO_2$ cathodes with various metal-oxide coatings. *J. Electrochem. Soc.* **150**, A1723-A1725, (2003).

15 Oh, S., Lee, J. K., Byun, D., Cho, W. I. & Cho, B. W. Effect of Al_2O_3 coating on electrochemical performance of $LiCoO_2$ as cathode materials for secondary lithium batteries. *J. Power Sources* **132**, 249-255, (2004).

16 Sun, Y. K., Cho, S. W., Myung, S. T., Amine, K. & Prakash, J. Effect of AlF_3 coating amount on high voltage cycling performance of $LiCoO_2$. *Electrochim. Acta* **53**, 1013-1019, (2007).

17 Cho, J. Correlation between $AlPO_4$ nanoparticle coating thickness on $LiCoO_2$ cathode and thermal stability. *Electrochim. Acta* **48**, 2807-2811, (2003).

18 Cho, J., Kim, Y. W., Kim, B., Lee, J. G. & Park, B. A breakthrough in the safety of lithium secondary batteries by coating the cathode material with $AlPO_4$ nanoparticles. *Angew. Chem.-Int. Edit.* **42**, 1618-1621, (2003).

19 Horiba, T., Maeshima, T., Matsumura, T., Koseki, M., Arai, J. & Muranaka, Y. Applications of high power density lithium ion batteries. *J. Power Sources* **146**, 107-110, (2005).

20 Snyder, K. *DOE Merit Review : United States Advanced Battery Consortium (http ://www1.eere.energy.gov/vehiclesandfuels/pdfs/merit_review_2009/energy_storage/es_03_snyder.pdf)* 2009).
21 Abraham, K. M. & Jiang, Z. A polymer electrolyte-based rechargeable lithium/oxygen battery. *J. Electrochem. Soc.* **143**, 1-5, (1996).
22 Bruce, P. G., Freunberger, S. A., Hardwick, L. J. & Tarascon, J.-M. Li-O_2 and Li-S batteries with high energy storage. *Nat. Mater.* **11**, 19-29, (2012).
23 Beattie, S. D., Manolescu, D. M. & Blair, S. L. High-Capacity Lithium-Air Cathodes. *J. Electrochem. Soc.* **156**, A44-A47, (2009).
24 Abraham, K. M. A Brief History of Non-aqueous Metal-Air Batteries. *ECS Transactions* **3**, 67-71, (2008).
25 Chase, M. W., Jr. in *Journal of physical and chemical reference data, Monograph 9* (1998).
26 Hummelshoj, J. S., Blomqvist, J., Datta, S., Vegge, T., Rossmeisl, J., Thygesen, K. S., Luntz, A. C., Jacobsen, K. W. & Norskov, J. K. Communications: Elementary oxygen electrode reactions in the aprotic Li-air battery. *J. Chem. Phys.* **132**, 071101, (2010).
27 Read, J. Characterization of the lithium/oxygen organic electrolyte battery. *J. Electrochem. Soc.* **149**, A1190-A1195, (2002).
28 Read, J., Mutolo, K., Ervin, M., Behl, W., Wolfenstine, J., Driedger, A. & Foster, D. Oxygen transport properties of organic electrolytes and performance of lithium/oxygen battery. *J. Electrochem. Soc.* **150**, A1351-A1356, (2003).
29 Sandhu, S. S., Fellner, J. P. & Brutchen, G. W. Diffusion-limited model for a lithium/air battery with an organic electrolyte. *J. Power Sources* **164**, 365-371, (2007).
30 Kuboki, T., Okuyama, T., Ohsaki, T. & Takami, N. Lithium-air batteries using hydrophobic room temperature ionic liquid electrolyte. *J. Power Sources* **146**, 766-769, (2005).
31 Debart, A., Paterson, A. J., Bao, J. & Bruce, P. G. alpha-MnO_2 nanowires: A catalyst for the O-2 electrode in rechargeable lithium batteries. *Angew. Chem.-Int. Edit.* **47**, 4521-4524, (2008).
32 Cheng, H. & Scott, K. Carbon-supported manganese oxide nanocatalysts for rechargeable lithium-air batteries. *J. Power Sources* **195**, 1370-1374, (2010).
33 Gu, W., Baker, D. R., Liu, Y. & Gasteiger, H. A. in *Handbook of Fuel Cells – Fundamentals, Technology and Applications* Vol. 6 (eds W. Vielstich, Hubert A. Gasteiger, & H. Yokokawa) 631-657 (John Wiley & Sons 2009).
34 Thompson, E. L., Jorne, J., Gu, W. B. & Gasteiger, H. A. PEM fuel cell operation at -20 degrees C. I. Electrode and membrane water (charge) storage. *J. Electrochem. Soc.* **155**, B625-B634, (2008).
35 Zhang, S. S., Foster, D. & Read, J. Discharge characteristic of a non-aqueous electrolyte Li/O-2 battery. *J. Power Sources* **195**, 1235-1240, (2010).
36 Mizuno, F., Nakanishi, S., Kotani, Y., Yokoishi, S. & Iba, H. Rechargeable Li-Air Batteries with Carbonate-Based Liquid Electrolytes. *Electrochemistry* **78**, 403-405, (2010).
37 Zhang, G. Q., Zheng, J. P., Liang, R., Zhang, C., Wang, B., Hendrickson, M. & Plichta, E. J. Lithium-Air Batteries Using SWNT/CNF Buckypapers as Air Electrodes. *J. Electrochem. Soc.* **157**, A953-A956, (2010).

38 Girishkumar, G., McCloskey, B., Luntz, A. C., Swanson, S. & Wilcke, W. Lithium - Air Battery: Promise and Challenges. *J. Phys. Chem. Lett.* **1**, 2193-2203, (2010).
39 Debart, A., Bao, J., Armstrong, G. & Bruce, P. G. An O_2 cathode for rechargeable lithium batteries: The effect of a catalyst. *J. Power Sources* **174**, 1177-1182, (2007).
40 Fey, G. T. K., Lu, C. Z., Huang, J. D., Kumar, T. P. & Chang, Y. C. Nanoparticulate coatings for enhanced cyclability of $LiCoO_2$ cathodes. *J. Power Sources* **146**, 65-70, (2005).
41 Lee, J. G., Kim, B., Cho, J., Kim, Y. W. & Park, B. Effect of $AlPO_4$-nanoparticle coating concentration on high-cutoff-voltage electrochemical performances in $LiCoO_2$. *J. Electrochem. Soc.* **151**, A801-A805, (2004).
42 Kim, B., Lee, J. G., Choi, M., Cho, J. & Park, B. Correlation between local strain and cycle-life performance of $AlPO_4$-coated $LiCoO_2$ cathodes. *J. Power Sources* **126**, 190-192, (2004).
43 Cho, J., Lee, J. G., Kim, B., Kim, T. G., Kim, J. & Park, B. Control of $AlPO_4$-nanoparticle coating on $LiCoO_2$ by using water or ethanol. *Electrochim Acta* **50**, 4182-4187, (2005).
44 Cho, J., Kim, T. G., Kim, C., Lee, J. G., Kim, Y. W. & Park, B. Comparison of Al_2O_3- and $AlPO_4$-coated $LiCoO_2$ cathode materials for a Li-ion cell. *J. Power Sources* **146**, 58-64, (2005).
45 Cho, J. P., Kim, B., Lee, J. G., Kim, Y. W. & Park, B. Annealing-temperature effect on various cutoff-voltage electrochemical performances in $AlPO_4$-Nanoparticle-Coated $LiCoO_2$. *J. Electrochem. Soc.* **152**, A32-A36, (2005).
46 Kim, J., Noh, M., Cho, J., Kim, H. & Kim, K. B. Controlled nanoparticle metal phosphates (metal = Al, Fe, Ce, and Sr) coatings on $LiCoO_2$ cathode materials. *J Electrochem Soc* **152**, A1142-A1148, (2005).
47 Cho, J. P. & Park, B. Preparation and electrochemical/thermal properties of $LiNi_{0.74}Co_{0.26}O_2$ cathode material. *J. Power Sources* **92**, 35-39, (2001).
48 Cho, J., Kim, Y. J. & Park, B. $LiCoO_2$ cathode material that does not show a phase transition from hexagonal to monoclinic phase. *J Electrochem Soc* **148**, A1110-A1115, (2001).
49 Fey, G. T. K., Weng, Z. X., Chen, J. G., Lu, C. Z., Kumar, T. P., Naik, S. P., Chiang, A. S. T., Lee, D. C. & Lin, J. R. Preformed boehmite nanoparticles as coating materials for long-cycling $LiCoO_2$. *J. Appl. Electrochem.* **34**, 715-722, (2004).
50 Fey, G. T.-K., Yang, H.-Z., Prem Kumar, T., Naik, S. P., Chiang, A. S. T., Lee, D.-C. & Lin, J.-R. A simple mechano-thermal coating process for improved lithium battery cathode materials. *J. Power Sources* **132**, 172-180, (2004).
51 Chen, Z. H. & Dahn, J. R. Improving the capacity retention of $LiCoO_2$ cycled to 4.5 V by heat-treatment. *Electrochem. Solid State Lett.* **7**, A11-A14, (2004).
52 Bai, Y., Liu, N., Liu, J. Y., Wang, Z. X. & Chen, L. Q. Coating material-induced acidic electrolyte improves $LiCoO_2$ performances. *Electrochem. Solid State Lett.* **9**, A552-A556, (2006).
53 Myung, S. T., Izumi, K., Komaba, S., Sun, Y. K., Yashiro, H. & Kumagai, N. Role of alumina coating on Li-Ni-Co-Mn-O particles as positive electrode material for lithium-ion batteries. *Chem. Mat.* **17**, 3695-3704, (2005).

54 Kim, J. S., Johnson, C. S., Vaughey, J. T., Hackney, S. A., Walz, K. A., Zeltner, W. A., Anderson, M. A. & Thackeray, M. M. The electrochemical stability of spinel electrodes coated with ZrO_2, Al_2O_3, and SiO_2 from colloidal suspensions. *J. Electrochem. Soc.* **151**, A1755-A1761, (2004).

55 Aurbach, D., Markovsky, B., Rodkin, A., Levi, E., Cohen, Y. S., Kim, H. J. & Schmidt, M. On the capacity fading of $LiCoO_2$ intercalation electrodes: the effect of cycling, storage, temperature, and surface film forming additives. *Electrochim. Acta* **47**, 4291-4306, (2002).

56 Sun, Y. K., Lee, Y. S., Yoshio, M. & Amine, K. Synthesis and Electrochemical Properties of ZnO-Coated $LiNi_{0.5}Mn_{1.5}O_4$ Spinel as 5 V Cathode Material for Lithium Secondary Batteries. *Electrochem. Solid State Lett.* **5**, A99-A102, (2002).

57 Liu, J. Y., Liu, N., Liu, D. T., Bai, Y., Shi, L. H., Wang, Z. X., Chen, L. Q., Hennige, V. & Schuch, A. Improving the performances of $LiCoO_2$ cathode materials by soaking nano-alumina in commercial electrolyte. *J. Electrochem. Soc.* **154**, A55-A63, (2007).

58 Bai, Y., Yin, Y. F., Liu, N., Guo, B. K., Shi, H., Liu, J. Y., Wang, Z. X. & Chen, L. Q. New concept of surface modification to $LiCoO_2$. *J. Power Sources* **174**, 328-334, (2007).

59 Park, S. B., Shin, H. C., Lee, W.-G., Cho, W. I. & Jang, H. Improvement of capacity fading resistance of $LiMn_2O_4$ by amphoteric oxides. *J. Power Sources* **180**, 597-601, (2008).

60 Aurbach, D., Markovsky, B., Levi, M. D., Levi, E., Schechter, A., Moshkovich, M. & Cohen, Y. New insights into the interactions between electrode materials and electrolyte solutions for advanced nonaqueous batteries. *J. Power Sources* **82**, 95-111, (1999).

61 Aurbach, D. Review of selected electrode-solution interactions which determine the performance of Li and Li ion batteries. *J. Power Sources* **89**, 206-218, (2000).

62 Aurbach, D., Gamolsky, K., Markovsky, B., Salitra, G., Gofer, Y., Heider, U., Oesten, R. & Schmidt, M. The study of surface phenomena related to electrochemical lithium intercalation into Li_xMO_y host materials (M = Ni, Mn). *J. Electrochem. Soc.* **147**, 1322-1331, (2000).

63 Aurbach, D. Electrode-solution interactions in Li-ion batteries: a short summary and new insights. *J. Power Sources* **119**, 497-503, (2003).

64 Aurbach, D., Talyosef, Y., Markovsky, B., Markevich, E., Zinigrad, E., Asraf, L., Gnanaraj, J. S. & Kim, H. J. Design of electrolyte solutions for Li and Li-ion batteries: a review. *Electrochim. Acta* **50**, 247-254, (2004).

65 Aurbach, D., Markovsky, B., Salitra, G., Markevich, E., Talyossef, Y., Koltypin, M., Nazar, L., Ellis, B. & Kovacheva, D. Review on electrode-electrolyte solution interactions, related to cathode materials for Li-ion batteries. *J. Power Sources* **165**, 491-499, (2007).

66 Verdier, S., El Ouatani, L., Dedryvere, R., Bonhomme, F., Biensan, P. & Gonbeau, D. XPS study on Al_2O_3- and $AlPO_4$-coated $LiCoO_2$ cathode material for high-capacity li ion batteries. *J. Electrochem. Soc.* **154**, A1088-A1099, (2007).

67 Nishibori, E., Takata, M., Kato, K., Sakata, M., Kubota, Y., Aoyagi, S., Kuroiwa, Y., Yamakata, M. & Ikeda, N. The large Debye-Scherrer camera installed at SPring-8

BL02B2 for charge density studies. *Nucl. Instrum. Methods Phys. Res. Sect. A-Accel. Spectrom. Dect. Assoc. Equip.* **467-468**, 1045-1048, (2001).

68 Rodríguez-Carvajal, J. Recent advances in magnetic structure determination by neutron powder diffraction. *Physica B* **192**, 55-69, (1993).

69 Briggs, D. & Grant, J. T. (IM Publications and SurfaceSpectra Limited., Manchester, 2003).

70 N. Ikeo, Y. I., N. Nimura, M. Sigematsu, T. Tazawa, S. Matsumoto, K. Kojima, Y. Nagasawa. *Handbook of X-ray Photoelectron Spectroscopy*. (JEOL, 1991).

71 Menetrier, M., Carlier, D., Blangero, M. & Delmas, C. On "Really" stoichiometric $LiCoO_2$. *Electrochem. Solid State Lett.* **11**, A179-A182, (2008).

72 Menetrier, M., Saadoune, I., Levasseur, S. & Delmas, C. The insulator-metal transition upon lithium deintercalation from $LiCoO_2$: electronic properties and ^{7}Li NMR study. *J. Mater. Chem.* **9**, 1135-1140, (1999).

73 Ohzuku, T. & Ueda, A. Solid-State Redox Reactions of $LiCoO_2$ (R(3)over-Bar-M) for 4 Volt Secondary Lithium Cells. *J Electrochem Soc* **141**, 2972-2977, (1994).

74 Reimers, J. N. & Dahn, J. R. Electrochemical and Insitu X-ray-Diffraction Studies of Lithium Intercalation in Li_xCoO_2. *J. Electrochem. Soc.* **139**, 2091-2097, (1992).

75 Levasseur, S., Menetrier, M., Suard, E. & Delmas, C. Evidence for structural defects in non-stoichiometric HT-$LiCoO_2$: electrochemical, electronic properties and ^{7}Li NMR studies. *Sol. St. Ionics* **128**, 11-24, (2000).

76 Larcher, D., Palacin, M. R., Amatucci, G. G. & Tarascon, J.-M. Electrochemically active $LiCoO_2$ and $LiNiO_2$ made by cationic exchange under hydrothermal conditions. *J. Electrochem. Soc.* **144**, 408-417, (1997).

77 Benedek, R., Thackeray, M. M. & van de Walle, A. Free energy for protonation reaction in lithium-ion battery cathode materials. *Chem. Mat.* **20**, 5485-5490, (2008).

78 Butel, M., Gautier, L. & Delmas, C. Cobalt oxyhydroxides obtained by 'chimie douce' reactions: structure and electronic conductivity properties. *Solid State Ion.* **122**, 271-284, (1999).

79 Briggs, D. & Grant, J. T. 49 (IM Publications and SurfaceSpectra Limited., Manchester, 2003).

80 Ago, H., Kugler, T., Cacialli, F., Salaneck, W. R., Shaffer, M. S. P., Windle, A. H. & Friend, R. H. Work functions and surface functional groups of multiwall carbon nanotubes. *J. Phys. Chem. B* **103**, 8116-8121, (1999).

81 Kozlowski, C. & Sherwood, P. M. A. X-ray photoelectron-spectroscopic studies of carbon-fibre surfaces .5. the effect of PH on surface oxidation. *J. Chem. Soc., Faraday Trans. I* **81**, 2745-2756, (1985).

82 Clemencon, A., Appapillai, A. T., Kumar, S. & Shao-Horn, Y. Atomic force microscopy studies of surface and dimensional changes in Li_xCoO_2 crystals during lithium de-intercalation. *Electrochim. Acta* **52**, 4572-4580, (2007).

83 Dedryvere, R., Gireaud, L., Grugeon, S., Laruelle, S., Tarascon, J. M. & Gonbeau, D. Characterization of Lithium Alkyl Carbonates by X-ray Photoelectron Spectroscopy: Experimental and Theoretical Study. *J. Phys. Chem. B* **109**, 15868-15875, (2005).

84 Dupin, J. C., Gonbeau, D., Benqlilou-Moudden, H., Vinatier, P. & Levasseur, A. XPS analysis of new lithium cobalt oxide thin-films before and after lithium deintercalation. *Thin Solid Films* **384**, 23-32, (2001).

85 Hagelin-Weaver, H. A. E., Hoflund, G. B., Minahan, D. M. & Salaita, G. N. Electron energy loss spectroscopic investigation of Co metal, CoO, and Co3O4 before and after Ar+ bombardment. *Appl. Surf. Sci.* **235**, 420-448, (2004).

86 Markovsky, B., Rodkin, A., Salitra, G., Talyosef, Y., Aurbach, D. & Kim, H. J. The impact of Co^{2+} ions in solutions on the performance of $LiCoO_2$, Li, and lithiated graphite electrodes. *J. Electrochem. Soc.* **151**, A1068-A1076, (2004).

87 Daheron, L., Dedryvere, R., Martinez, H., Menetrier, M., Denage, C., Delmas, C. & Gonbeau, D. Electron transfer mechanisms upon lithium deintercalation from $LiCoO_2$ to CoO_2 investigated by XPS. *Chem. Mat.* **20**, 583-590, (2008).

88 Van Elp, J., Wieland, J. L., Eskes, H., Kuiper, P., Sawatzky, G. A., de Groot, F. M. F. & Turner, T. S. Electronic structure of CoO, Li-doped CoO, and $LiCoO_2$. *Phys. Rev. B* **44**, 6090, (1991).

89 Edström, K., Gustafsson, T. & Thomas, J. O. The cathode-electrolyte interface in the Li-ion battery. *Electrochim. Acta* **50**, 397-403, (2004).

90 Dupin, J. C., Gonbeau, D., Martin-Litas, I., Vinatier, P. & Levasseur, A. Lithium intercalation/deintercalation in transition metal oxides investigated by X-ray photoelectron spectroscopy. *J. Elec. Spectr. Rel. Phenom.* **120**, 55-65, (2001).

91 Alcantara, R., Ortiz, G. F., Lavela, P., Tirado, J. L., Jaegermann, W. & Thissen, A. Rotor blade grinding and re-annealing of $LiCoO_2$: SEM, XPS, EIS and electrochemical study. *J. Electroanal. Chem.* **584**, 147-156, (2005).

92 Zielke, U., Hüttinger, K. J. & Hoffman, W. P. Surface-oxidized carbon fibers: I. Surface structure and chemistry. *Carbon* **34**, 983-998, (1996).

93 Dupin, J.-C., Gonbeau, D., Vinatier, P. & Levasseur, A. Systematic XPS studies of metal oxides, hydroxides and peroxides. *Phys. Chem. Chem. Phys.* **2**, 1319-1324, (2000).

94 Liu, H. S., Zhang, Z. R., Gong, Z. L. & Yang, Y. Origin of deterioration for $LiNiO_2$ cathode material during storage in air. *Electrochem. Solid State Lett.* **7**, A190-A193, (2004).

95 Bryngelsson, H., Stjerndahl, M., Gustafsson, T. & Edstrom, K. How dynamic is the SEI? *J. Power Sources* **174**, 970-975, (2007).

96 Miller, A. C., McCluskey, F. P. & Taylor, J. A. An x-ray photoelectron spectroscopy study of aluminum surfaces treated with fluorocarbon plasmas. *J. Vac. Sci. Technol. A* **9**, 1461-1465, (1991).

97 Thomas, J. H. & Maa, J. S. X-ray photoelectron spectroscopy study of the surface chemistry of freon-oxygen plasma etched silicon. *Appl. Phys. Lett.* **43**, 859-861, (1983).

98 Bose, O., Kemnitz, E., Lippitz, A. & Unger, W. E. S. C 1s and Au 4f(7/2) referenced XPS binding energy data obtained with different aluminium oxides, -hydroxides and -fluorides. *Fresenius J. Anal. Chem.* **358**, 175-179, (1997).

99 Fluck, E., Weber, D., . X-ray photoelectron spectroscopy, Phosphorus compounds, Phosphonium salts, Oxoacids of phosphorus. *Z. Naturforsch. B* **29**, 603-607, (1974).

100 McGuire, G. E., Schweitz.Gk & Carlson, T. A. Study of Core Electron Binding-Energies in Some Group Iiia, Vb, and Vib Compounds. *Inorg. Chem.* **12**, 2450-2453, (1973).

101 Pereira, N., Matthias, C., Bell, K., Badway, F., Plitz, I., Al-Sharab, J., Cosandey, F., Shah, P., Isaacs, N. & Amatucci, G. G. Stoichiometric, Morphological, and Electrochemical Impact of the Phase Stability of Li_xCoO_2. *J. Electrochem. Soc.* **152**, A114-A125, (2005).
102 Lu, Y.-C., Gasteiger, H. A., Parent, M. C., Chiloyan, V. & Shao-Horn, Y. The Influence of Catalysts on Discharge and Charge Voltages of Rechargeable Li-Oxygen Batteries. *Electrochem. Solid State Lett.* **13**, A69-A72, (2010).
103 Ogasawara, T., Debart, A., Holzapfel, M., Novak, P. & Bruce, P. G. Rechargeable Li_2O_2 electrode for lithium batteries. *J. Am. Chem. Soc.* **128**, 1390-1393, (2006).
104 Gasteiger, H. A., Kocha, S. S., Sompalli, B. & Wagner, F. T. Activity benchmarks and requirements for Pt, Pt-alloy, and non-Pt oxygen reduction catalysts for PEMFCs. *Appl. Catal. B-Environ.* **56**, 9-35, (2005).
105 Paulus, U. A., Schmidt, T. J., Gasteiger, H. A. & Behm, R. J. Oxygen reduction on a high-surface area Pt/Vulcan carbon catalyst: a thin-film rotating ring-disk electrode study. *J. Electroanal. Chem.* **495**, 134-145, (2001).
106 Suntivich, J., Gasteiger, H. A., Yabuuchi, N. & Shao-Horn, Y. Electrocatalytic Measurement Methodology of Oxide Catalysts Using a Thin-Film Rotating Disk Electrode. *J. Electrochem. Soc.* **157**, B1263-B1268, (2010).
107 Aurbach, D., Daroux M.L., Faguy P. and Yeager E. The electrochemistry of noble metal electrodes in aprotic organic solvents containing lithium salts. *J. Electroanal. Chem.* **297**, 225-244, (1991).
108 Wang, D. Y., Xiao, J., Xu, W. & Zhang, J. G. High Capacity Pouch-Type Li-Air Batteries. *J. Electrochem. Soc.* **157**, A760-A764, (2010).
109 Xiao, J., Wang, D. H., Xu, W., Wang, D. Y., Williford, R. E., Liu, J. & Zhang, J. G. Optimization of Air Electrode for Li/Air Batteries. *J. Electrochem. Soc.* **157**, A487-A492, (2010).
110 Xu, W., Xiao, J., Wang, D. Y., Zhang, J. & Zhang, J. G. Effects of Nonaqueous Electrolytes on the Performance of Lithium/Air Batteries. *J. Electrochem. Soc.* **157**, A219-A224, (2010).
111 Zhang, J. G., Wang, D. Y., Xu, W., Xiao, J. & Williford, R. E. Ambient operation of Li/Air batteries. *J. Power Sources* **195**, 4332-4337, (2010).
112 Dobley, A., DiCarlo, J. & Abraham, K. M. in *41st Power Sources Conference*
113 Yang, X.-H., He, P., Xia, Y.-Y. Preparation of Mesocellular Carbon Foam and its Application for Lithium/Oxygen Batteries. *Electrochem. Comm.* **11**, 1127-1130, (2009).
114 Xie, B., Lee, H. S., Li, H., Yang, X. Q., McBreen, J. & Chen, L. Q. New electrolytes using Li_2O or Li_2O_2 oxides and tris(pentafluorophenyl) borane as boron based anion receptor for lithium batteries. *Electrochem. Comm.* **10**, 1195-1197, (2008).
115 Rich, R. in *Inorganic Reactions in Water* p.25-35 (2008).
116 Laoire, C. O., Mukerjee, S., Abraham, K. M., Plichta, E. J. & Hendrickson, M. A. Elucidating the Mechanism of Oxygen Reduction for Lithium-Air Battery Applications. *J. Phys. Chem. C* **113**, 20127-20134, (2009).
117 Andrews, L. Infrared Spectrum, Structure, Vibrational Potental Function, and Bonding in Lithium Superoxide Molecule LiO_2. *J. Chem. Phys.* **50**, 4288-4299, (1969).

118 Andrews, L. & Smardzew.Rr. Argon Matrix Raman-Spectrum of LiO_2 - Bonding in M^+O_2 Molecules and Ionic Model. *J. Chem. Phys.* **58**, 2258-2261, (1973).
119 Sawyer, D. T., Chiericato, G., Angelis, C. T., Nanni, E. J. & Tsuchiya, T. Effects of media and electrode materials on the electrochemical reduction of dioxygen. *Anal. Chem.* **54**, 1720-1724, (1982).
120 Sawyer, D. T. & Roberts Jr, J. L. Electrochemistry of oxygen and superoxide ion in dimethylsulfoxide at platinum, gold and mercury electrodes. *J. Electroanal. Chem.* **12**, 90-101, (1966).
121 Neyerlin, K. C., Gu, W., Jorne, J. & Gasteiger, H. A. Determination of Catalyst Unique Parameters for the Oxygen Reduction Reaction in a PEMFC. *J. Electrochem. Soc.* **153**, A1955-A1963, (2006).
122 Sorescu, D. C., Jordan, K. D. & Avouris, P. Theoretical study of oxygen adsorption on graphite and the (8,0) single-walled carbon nanotube. *J. Phys. Chem. B* **105**, 11227-11232, (2001).
123 Kinoshita, K. *Carbon: Electrochemical and Physicochemical Properties*. 1st edn, 35-46 (Wiley-Interscience, 1988).
124 Bard, A. J. & Faulkner, L. R. *Electrochemical Methods: Fundamentals and Applications*. 2nd edn, (John Wiley & Sons 2001).
125 Lu, Y.-C., Gasteiger, H. A., Crumlin, E., McGuire, J. R. & Shao-Horn, Y. Electrocatalytic Activity Studies of Select Metal Surfaces and Implications in Li-Air Batteries. *J. Electrochem. Soc.* **157**, A1016-A1025, (2010).
126 Lu, Y.-C., Kwabi, D. G., Yao, K. P. C., Harding, J. R., Zhou, J., Zuin, L. & Shao-Horn, Y. The discharge rate capability of rechargeable Li-O_2 batteries. *Energy Environ. Sci.* **4**, 2999-3007, (2011).
127 Lu, Y.-C., Xu, Z. C., Gasteiger, H. A., Chen, S., Hamad-Schifferli, K. & Shao-Horn, Y. Platinum-Gold Nanoparticles: A Highly Active Bifunctional Electrocatalyst for Rechargeable Lithium-Air Batteries. *J. Am. Chem. Soc.* **132**, 12170-12171, (2010).
128 Thapa, A. K. & Ishihara, T. Mesoporous [alpha]-MnO_2/Pd catalyst air electrode for rechargeable lithium-air battery. *J. Power Sources* **196**, 7016-7020, (2011).
129 McCloskey, B. D., Bethune, D. S., Shelby, R. M., Girishkumar, G. & Luntz, A. C. Solvents' Critical Role in Nonaqueous Lithium-Oxygen Battery Electrochemistry. *J. Phys. Chem. Lett.* **2**, 1161-1166, (2011).
130 Freunberger, S. A., Chen, Y. H., Peng, Z. Q., Griffin, J. M., Hardwick, L. J., Barde, F., Novak, P. & Bruce, P. G. Reactions in the Rechargeable Lithium-O_2 Battery with Alkyl Carbonate Electrolytes. *J. Am. Chem. Soc.* **133**, 8040-8047, (2011).
131 Peng, Z., Freunberger, S. A., Hardwick, L. J., Chen, Y., Giordani, V., Barde, F., Novak, P., Graham, D., Tarascon, J.-M. & Bruce, P. G. Oxygen reactions in a non-aqueous li^+ electrolyte. *Angew. Chem. Int. Ed.* **50**, 6351-6355, (2011).
132 Veith, G. M., Dudney, N. J., Howe, J. & Nanda, J. Spectroscopic Characterization of Solid Discharge Products in Li-Air Cells with Aprotic Carbonate Electrolytes. *J. Phys. Chem. C* **115**, 14325-14333, (2011).
133 Xiao, J., Hu, J. Z., Wang, D. Y., Hu, D. H., Xu, W., Graff, G. L., Nie, Z. M., Liu, J. & Zhang, J. G. Investigation of the rechargeability of Li-O_2 batteries in non-aqueous electrolyte. *J. Power Sources* **196**, 5674-5678, (2011).

134 Greeley, J., Stephens, I. E. L., Bondarenko, A. S., Johansson, T. P., Hansen, H. A., Jaramillo, T. F., Rossmeisl, J., Chorkendorff, I. & Norskov, J. K. Alloys of platinum and early transition metals as oxygen reduction electrocatalysts. *Nat. Chem.* **1**, 552-556, (2009).

135 Lima, F. H. B., Zhang, J., Shao, M. H., Sasaki, K., Vukmirovic, M. B., Ticianelli, E. A. & Adzic, R. R. Catalytic activity-d-band center correlation for the O_2 reduction reaction on platinum in alkaline solutions. *J. Phys. Chem. C* **111**, 404-410, (2007).

136 Nørskov, J. K., Rossmeisl, J., Logadottir, A., Lindqvist, L., Kitchin, J. R., Bligaard, T. & Jonsson, H. Origin of the overpotential for oxygen reduction at a fuel-cell cathode. *J. Phys. Chem. B* **108**, 17886-17892, (2004).

137 Stamenkovic, V. R., Mun, B. S., Arenz, M., Mayrhofer, K. J. J., Lucas, C. A., Wang, G. F., Ross, P. N. & Markovic, N. M. Trends in electrocatalysis on extended and nanoscale Pt-bimetallic alloy surfaces. *Nat. Mater.* **6**, 241-247, (2007).

138 Mitchell, R. R., Gallant, B. M., Thompson, C. V. & Shao-Horn, Y. All-carbon-nanofiber electrodes for high-energy rechargeable Li-O_2 batteries. *Energy Environ. Sci.* **4**, 2952-2958, (2011).

139 Aurbach, D., Gofer, Y. in *Nonaqueous electrochemistry* (ed D. Aurbach) Ch. 4, (CRC Press, 1999, p.200).

140 Gasteiger, H. A., Markovic, N. M. & Ross, P. N. H_2 and CO Electrooxidation on Well-Characterized Pt, Ru, and Pt-Ru. 2. Rotating Disk Electrode Studies of CO/H_2 Mixtures at 62 .degree.C. *J. Phys. Chem.* **99**, 16757-16767, (2002).

141 Green, C. L. & Kucernak, A. Determination of the Platinum and Ruthenium Surface Areas in Platinum-Ruthenium Alloy Electrocatalysts by Underpotential Deposition of Copper. I. Unsupported Catalysts. *J. Phys. Chem. B* **106**, 1036-1047, (2002).

142 Chierchie, T., Mayer, C. & Lorenz, W. J. Structural changes of surface oxide layers on palladium. *J. Electroanal. Chem.* **135**, 211-220, (1982).

143 Tremiliosi-Filho, G., Dall'Antonia, L.H., Jerkiewicz, G. Limit to extent of formation of the quasi-two-dimensional oxide state on Au electrodes *J. Electroanal. Chem.* **422**, 149-159, (1997).

144 Krol, A., Lin, C. S., Ming, Z. H., Sher, C. J., Kao, Y. H., Chen, C. T., Sette, F., Ma, Y., Smith, G. C., Zhu, Y. Z. & Shaw, D. T. X-ray-absorption studies of Y-Ba-Cu-O and Bi-Sr-Ca-Cu-O films at oxygen K edge by means of fluorescence and total electron yield: A comparison of two techniques. *Phys. Rev. B* **42**, 2635, (1990).

145 Henke, B. L., Gullikson, E. M. & Davis, J. C. X-Ray Interactions: Photoabsorption, Scattering, Transmission, and Reflection at E = 50-30,000 eV, Z = 1-92. *Atom. Data Nucl. Data Tables* **54**, 181-342, (1993).

146 Hammer, B. & Norskov, J. K. Theoretical surface science and catalysis - Calculations and concepts. *Adv. Catal.* **45**, 71-129, (2000).

147 Park, C. K., Park, S. B., Lee, S. Y., Lee, H., Jang, H. & Cho, W. I. Electrochemical Performances of Lithium-air Cell with Carbon Materials. *Bull. Korean Chem. Soc.* **31**, 3221-3224, (2010).

148 Lu, Y.-C., Gasteiger, H. A. & Shao-Horn, Y. Method Development to Evaluate the Oxygen Reduction Activity of High-Surface-Area Catalysts for Li-Air Batteries. *Electrochem. Solid State Lett.* **5**, A70-74, (2011).

149 Hassoun, J. H. J., Croce, F., Armand, M. & Scrosati, B. Investigation of the O_2 Electrochemistry in a Polymer Electrolyte Solid-State Cell. *Angew. Chem.-Int. Edit.* **50**, 2999-3002, (2011).
150 Norskov, J. K., Bligaard, T., Rossmeisl, J. & Christensen, C. H. Towards the computational design of solid catalysts. *Nat Chem* **1**, 37-46, (2009).
151 Andrei, P., Zheng, J. P., Hendrickson, M. & Plichta, E. J. Some Possible Approaches for Improving the Energy Density of Li-Air Batteries. *J. Electrochem. Soc.* **157**, A1287-A1295, (2010).
152 Chen, H., Armand, M., Demailly, G., Dolhem, F., Poizot, P. & Tarascon, J. M. From biomass to a renewable $Li_xC_6O_6$ organic electrode for sustainable Li-ion batteries. *Chemsuschem* **1**, 348-355, (2008).
153 Zhou, J. G., Fang, H. T., Maley, J. M., Murphy, M. W., Peter Ko, J. Y., Cutler, J. N., Sammynaiken, R., Sham, T. K., Liu, M. & Li, F. Electronic structure of TiO_2 nanotube arrays from X-ray absorption near edge structure studies. *J. Mater. Chem.* **19**, 6804-6809, (2009).
154 Xu, Y. & Shelton, W. A. O_2 reduction by lithium on Au(111) and Pt(111). *J. Chem. Phys.* **133**, 024703, (2010).
155 Zhang, S. S. & Jow, T. R. Aluminum corrosion in electrolyte of Li-ion battery. *J. Power Sources* **109**, 458-464, (2002).
156 Xu, Z., Carlton, C. E., Allard, L. F., Shao-Horn, Y. & Hamad-Schifferli, K. Direct Colloidal Route for Pt-Covered AuPt Bimetallic Nanoparticles. **1**, 2514-2518, (2010).
157 Mott, D., Luo, J., Smith, A., Njoki, P. N., Wang, L., Zhong, C. J. Nanocrystal and surface alloy properties of bimetallic Gold-Platinum nanoparticles *Nanoscale Res. Lett.* **2**, 12-16, (2007).
158 Darling, A. S., Mintern, R.A., Chaston, J.C. The Gold Platinum System-Discussion. *J. Inst. Met.* **81**, 125, (1953).
159 Nart, F. C. & Vielstich, W. in *Handbook of Fuel Cells – Fundamentals, Technology and Applications* (John Wiley & Sons 2009).